Search for the Stueckelberg Z′ Decaying into Dimuon Pairs at CMS/LHC

by Jinzhong Zhang

B.S. in Physics, Peking University
M.S. in Physics, Northeastern University

A dissertation submitted to

The Faculty of
the College of Science of
Northeastern University
in partial fulfillment of the requirements
for the degree of Doctor of Philosophy

July 30, 2014

Dissertation directed by

George Alverson
Associate Professor of Physics

Acknowledgments

First I would like to thank our Northeastern CMS group: the professors, George Alverson, Darien Wood, Emanuela Barberis, and Toyoko Orimoto, who gave suggestions every week in the group meetings. Especially my advisor, George Alverson, talks with me a lot also outside meetings. My colleagues, Daniele Trocino, Darin Baumgartel, Matthew Chasco, and David Nash, always discussed with me in the office and shared their instrumental codes, which saved lots of my time.

Second I would like to thank the dimuon Z prime analysis group, who provided most data analysis materials in this thesis. In particular, I thank Gena Kukartsev who provided the limit setting code and Alexander Belyaev who answered lots of questions on the (C_u, C_d).

I am also grateful to Prof. Pran Nath for clearing up lots of my questions in quantum field theory.

In addition, I thank the CSC detector operating group, especially Tim Cox, Gregory Rakness, Mikhail Ignatenko, Evaldas Juska, Chaouki Boulahouache, and Armando Lanaro. They helped me a lot with understanding the detectors and with the efficiency measurement work. The b-tagging working group, especially Alexander Schmidt, Andrea Rizzi, Daniel Bloch, Wolfgang Adam, and Meenakshi Narain, also helped a lot with physics object building and verifying. I am grateful to them as well. Though those works do not have a close relationship with this thesis topic and have not been introduced in this thesis, they are quite necessary for my future research.

When I started with the works in CERN, several people helped me a lot with getting familiar with the tools and concepts in high energy experiments, in particular Si Xie who was a graduate student in MIT group and Oana Boeriu who was a post doctor in Northeastern University group. Thank them for sure.

Finally, I thank my parents. They supported me a lot both mentally and during the whole graduate study. Especially my mother, she suffered lots of pains from her cancer and medical treatment in my thesis writing year and has fortunately conquered the cancer.

Best wishes to all of the people mentioned above.

Thank the United States National Science Foundation for financial support as well.

Jinzhong Zhang, August 8, 2014

Abstract of Dissertation

This thesis describes a search for a new particle with narrow decay width decaying into dimuon pairs. In 2012 and 2011, the Large Hadron Collider produced proton-proton collisions. The CMS detector at the CERN laboratory recorded about $5\,\mathrm{fb}^{-1}$ integrated luminosity at a center-of-mass energy of $\sqrt{s} = 7\,\mathrm{TeV}$ and about $20\,\mathrm{fb}^{-1}$ at $\sqrt{s} = 8\,\mathrm{TeV}$. The upper limits on the ratio of the cross section times dimuon branching fraction of the Stueckelberg Z' boson to that of the standard model Z boson are determined at the 95% confidence level by the Bayesian technique. The parallel analysis in the dielectron channel is combined with this dimuon analysis. The combined result excludes, at 95% confidence level, the Stueckelberg Z' boson with $\epsilon = 0.06(0.04)$ lighter than $890(540)\,\mathrm{GeV}$ based on the CMS data recorded in 2011. The Stueckelberg Z' boson excluded parameter space, at 95% confidence level, is given in a (mass, ϵ) and (C_d,C_u) combined plot.

Table of Contents

List of Figures

List of Tables

Notation

Units

In this thesis, we use natural units, where $\hbar = c = 1$. In this system,
[length] = [time] = [energy]$^{-1}$ = [mass]$^{-1}$

- 1 eV^{-1} of length=1 eV$^{-1}\hbar c = 1.97 \times 10^{-7}$ meter
- 1 eV^{-1} of time=1 eV$^{-1}\hbar = 6.58 \times 10^{-16}$ second
- 1 eV of mass = 1eV$^{-1}/(c^2) = 1.78 \times 10^{-36}$ kilogram
- 1 eV of energy = 1.60×10^{-19} kg·m^2/s^2

The electron charge is still e.

Einstein Summation Convention

When an index variable appears twice in a single term it implies summation of that term over all the values of the index:

$$\sum_i x_i y^i \equiv x_i y^i$$

Four-vector Notation

- Position: $x^\mu = (x^0, \vec{x})$, x^0 is the time
- Momentum: $p^\mu = (E, \vec{p})$
- Electromagnetic field: $A^\nu = (\Phi, \vec{A})$. The Coulomb potential of a point charge is Φ. The magnetic vector potential is $\vec{A}$. The magnetic field $\vec{B} = \vec{\nabla} \times \vec{A}$.

- Lorentz scalar and metric tensor:

$$xx \equiv x^\mu x_\mu = g_{\mu\nu} x^\mu x^\nu = (x^0)^2 - (x^1)^2 - (x^2)^2 - (x^3)^2, \quad \text{also} \quad px \equiv p^\mu x_\mu = g_{\mu\nu} p^\mu x^\nu,$$

where

$$g_{\mu\nu} = g^{\mu\nu} = \begin{bmatrix} 1 & 0 & 0 & 0 \\ 0 & -1 & 0 & 0 \\ 0 & 0 & -1 & 0 \\ 0 & 0 & 0 & -1 \end{bmatrix}$$

- Maxwell equations:

$$\begin{cases} \text{Faraday's law of induction and Gauss's law for magnetism:} & \epsilon^{\mu\nu\rho\sigma} \partial_\nu F_{\rho\sigma} = 0 \\ \text{Gauss's Law and Ampre's law:} & \partial_\mu F^{\mu\nu} = q j^\nu \end{cases},$$

where $F_{\mu\nu} = \partial_\mu A_\nu - \partial_\nu A_\mu$. The Levi-Civita symbol, $\epsilon^{\mu\nu\rho\sigma}$, is defined as $\epsilon^{0123} = +1$. The 4-vector current density is j^ν, where $j^\nu = (\rho, \vec{j})$, and where ρ is the charge density and $\vec{j}$ is the conventional current density.

- The Lagrangian for classical electrodynamics (Gauss's Law and Ampre's law):

$$\mathcal{L} = \mathcal{L}_{\text{field}} + \mathcal{L}_{\text{int}} = -\frac{1}{4} F^{\mu\nu} F_{\mu\nu} - q A_\nu J^\nu \tag{1}$$

The Pauli Matrices

σ^i are the Pauli sigma matrices.

$$\sigma^0 = I = \begin{bmatrix} 1 & 0 \\ 0 & 1 \end{bmatrix}; \quad \sigma^1 = \begin{bmatrix} 0 & 1 \\ 1 & 0 \end{bmatrix}; \quad \sigma^2 = \begin{bmatrix} 0 & -i \\ i & 0 \end{bmatrix}; \quad \sigma^3 = \begin{bmatrix} 1 & 0 \\ 0 & -1 \end{bmatrix}$$

$\vec{\sigma} = (\sigma^1, \sigma^2, \sigma^3)$; $\sigma^\mu = (I, \vec{\sigma})$; $\bar{\sigma^\mu} = (I, -\vec{\sigma})$.

The Dirac Matrices

$$\gamma^0 = \begin{bmatrix} 0 & I \\ I & 0 \end{bmatrix} = \begin{bmatrix} 0 & 0 & 1 & 0 \\ 0 & 0 & 0 & 1 \\ 1 & 0 & 0 & 0 \\ 0 & 1 & 0 & 0 \end{bmatrix} \qquad \gamma^1 = \begin{bmatrix} 0 & \sigma^1 \\ -\sigma^1 & 0 \end{bmatrix} = \begin{bmatrix} 0 & 0 & 0 & 1 \\ 0 & 0 & 1 & 0 \\ 0 & -1 & 0 & 0 \\ -1 & 0 & 0 & 0 \end{bmatrix}$$

$$\gamma^2 = \begin{bmatrix} 0 & \sigma^2 \\ -\sigma^2 & 0 \end{bmatrix} = \begin{bmatrix} 0 & 0 & 0 & -i \\ 0 & 0 & i & 0 \\ 0 & i & 0 & 0 \\ -i & 0 & 0 & 0 \end{bmatrix} \qquad \gamma^3 = \begin{bmatrix} 0 & \sigma^3 \\ -\sigma^3 & 0 \end{bmatrix} = \begin{bmatrix} 0 & 0 & 1 & 0 \\ 0 & 0 & 0 & -1 \\ -1 & 0 & 0 & 0 \\ 0 & 1 & 0 & 0 \end{bmatrix}$$

$$\gamma^5 \equiv i\gamma^0\gamma^1\gamma^2\gamma^3 = \begin{bmatrix} -1 & 0 & 0 & 0 \\ 0 & -1 & 0 & 0 \\ 0 & 0 & 1 & 0 \\ 0 & 0 & 0 & 1 \end{bmatrix}$$

Chapter 1

Introduction

So far as we know, the best and simplest model describing the microscopic world is the Standard Model (SM). Motivated by the discovery of a series of particles that were later named baryons and leptons, this model originated in the 1960s and was finalized in the mid-1970s [3]. With the discovery of the neutral current in 1973 [4, 5, 6], the discovery of the strong force carrier, the gluon, in 1979 [7], and the confirmation of the weak force carriers, the $W^{\pm}$ and the Z bosons [8, 9], the enigma of the existence of the last SM predicted particle, the Higgs, puzzled scientists for decades.

To give a final answer to the remaining puzzles of the SM and to explore beyond, the Large Hadron Collider (LHC) was built in Switzerland from 1998 to 2008. The LHC delivered the first proton-proton collisions in Nov 2009. In 2010, the beam energy was ramped up to 3.5 TeV and the center-of-mass energy was 7 TeV. In the next year, 2011, the LHC continued running at this beam energy in order to accumulate enough data for analysis. In 2012, the final year of LHC run 1 operation, 4 TeV beams were produced with a higher instantaneous luminosity of approximately 10^{33} to 10^{34} $\mathrm{cm}^{-2}\mathrm{s}^{-1}$. In the following year, on March 14th, 2013, by combining all of the data recorded by the Compact Muon Solenoid (CMS) detector located in France and the A Toroidal LHC ApparatuS (ATLAS) detector located in Switzerland in 2011 and 2012, the existence of a particle compatible with the Higgs boson hypothesis was confirmed [10, 11].

However, physics never ends. There are problems outside the SM, such as neutrino oscillations, dark matter, general relativity, and so on. Many models are trying to understand those beyond SM phenomena. This thesis describes the search for one of those models, the Stueckelberg minimal supersymmetric extension of the SM. The search has been performed using 7 TeV and 8 TeV proton-proton collision data recorded by the CMS experiment. For 7 TeV, the dimuon event sample used corresponds to an integrated luminosity of $5.28 \pm 0.12\,\mathrm{fb}^{-1}$ while the dielectron event sam-

ple used corresponds to an integrated luminosity of $4.98 \pm 0.11\,\mathrm{fb}^{-1}$. For 8 TeV, the dimuon event sample used corresponds to[1] an integrated luminosity of $20.6 \pm 0.5\,\mathrm{fb}^{-1}$ while the dielectron event sample used corresponds to an integrated luminosity of $19.6 \pm 0.5\,\mathrm{fb}^{-1}$. The work is done by the exotic dilepton group. I participated in that and focused on the Stueckelberg extension.

In the chapter 2, I give a brief description of the Standard Model, as well as the Stueckelberg mechanism. A narrow resonance is expected in that model. In chapter 3, LHC and CMS are described. In chapter 4, there is a discussion of searches using the $\mathrm{Z}' \to l^+l^-$ process. Since no significant signal is observed, the limits on the ratio R_σ of the production cross section times branching fraction for high-mass resonances to that of the Z are presented as the result. Many experimental and theoretical uncertainties are common in Z' and SM Z measurement that can then be canceled. Based on the limits of the ratio R_σ, the limits of the couplings between the Stueckelberg and u, d quarks, as well as the limits on the (mass, ϵ) region in the parameter space of the Stueckelberg extension, are presented in plots. Since the analysis using data recorded by CMS in 2012 has not been published, this chapter only shows the work done using data recorded in 2011. The analysis and results using data recorded in 2012 are shown in Appendix A and B.

[1] The uncertainties are calculated according to [12].

Chapter 2

Theory

According to the theory of relativity, our universe is a four dimensional spacetime (Minkowski space). Time and space are only different in the metric and naturally do not have to have different units. According to quantum field theory, spacetime, the universe, is filled with states of fields. "Wave" and "particle" are human-coined words to describe phenomena in approximations, which reflect only one aspect of the object. The objects of fundamental physics study are fields. The transitions among the states of those fields make our universe alive. The states are represented by rays in Hilbert space (see Weinberg I chapter 2.1 [13]). This chapter starts from three principles, the least action principle, the principle that laws of physics are invariant in all inertial systems, and the principle of global and local gauge invariance. Moreover, the theory must be renormalizable. Then based on some experimental facts, I briefly describe the standard model (SM) and one of the beyond SM theories in which can be explored using data from the Large Hadron Collider and its detectors. I omit an introduction to renormalization as being beyond of the scope of this thesis.

2.1 Lagrangian Field Theory

In the local field theory, the action S is defined as the time integral of the Lagrangian (L) and can be written as the spatial and time integral of the Lagrangian density ($\mathcal{L}$). $\mathcal{L}$ is a function of one or more fields $\psi_i(x)$ and their derivatives $\partial_\mu \psi_i$, where i is the index of the fields:

$$S \equiv \int L dt = \int \mathcal{L}(\psi_i, \partial_\mu \psi_i) d^4x.$$

The unit of S is energy multiplied by time. I use the natural unit, where time and space have the same units. The unit of S is 1 or unit-less. The unit of $\mathcal{L}$ is

[length]$^{-4}$. Because S is a Lorentz scalar, $\mathcal{L}$ must also be Lorentz invariant and gauge invariant. The action S must be Hermitian because it reflects a observable path in the parameter space.

The principle of least action states that when a system evolves from one given configuration to another between times t_1 and t_2, it does so along the "path" in configuration space for which S is an extremum (normally a minimum) [14]. In other words, if $\mathcal{L}$ reflects the real world faithfully, the real world can be considered as an incorporation of fields and the parameters of those fields versus the time will follow the path in which $\delta S = 0$. The path in the parameter space of a field can be solved using the Euler-Lagrange equations of motion, which are derived from the principle of least action assuming that the deformations of the field ($\delta\psi_j$, where j is the index of that field) vanish on the spatial boundary. The Euler-Lagrange equations of motion are written as

$$\partial_\mu \left(\frac{\partial \mathcal{L}(\psi_i, \partial_\mu \psi_i)}{\partial(\partial_\mu \psi_j)} \right) - \frac{\partial \mathcal{L}(\psi_i, \partial_\mu \psi_i)}{\partial \psi_j} = 0,$$

where j runs from one to the number of fields considered in $\mathcal{L}$.

In the following sections, we will introduce a brief procedure to build the SM $\mathcal{L}$ from hypotheses, known theories and facts.

2.2 Gauge Invariance

Noether's theorem states that any continuous symmetry of the action of a physical system has a corresponding conservation law [15]. In quantum field theory, the physical system is represented by $\mathcal{L}(\psi_i, \partial_\mu \psi_i)$. The internal symmetry transformations that commute with the spacetime components of the field lead to conservation laws as well[1]. For example, the symmetry in the U(1) global phase transformation $\psi(x) \to e^{i\alpha}\psi(x)$ where α is a real constant leads to charge conservation.

In the case that α is not a constant, $\alpha(x)$ varies arbitrarily from point to point. Noether's theorem should still be valid and we should still be able to write down a $\mathcal{L}(\psi_i, \partial_\mu \psi_i)$ that leads to conservation laws. However, $\partial_\mu \psi(x)$ (we can drop the index i to indicate the general case here) does not keep its form under the transformation $\psi(x) \to e^{i\alpha(x)}\psi(x)$. For example, in an n-dimensional Hilbert space, the definition of

[1]We can write ψ_i as $\psi(x, \text{phase}(x))$ to interpret its internal symmetries.

$\partial_\mu(x)$ transforms like

$$\begin{aligned} \partial_\mu\psi(x) &\equiv \lim_{\epsilon\to 0}\frac{\psi(x^\mu+\epsilon)-\psi(x^\mu)}{\epsilon} \\ \to\ \partial_\mu[e^{i\alpha(x)}\psi(x)] &= \lim_{\epsilon\to 0}\frac{e^{i\alpha(x^\mu+\epsilon)}\psi(x^\mu+\epsilon)-e^{i\alpha(x^\mu)}\psi(x^\mu)}{\epsilon} \\ &= e^{i\alpha(x)}[i\alpha(x)\partial_\mu\alpha(x)+\partial_\mu]\psi(x), \end{aligned}$$

where we only leave the variable of interest, x^μ, in the parentheses, as in the following context.

In order to let the $\mathcal{L}$ keep its form, we have to write down some terms to compensate the in-covariance caused by ∂_μ. We introduce a $2n$ dimension scalar quantity $U(y,x)$ that depends on two Hilbert space points. For the same Hilbert space point, $U(x;x)=1$. For different Hilbert space points, $|U(y;x)|\equiv 1$ (phase only). Instead of ∂_μ, we define the covariant derivative D_μ that depends on $U(x^\mu+\epsilon;x^\mu)$. D_μ is independent of the arbitrary phase $\alpha(x)$. It transforms as follows:

$$\begin{aligned} D_\mu\psi(x) &\equiv \lim_{\epsilon\to 0}\frac{\psi(x^\mu+\epsilon)-U(x^\mu+\epsilon;x^\mu)\psi(x^\mu)}{\epsilon} \\ \to\ D_\mu[e^{i\alpha(x)}\psi(x)] &= \lim_{\epsilon\to 0}\frac{e^{i\alpha(x^\mu+\epsilon)}\psi(x^\mu+\epsilon)-U'(x^\mu+\epsilon;x^\mu)e^{i\alpha(x^\mu)}\psi(x^\mu)}{\epsilon} \\ &= e^{i\alpha(x)}D_\mu\psi(x). \end{aligned} \tag{2.1}$$

In order to satisfy equation 2.1,

$$U(x^\mu+\epsilon;x^\mu)\to U'(x^\mu+\epsilon;x^\mu)=e^{i\alpha(x^\mu+\epsilon)}U(x^\mu+\epsilon;x^\mu)e^{-i\alpha(x^\mu)}. \tag{2.2}$$

Because $U(y;x)$ is a unitary scalar quantity, $U(x^\mu+\epsilon;x^\mu)$ can be rewritten as $\exp[-iq\beta_\mu(x^\mu+\epsilon;x^\mu)]$, where $\beta_\mu(x^\mu+\epsilon;x^\mu)$ is a function satisfying $\beta_\mu(x^\mu;x^\mu)=0$ and a unit-less constant q is arbitrarily extracted. Expanding $U(x^\mu+\epsilon;x^\mu)$ at the point of $U(x^\mu;x^\mu)$, we have

$$\begin{aligned} U(x^\mu+\epsilon;x^\mu) &= \exp[-iq\beta_\mu(x^\mu+\epsilon;x^\mu)] \\ &= \exp[-iq(\epsilon\left.\frac{\partial\beta_\mu}{\partial(x^\mu)}\right|_{x^\mu}+\mathcal{O}(\epsilon^2))] \\ &= 1-iq\epsilon A_\mu(x)+\mathcal{O}(\epsilon^2), \end{aligned} \tag{2.3}$$

Inserting Equation 2.3 into Equation 2.1, we have

$$D_\mu\psi(x) = \lim_{\epsilon\to 0}\frac{\psi(x^\mu+\epsilon)-\psi(x^\mu)}{\epsilon}+\lim_{\epsilon\to 0}\frac{[1-U(x^\mu+\epsilon;x^\mu)]\psi(x^\mu)}{\epsilon} \tag{2.4}$$

$$= [\partial_\mu+iqA_\mu(x)]\psi(x). \tag{2.5}$$

Here we know that the unit of $A_\mu(x)$ is [length]$^{-1}$ or [energy].

Inserting equation 2.3 into equation 2.2 and ignoring the terms whose order is higher than one, we have

$$\begin{aligned} U'(x^\mu+\epsilon;x^\mu) &= e^{i\alpha(x^\mu+\epsilon)}[1-iq\epsilon A_\mu(x)]e^{-i\alpha(x)} \\ &= e^{i\partial_\mu\alpha(x)\epsilon}[1-iq\epsilon A_\mu(x)] \\ &= [1+i\partial_\mu\alpha(x)\epsilon][1-iq\epsilon A_\mu(x)] \\ &= 1-iq\epsilon[A_\mu(x)-\frac{1}{q}\partial_\mu\alpha(x)], \end{aligned}$$

in which we can see that $A_\mu(x)$ transforms like

$$A_\mu(x) \to A_\mu(x)-\frac{1}{q}\partial_\mu\alpha(x).$$

Once we introduce the vector field $A_\mu(x)$, the locally invariant $\mathcal{L}$ must have a kinetic energy term corresponding to $A_\mu(x)$. This term can depend on $A_\mu(x)$ and its derivatives but not on ψ. In addition, it must be Lorentz invariant and gauge invariant because of the principle that laws of physics are invariant in all inertial systems and phase space. The kinetic term can thus be constructed from the commutator of covariant derivatives:

$$[D_\mu,D_\nu]\psi(x) \to e^{i\alpha(x)}[D_\mu,D_\nu]\psi(x)$$

Since $e^{i\alpha(x)}$ is the factor for the entire term, $[D_\mu,D_\nu]$ must be invariant under local gauge transformation.

$$\begin{aligned} [D_\mu,D_\nu]\psi &= [\partial_\mu,\partial_\nu]\psi+iq([\partial_\mu,A_\nu]-[\partial_\nu,A_\mu])\psi-q^2[A_\mu,A_\nu]\psi \\ &= iq(\partial_\mu A_\nu-\partial_\nu A_\mu)\psi \\ &= iqF_{\mu\nu}\psi, \end{aligned}$$

where $F_{\mu\nu}\equiv\partial_\mu A_\nu-\partial_\nu A_\mu$. The unit of $F_{\mu\nu}$ is [length]$^{-2}$.

Because $\mathcal{L}$ is a scalar and the unit of $\mathcal{L}$ is [length]$^{-4}$, $F_{\mu\nu}F^{\mu\nu}$, $i\epsilon^{\alpha\beta\mu\nu}F_{\alpha\beta}F_{\mu\nu}$ and $\partial^\nu\partial^\mu F_{\mu\nu}$ are possible terms for the kinetic energy of $A_\mu(x)$ in $\mathcal{L}$. The $\partial^\nu\partial^\mu F_{\mu\nu}$ can be eliminated by some transformations, so this term is trivial. As $i\epsilon^{\alpha\beta\mu\nu}F_{\alpha\beta}F_{\mu\nu}$ violates the parity (P) and time reversal (T) transformations, it may be excluded if we require P and T symmetries.

This is the general case of a gauge transformation. The $A_\mu(x)$ can be different formats, such as a summation of products of tensors. That leads to the quantum electrodynamics(QED) and the quantum chromodynamics(QCD).

2.3 Lorentz Invariance

All terms of the $\mathcal{L}$ have to be Lorentz invariant to preserve the Lorentz invariance of $\mathcal{L}$. The homogeneous change of x^μ is represented by $x^\mu \to \Lambda^\mu{}_\nu x^\nu$, where the transformation matrix Λ includes the ordinary spacetime rotations. The spacetime rotation includes both boosting and spatial rotations (combinations of any two dimensions of the four dimensional spacetime). Because $x^2 \equiv x^\mu x_\mu = g_{\mu\nu}x^\mu x^\nu$,

$$g_{\mu\nu}\Lambda^\mu{}_\rho\Lambda^\nu{}_\sigma = g_{\rho\sigma}. \tag{2.6}$$

That is the basic hint to find Lorentz scalars.

A scalar field transforms as $\phi(x) \to \phi(\Lambda^{-1}x)$. The whole $\mathcal{L}$ transforms as a scalar, $\mathcal{L}(x) \to \mathcal{L}(\Lambda^{-1}x)$. The derivatives of a scalar field ϕ transform as

$$\frac{\partial\phi(x)}{\partial x^\mu} \to \Lambda^\mu{}_\rho \frac{\partial\phi(\Lambda^{-1}x)}{\partial(\Lambda^{-1}x)^\rho}.$$

By use of equation 2.6 and considering gauge invariance, we can derive that the terms $D^\mu\phi(x)^\dagger D_\mu\phi(x)$ and $\phi(x)^\dagger\phi(x)$ are both Lorentz and gauge invariant, and also Hermitian. The term $[\phi(x)^\dagger\phi(x)]^2$ is also possible. However, terms whose orders are higher than 4 are not renormalizable so they are not possible.

A vector field $A^\mu(x)$ transforms as $A^\mu(x) \to \Lambda^\mu{}_\rho A^\rho(\Lambda^{-1}x)$. It naturally transforms like the derivatives. The gauge derivative D_μ is just a summation of the derivative and a vector field.

A spinor field carries a generic Lorentz index, e.g. $\psi_A(x)$. Unlike the vector field, the index of a spinor field does not associate with spacetime, but the spinor field itself still follows the Lorentz spacetime transformation. Like the spacetime metric tensor $g_{\mu\nu}$, the spinor metric tensor is

$$\epsilon^{AB} = \begin{bmatrix} 0 & I \\ -I & 0 \end{bmatrix} = -\epsilon_{AB} = \begin{bmatrix} 0 & -I \\ I & 0 \end{bmatrix}.$$

So a Lorentz scalar built from spinor fields is

$$\psi^A\chi_A = \epsilon^{AB}\psi_B\chi_A = -\epsilon^{BA}\psi_B\chi_A = -\psi_B\chi^B.$$

A left-handed spinor field transforms as $\psi_{L_A}(x) \to L_A{}^B(\Lambda)\psi_{L_B}(\Lambda^{-1}x)$, where $L_A{}^B$ is a finite-dimensional matrix that depends on Λ. $L_A{}^B(\Lambda)$ obeys the group composition rule $L_A{}^B(\Lambda')L_B{}^C(\Lambda) = L_A{}^C(\Lambda'\Lambda)$ so that $L_A{}^B(\Lambda)$ forms a representation of the Lorentz group. The Hermitian conjugation of a left-handed spinor field becomes a right-handed spinor field: $(\psi_{L_A}(x))^\dagger = \psi^\dagger_{R_A}(x)$. A right-handed vector

field transforms as $\psi_{R_A}^\dagger(x) \to R_A{}^B(\Lambda)\psi_{R_B}^\dagger(\Lambda^{-1}x)$. It can be proved that the left-handed and right handed terms transform as [16]

$$\begin{aligned} \psi_{R_A}^\dagger \bar{\sigma}^{\mu AC} \chi_{LC} &\to \Lambda^\mu{}_\nu \psi_{R_A}^\dagger \bar{\sigma}^{\mu AC} \chi_{LC} \\ \text{or} \quad \psi_R{}^{\dagger A} \sigma^\mu_{AC} \chi_L{}^C &\to \Lambda^\mu{}_\nu \psi_R{}^{\dagger A} \sigma^\mu_{AC} \chi_L{}^C. \end{aligned} \tag{2.7}$$

So the terms

$$i\psi_{R_A}^\dagger \bar{\sigma}^{\mu AC} D_\mu \psi_{LC} \quad \text{and} \quad i\psi_R{}^{\dagger A} \sigma^\mu_{AC} D_\mu \psi_L{}^C \tag{2.8}$$

are Lorentz invariant. By setting the boundary condition $\lim_{x\to\infty} \psi_{R_A}^\dagger \bar{\sigma}^{\mu AC} \psi_{LC} \to 0$, the action S is still Hermitian with terms in Equation 2.8.

Because $\psi^A \chi_A = -\psi_A \chi^A$ (anti-commutation), it is not possible to write down terms without derivatives by a single spinor left or right handed field: $\psi_{R_A}^\dagger \psi_L{}^A$ is not Hermitian; $\psi_L{}^A \psi_{LA} + \psi_{RA}{}^\dagger \psi_R{}^{\dagger A}$ is Hermitian but not even globally gauge invariant[2]. With an additional spinor field, we can make a both Hermitian and gauge invariant term without derivatives. Since two spinor field phase spaces transforms as

$$\begin{bmatrix} \psi_L \\ \zeta_L \end{bmatrix} \to \begin{bmatrix} \cos\alpha & \sin\alpha \\ -\sin\alpha & \cos\alpha \end{bmatrix} \begin{bmatrix} \psi_L \\ \zeta_L \end{bmatrix}$$

We can always define

$$\begin{aligned} \chi_L &\equiv \frac{1}{\sqrt{2}}(\psi_L + i\zeta_L) \\ \xi_L &\equiv \frac{1}{\sqrt{2}}(\psi_L - i\zeta_L). \end{aligned}$$

So,

$$\begin{bmatrix} \chi_L \\ \xi_L \end{bmatrix} \to \begin{bmatrix} \frac{1}{\sqrt{2}}(e^{-i\alpha}\psi_L + ie^{-i\alpha}\zeta_L) \\ \frac{1}{\sqrt{2}}(e^{+i\alpha}\psi_L - ie^{+i\alpha}\zeta_L) \end{bmatrix} = \begin{bmatrix} e^{-i\alpha}\chi_L \\ e^{+i\alpha}\xi_L \end{bmatrix}.$$

With terms in Equation 2.8, we can write down a $\mathcal{L}$ term with derivative:

$$i\chi_{RA}^\dagger \bar{\sigma}^{\mu AC} D_\mu \chi_{LC} + i\xi_R{}^{\dagger A} \sigma^\mu_{AC} D_\mu \xi_L{}^C$$

and a term without derivative:

$$\xi_L{}^A \chi_{LA} + \chi_{RA}^\dagger \xi_R{}^{\dagger A}.$$

[2]The $\mathcal{L}$ without such terms leads to the Weyl equations, which can describe massless spin $\frac{1}{2}$ fields, e.g. the neutrinos in the Standard Model.

Both of them are Hermitian, Lorentz and gauge invariant. By setting the boundary condition $\lim_{x\to\infty} \xi_R^{\dagger\,A}\sigma^\mu_{AC}\xi_L{}^C \to 0$, $i\xi_R{}^{\dagger A}\sigma^\mu_{AC}D_\mu\xi_L{}^C$ is equivalent to $i\xi_L{}^A\sigma^\mu_{AC}D_\mu\xi_R^{\dagger\,C}$ in the action S. With definitions,

$$\Psi \equiv \begin{bmatrix} \chi_{LC} \\ \xi_R^{\dagger\,C} \end{bmatrix} \quad \text{and} \quad \bar{\Psi} \equiv \Psi^\dagger\gamma^0 = [\chi^\dagger_{RC}, \xi_L{}^C] \begin{bmatrix} 0 & \delta^C{}_A \\ \delta_C{}^A & 0 \end{bmatrix} = [\xi_L{}^A, \chi^\dagger_{RA}],$$

and using the Dirac matrices, the term with derivative becomes $i\bar{\Psi}\gamma^\mu D_\mu\Psi$; the term without derivative becomes $\bar{\Psi}\Psi$. They are both the possible terms for spinor fields in the $\mathcal{L}$.

Chapter 5.4 and 5.5 of Weinberg I [13] give a complete and direct derivation from Lorentz invariance to the Dirac equation. This section is an alternative approach.

2.4 The Quantum Electrodynamics (QED)

The last two sections provided the spinor field $\mathcal{L}$ with terms including a gauge vector field and its kinetic term. Expanding the term $i\bar{\Psi}\gamma^\mu D_\mu\Psi$ according to equation 2.5, we get a term that represents the interaction of the spinor fields and the gauge vector field[3], which is $-q\bar{\Psi}\gamma^\mu A^\gamma_\mu\Psi$.

The vector field $A^\gamma_\mu(x)$ can be used to represent the magnetic vector potential in electrodynamics. Comparing the electrodynamics Lagrangian (Equation 1), because the spinor field Ψ commutes with the vector field $A^\gamma_\mu(x)$, we know that the currency density $J^\mu = \bar{\Psi}\gamma^\mu\Psi$. So the dimension of $\bar{\Psi}\Psi$ is $[\text{length}]^{-3}$ and the factor of the $F_{\mu\nu}F^{\mu\nu}$ is $-\frac{1}{4}$. Thus the mass term of the spinor field in $\mathcal{L}$ is $m\bar{\Psi}\Psi$, where the unit of m is $[\text{length}]^{-1}$ or [energy].

It can be proved that the higher order terms, e.g. $\frac{1}{m_1}D^\mu\bar{\Psi}D_\mu\Psi$, $\frac{1}{m_2^2}(\bar{\Psi}\Psi)^2$, are not renormalizable [14], where m_i has the unit of [energy]. We then have the QED Lagrangian which describes a spin $\frac{1}{2}$ field interacting with the electromagnetic vector field:

$$\mathcal{L}_{\text{QED}} = i\bar{\Psi}\gamma^\mu D_\mu\Psi - m\bar{\Psi}\Psi - \frac{1}{4}F_{\mu\nu}F^{\mu\nu}, \tag{2.9}$$

where $D_\mu = \partial_\mu - iqA^\gamma_\mu$; $F_{\mu\nu} \equiv \partial_\mu A^\gamma_\nu - \partial_\nu A^\gamma_\mu$.

2.5 The Quantum Chromodynamics (QCD)

Based on the discovery of a bunch of hadrons, scientists built the quark model and further incorporated them into an SU(3) gauge degree of freedom, where the number

[3] In fact, it is a kind of the Yukawa coupling.

3 indicates three kinds of color charges named *blue*, *green* and *red*. In mathematical expression, the gauge is represented by a summation of productions of fields and SU(3) generators:

$$D_\mu = \partial_\mu - ig_s G^a_\mu t^a,$$

where the G^a_μ is the vector field for the SU(3) generator t^a, and g_s is the strong coupling constant. The generators satisfy

$$[t^a, t^b] = if^{abc}t^c,$$

where f^{abc} are the structure constants of SU(3). SU(3) group has 8 generators, which indicates eight kinds of eigenvector fields $G^a_\mu (a = 1..8)$, named *gluons*. The transformation laws of Ψ and G^a_μ are

$$\begin{aligned} \Psi &\rightarrow (1 + i\alpha^a t^a)\Psi \\ G^a_\mu &\rightarrow G^a_\mu + \frac{1}{g_s}\partial_\mu \alpha^a + f^{abc}G^b_\mu \alpha^c. \end{aligned}$$

Similarly, $[D_\mu, D_\nu] = -ig_s(\partial_\mu G^a_\nu - \partial_\nu G^a_\mu + g_s f^{abc}G^b_\mu G^c_\nu)$. The $-ig_s f^{abc}G^b_\mu G^c_\nu$ term comes out because of the commutation relationship among t^a.

We then have the QCD Lagrangian which describes a spin $\frac{1}{2}$ field interacting with the gluon vector fields:

$$\mathcal{L}_{\text{QCD}} = i\bar{\Psi}\gamma^\mu D_\mu \Psi - m\bar{\Psi}\Psi - \frac{1}{4}G^a_{\mu\nu}G^{a\mu\nu}, \tag{2.10}$$

where $D_\mu = \partial_\mu - ig_s G^a_\mu t^a$; $G^a_{\mu\nu} \equiv \partial_\mu G^a_\nu - \partial_\nu G^a_\mu + g_s f^{abc}G^b_\mu G^c_\nu$.

Based on the asymptotic freedom theory [17], there are no more than 16 quark flavors. Because of the observed CP violation, there must be more than two generations of ($\geqslant 6$) quarks. Currently six quark flavors (three generations) have been discovered.

2.6 The Electro-weak Theory and the Spontaneously Broken Gauge Symmetries

The weak interaction was first introduced by Enrico Fermi in 1933 to explain beta decay [18]. The discovery of parity violation by Lee, Yang, and Wu in 1956 [19, 20] implies that the left-handed fields and right-handed fields act differently — there are only left-handed neutrinos and right-handed anti-neutrinos. By setting the left-handed doublet

$$\eta_L = \begin{bmatrix} \nu_{eL} \\ e_L \end{bmatrix} = \begin{bmatrix} \frac{1}{2}(1-\gamma_5)\nu_{eL} \\ \frac{1}{2}(1-\gamma_5)e \end{bmatrix}$$

and a right handed singlet

$$e_R = \frac{1}{2}(1+\gamma_5)e,$$

the experimentally proven gauge group is $\mathrm{SU}(2)_L \times \mathrm{U}(1)$. The left-handed and right-handed fields transform as

$$\begin{aligned} \begin{bmatrix} \nu_{eL} \\ e_L \end{bmatrix} &\rightarrow e^{i[\alpha^a(x)T^a + \beta(x)Y_L]} \begin{bmatrix} \nu_{eL} \\ e_L \end{bmatrix} \qquad (a = 1,2,3) \\ e_R &\rightarrow e^{i\beta(x)Y_R} e_R, \end{aligned}$$

where the SU(2) generators are

$$T^a = \frac{1}{2}\sigma^a \qquad (a = 1,2,3).$$

Because the electric charge of both e_L and e_R is $-e$:

$$e \begin{bmatrix} 0 & 0 \\ 0 & -1 \end{bmatrix} \begin{bmatrix} 0 \\ e_L \end{bmatrix} = -e \begin{bmatrix} 0 \\ e_L \end{bmatrix},$$

the electric charge operator $q_L = e \begin{bmatrix} 0 & 0 \\ 0 & -1 \end{bmatrix}$ for e_L and $q_R = -e$ for e_R.

Because

$$T_L^3 \begin{bmatrix} 0 \\ e_L \end{bmatrix} = \frac{1}{2} \begin{bmatrix} 1 & 0 \\ 0 & -1 \end{bmatrix} \begin{bmatrix} 0 \\ e_L \end{bmatrix} = -\frac{1}{2} \begin{bmatrix} 0 \\ e_L \end{bmatrix} \quad \text{and} \quad T_R^3 e_R = 0 \quad (\text{no } T^3 \text{ for } e_R),$$

where the subscript L indicates left-handed only, it is convenient to define the U(1) generators Y_L and Y_R as

$$\begin{aligned} Y_L \begin{bmatrix} 0 \\ e_L \end{bmatrix} &\equiv \left(\frac{q_L}{e} - T_L^3\right) \begin{bmatrix} 0 \\ e_L \end{bmatrix} = -\frac{1}{2} \begin{bmatrix} 1 & 0 \\ 0 & 1 \end{bmatrix} \begin{bmatrix} 0 \\ e_L \end{bmatrix} = -\frac{1}{2} \begin{bmatrix} 0 \\ e_L \end{bmatrix} \\ Y_R e_R &\equiv \left(\frac{q_R}{e} - T_R^3\right) e_R = -e_R. \end{aligned}$$

Y_L and Y_R are named as hypercharge. The eigenvalue of Y_L is $-\frac{1}{2}$ and of Y_R is -1. The corresponding gauge derivative is

$$D_{\mu L} = \partial_\mu - i g_W T^a A_\mu^a - i g_Y Y_L B_\mu$$

for a left-handed doublet and

$$D_{\mu R} = \partial_\mu - i g_Y Y_R B_\mu \tag{2.11}$$

for a right-handed singlet, where g_W and g_Y are constants. The corresponding Lagrangian is

$$\begin{aligned}\mathcal{L}_{\text{EWK}} &= (\eta_L)^\dagger\gamma^0\gamma^\mu(\partial_\mu - ig_W T^a A^a_\mu - ig_Y Y_L B_\mu)\eta_L + (e_R)^\dagger\gamma^0\gamma^\mu(\partial_\mu - ig_Y Y_R B_\mu)e_R \\ &\quad -\frac{1}{4}A^a_{\mu\nu}A^{a\mu\nu} - \frac{1}{4}B_{\mu\nu}B^{\mu\nu},\end{aligned}$$

where $A^a_{\mu\nu} = \partial_\mu A^a_\nu - \partial_\nu A^a_\mu - g_W\epsilon^{abc}A^b_\mu A^c_\nu$ and $B_{\mu\nu} = \partial_\mu B_\nu - \partial_\nu B_\mu$. $A^a_{\mu\nu}$ and $B_{\mu\nu}$ are the kinetic terms of the fields. ϵ^{abc} are the structure constants of SU(2).

Incorporating with the electro-weak facts that there are charge raising and charge lowering currents, to present the observable fields, we should choose the $T^\pm \equiv \frac{1}{2}(T^1 \pm iT^2) = \frac{1}{4}(\sigma^1 \pm i\sigma^2)$,

$$T^+ = \frac{1}{2}\begin{bmatrix}0 & 1\\ 0 & 0\end{bmatrix} \qquad T^- = \frac{1}{2}\begin{bmatrix}0 & 0\\ 1 & 0\end{bmatrix},$$

where $T^+ = (T^-)^\dagger$, instead of T^1 and T^2 as the SU(2) generators. Thus

$$qT^+\eta_L = 0 \quad \text{and} \quad qT^-T^+\eta_L = -\frac{1}{4}e\begin{bmatrix}0\\ e_L\end{bmatrix}.$$

Because

$$(A^1_\mu - iA^2_\mu)\frac{1}{2}(T^1 + iT^2) + (A^1_\mu + iA^2_\mu)\frac{1}{2}(T^1 - iT^2) = A^1_\mu T^1 + A^2_\mu T^2,$$

considering the normalization condition $\langle 0|\,(W^\pm_\mu)^\dagger W^{\pm\mu}\,|0\rangle = 1$, the corresponding charge raising and charge lowering observable gauge fields are

$$W^+_\mu = \frac{1}{\sqrt{2}}(A^1_\mu - iA^2_\mu) \quad \text{and} \quad W^-_\mu = \frac{1}{\sqrt{2}}(A^1_\mu + iA^2_\mu),$$

respectively, where $W^+_\mu = (W^-_\mu)^\dagger$.

Because the above mentioned model includes the electromagnetic field, the gauge field corresponding to one of the linear combinations of T^3 and Y_L presents the electromagnetic field. Because

$$q\frac{q}{-e}\begin{bmatrix}0\\ e_L\end{bmatrix} = -q(T^3 + Y_L)\begin{bmatrix}0\\ e_L\end{bmatrix} = q\begin{bmatrix}0\\ e_L\end{bmatrix} = -e\begin{bmatrix}0\\ e_L\end{bmatrix},$$

the generator of the electromagnetic field is $T^3_L + Y_L$ for left-handed neutrinos and electrons, and $T^3_R + Y_R = Y_R = -1$ for right-handed electrons.

Considering the normalization condition, one can have

$$g_W A^3 + g_Y Y_L B_\mu = \frac{1}{\sqrt{g^2_W + g^2_Y}}Z_\mu(g^2_W T^3 - g^2_Y Y_L) + \frac{g_W g_Y}{\sqrt{g^2_W + g^2_Y}}A^\gamma_\mu(T^3 + Y_L),$$

where

$$A_\mu^\gamma = \frac{1}{\sqrt{g_W^2 + g_Y^2}}(g_Y A_\mu^3 + g_W B_\mu),$$

which is massless. The field that is orthogonal to A_μ^γ is

$$Z_\mu = \frac{1}{\sqrt{g_W^2 + g_Y^2}}(g_W A_\mu^3 - g_Y B_\mu).$$

Written in terms of the observable fields, $W_\mu^\pm$, Z_μ, and A_μ^γ, the gauge derivative $D_{\mu L}$ becomes

$$\begin{aligned} D_{\mu L} &= \partial_\mu - i\frac{g_W}{\sqrt{2}}(W_\mu^+ T^+ + W_\mu^- T^-) - i\frac{1}{\sqrt{g_W^2 + g_Y^2}} Z_\mu (g_W^2 T^3 - g_Y^2 Y_L) \\ &\quad -i\frac{g_W g_Y}{\sqrt{g_W^2 + g_Y^2}} A_\mu^\gamma (T^3 + Y_L). \end{aligned}$$

For the right-handed $D_{\mu R}$, because the electromagnetic field A_μ^γ is just B_μ, the format stays the same with Equation 2.11.

Because of the observed momentum changes in charge raising and lowering β decays, $W_\mu^\pm$ have to be massive. Since the gauge field A_μ^a is not gauge invariant, the mass term $(W_\mu^\pm)^\dagger W^{\mu\pm}$ cannot exist in the Lagrangian. The discussions of the vacuum expectation values solve the problem, which is called the spontaneously broken gauge symmetries or Higgs mechanism.

The vacuum can be defined as the state with the lowest possible energy (ground state) in Hilbert space. However, the fields still exist in this case. Consider a scalar field: to couple it with the $\mathrm{SU}(2)_L \times \mathrm{U}(1)$ electro-weak gauge fields, the scalar field has to be expressed as a doublet,

$$H \equiv \frac{1}{\sqrt{2}} \begin{bmatrix} H^a \\ H^b \end{bmatrix},$$

where the factor $\frac{1}{\sqrt{2}}$ is for normalization.

Summing up all possible terms for a scalar field mentioned in section 2.3 and assigning them with factors, the Lagrangian in terms of this scalar field is

$$\mathcal{L}_H = (\partial_\mu - ig_W T^a A_\mu^a - ig_Y Y_L B_\mu) H^\dagger (\partial^\mu - ig_W T^b A^{b\mu} - ig_Y Y_L B^\mu) H - \mu^2 H^\dagger H - \frac{\lambda}{2}(H^\dagger H)^2.$$

If $\lambda > 0$ and $\mu^2 < 0$, there is a vacuum expectation value at the stationary point of the Lagrangian: $\langle H \rangle^\dagger \langle H \rangle \equiv v^2 = \mu^2/\lambda$. The mass of H is μ^2.

One can always perform an SU(2)$_L$×U(1) electro-weak gauge transformation so that $H^a = 0$ and H^b is Hermitian. Thus the expectation value of the field, presented as $\langle H \rangle$, is

$$\frac{1}{\sqrt{2}} \begin{bmatrix} 0 \\ v \end{bmatrix}.$$

The vacuum interacting with the SU(2)$_L$×U(1) electro-weak gauge fields yields the masses of the gauge bosons:

$$\begin{aligned} & \frac{1}{2} \begin{bmatrix} 0 & v \end{bmatrix} (\partial_\mu - g_W T^a A^a_\mu - g_Y Y_L B_\mu)(\partial^\mu - g_W T^b A^{b\mu} - g_Y Y_L B^\mu) \begin{bmatrix} 0 \\ v \end{bmatrix} \\ = \; & \frac{v^2}{4} \frac{g_W^2}{2} (A^1_\mu A^{1\mu} + A^2_\mu A^{2\mu}) + \frac{v^2}{8} (g_W A^3_\mu + 2 g_Y Y_L B_\mu)(g_W A^{3\mu} + 2 g_Y Y_L B^\mu) \\ & \text{(diagonalize)} \rightarrow \\ = \; & \left(\frac{1}{2} v g_W \right)^2 (W^-_\mu)^\dagger W^{-\mu} + \frac{1}{8} v^2 (g_W^2 + g_Y^2) Z^\dagger_\mu Z^\mu + 0 A^\gamma_\mu A^{\gamma\mu}. \end{aligned}$$

It is clear that the mass of $W^\pm_\mu$ is $\frac{1}{2} v g_W$, the mass of Z_μ is $\frac{1}{2} v \sqrt{g_W^2 + g_Y^2}$, and the mass of A^γ_μ is zero, which is the electromagnetic vector field. The following table shows the recent experimentally measured values of the $W^\pm_\mu$, the Z_μ, and the H masses. No evidence shows that the electromagnetic field is massive.

Field	$W^\pm_\mu$	Z_μ	H
Mass (GeV)	80.385 ± 0.015 [21]	91.1876 ± 0.0021 [21]	125.3±0.6 (CMS [10]) 125.5±0.6 (ATLAS [11])

Table 2.1: The experimental values of the SU(2)$_L$ × $U(1)$ gauge fields masses and the Higgs field mass.

The above-mentioned theory is called *the Glashow-Weinberg-Salam theory of electro-weak interactions* [14]. The scalar field H that couples with the SU(2)$_L$×U(1) vector gauge fields is called *the Higgs field*. The charged $W^\pm_\mu$ fields are called *the standard model W bosons*. The neutral Z field is called *the standard model Z boson* (noted as Z).

2.7 The Standard Model

Because the SU(2)$_L$ doublet η_L and the U(1) singlet belong to different groups and have different Y eigenvalues, it is not possible to write a mass term like $\bar{\Psi}\Psi$ which is

both Hermitian and gauge invariant. Terms $e_L^\dagger \gamma^0 e_L$ and $e_R^\dagger \gamma^0 e_R$ are just zero. Terms $e_R^\dagger \gamma^0 e_L$ and $e_L^\dagger \gamma^0 e_R$ cannot be written because of different Y eigenvalues. The mass of the leptons can be derived from the Yukawa couplings with the Higgs field:

$$\Delta\mathcal{L}_{e-H} = -\lambda_e \eta_L^\dagger \gamma^0 H e_R - \lambda_e (H e_R)^\dagger \gamma^0 \eta_L.$$

If H is on its ground state,

$$\Delta\mathcal{L}_{e-\langle H\rangle} = -\frac{1}{\sqrt{2}}\lambda_e v e_L^\dagger \gamma^0 e_R - \frac{1}{\sqrt{2}}\lambda_e v e_R^\dagger \gamma^0 e_L,$$

and $m_e = \frac{1}{\sqrt{2}}\lambda_e v$. If there is more than one generation leptons,

$$\Delta\mathcal{L}_{l-H} = -\lambda_l^I \ell_L^{I\,\dagger} \gamma^0 H l_R^I - \lambda_l^I (H l_R^I)^\dagger \gamma^0 \ell_L^I.$$

Until now we observed three generations of leptons, so $I = 1, 2, 3$. The repeated generation index is summed, where

$$\ell_{L1} = \begin{bmatrix} \nu_e \\ e_L \end{bmatrix}, \ell_{L2} = \begin{bmatrix} \nu_\mu \\ \mu_L \end{bmatrix}, \ell_{L3} = \begin{bmatrix} \nu_\tau \\ \tau_L \end{bmatrix}, l_{R1} = e_R, l_{R2} = \mu_R, \text{ and } l_{R3} = \tau_R.$$

Note that there is no interactions among different generations, which preserves the lepton number.

To combine the electro-weak theory with QCD, because up and down quarks are able to transfer to each other though the weak interactions, $d + W^+ \to u$, similar to $e^- + W^+ \to \nu_e$, the left-handed up and down quarks can be assigned into a SU(2) doublet,

$$q_L = \begin{bmatrix} u_L \\ d_L \end{bmatrix}.$$

Because the gluon corresponds to the SU(3) group, left-handed quarks are thus in the SU(3)×SU(2)$_L$×U(1) group. The right-handed up and down quarks, which do not couple with the SU(2)$_L$ group, are treated separately. They belong to the SU(3)×U(1) group. Quarks gain masses in a similar way as the leptons. Considering one generation, the Lagrangian can be written as

$$\Delta\mathcal{L}_{q-H} = -\lambda_u q_L^\dagger \gamma^0 H u_R - \lambda_u (H u_R)^\dagger \gamma^0 q_L - \lambda_d q_L^\dagger \gamma^0 H d_R - \lambda_d (H d_R)^\dagger \gamma^0 q_L.$$

With H in its ground state, the masses come out to be $m_u = \frac{1}{\sqrt{2}}\lambda_u v$ and $m_d = \frac{1}{\sqrt{2}}\lambda_d v$.

Because it is observed that the quarks can transit among generations, e.g. $s \to u + W^-$, so it is better to write down either up or down type quarks in the doublets as mixed states so that there will be diagnalized real Yukawa coupling constants.

Theoretically there must be at least three generations to account for the T and CP violation and to match the experimental observations [22]. In the modern convention, we write down the three left-handed quark doublets as:

$$\begin{aligned} Q_L^1 &= \begin{bmatrix} u_L \\ V_{ud}d_L + V_{us}d_L + V_{ub}b_L \end{bmatrix} \\ Q_L^2 &= \begin{bmatrix} c_L \\ V_{cd}d_L + V_{cs}d_L + V_{cb}b_L \end{bmatrix} \\ Q_L^3 &= \begin{bmatrix} t_L \\ V_{td}d_L + V_{ts}d_L + V_{tb}b_L \end{bmatrix}. \end{aligned}$$

For right-handed quarks, we do it in the same way as for the left-handed quarks. The 3×3 matrix V is called the Cabibbo-Kobayashi-Maskawa(CKM) matrix. Because the direct transitions (leading order) among different generations of down type quarks are not observed

$$\left[\text{no leading order} \qquad K^0(d\bar{s}) \leftrightarrow \bar{K^0}(\bar{d}s)\right],$$

three restrictions should be applied on the CKM matrix elements. We can drop another three free elements in the CKM matrix into the down type quark mass terms. Thus the CKM matrix has $9 - 3 - 3 + 1$(total phase) $= 4$ free parameters. They can be written in three Euler angles (θ_{12}, θ_{23}, θ_{13}) indicating the transition of quark generations i and j and one CP-violating phase δ [23]. Figure 2.1 pictorially shows the strength of the V_{ij}.

Thus the three generations quarks Lagrangian can be written as

$$\Delta\mathcal{L}_{q-H} = -\lambda_u^I {Q_L^I}^\dagger \gamma^0 H u_R^I - \lambda_u^I (H u_R^I)^\dagger \gamma^0 Q_L^I - \lambda_d^I {Q_L^I}^\dagger \gamma^0 H d_R^I - \lambda_d^I (H d_R^I)^\dagger \gamma^0 Q_L^I,$$

where $I = 1, 2, 3$.

As a result, combing all results mentioned above, we can write down a Lagrangian that describes the electro-weak and the strong interactions among fields, which is the Standard Model:

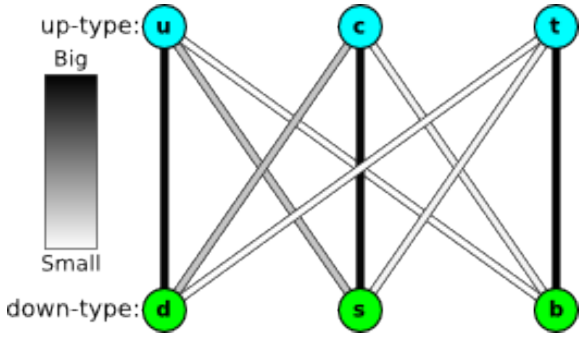

Figure 2.1: A pictorial representation of the Cabibbo-Kobayashi-Maskawa matrix that shows the strength of quark flavor-changing weak decays [24].

$\mathcal{L}_{\rm SM} =$	
$-\frac{1}{4}A^a_{\mu\nu}A^{a\mu\nu} - \frac{1}{4}B_{\mu\nu}B^{\mu\nu}$	$W^\pm_\mu$, Z_μ, A^γ_μ(photon) kinetic energies and self-interactions ($a = 1..3$)
$+[(\partial_\mu - ig_W T^a A^a_\mu - ig_Y Y^l_L B_\mu)H]^\dagger$ $(\partial^\mu - ig_W T^a A^{a\mu} - ig_Y Y^l_L B^\mu)H$	kinetic energy of H and its interactions with $W^\pm_\mu$, Z_μ, A^γ_μ ($a = 1..3$, $Y^l_L = -\frac{1}{2}$)
$-\mu^2 H^\dagger H - \frac{\lambda}{2}(H^\dagger H)^2$	potential energy of H, also H mass term
$+(\ell_{LI})^\dagger\gamma^0\gamma^\mu(\partial_\mu - ig_W T^a A^a_\mu - ig_Y Y^l_L B_\mu)\ell_{LI}$	left-handed lepton kinetic energies and their interactions with $W^\pm_\mu$, Z_μ, A^γ_μ ($I = 1, 2, 3$, $Y^l_L = -\frac{1}{2}$)
$+(\ell_{RI})^\dagger\gamma^0\gamma^\mu(\partial_\mu - ig_Y Y^l_R B_\mu)\ell_{RI}$	right-handed lepton kinetic energies and their interactions with B_μ ($I = 1, 2, 3$, $Y^l_R = -1$)
$-\lambda^I_l \ell^\dagger_{LI}\gamma^0 H l_{RI} - \lambda^I_l (H l_{RI})^\dagger\gamma^0\ell_{LI}$	leptons coupling to Higgs ($I = 1, 2, 3$)
$-\frac{1}{4}G^b_{\mu\nu}G^{b\mu\nu} + \frac{g_s^2\theta}{32\pi^2}G^b_{\mu\nu}\epsilon^{\alpha\beta\mu\nu}G^b_{\alpha\beta}$	gluon kinetic energy and a possible but not seen CP violation gluon kinetic energy term ($b = 1..8$)
$+(Q_{LI})^\dagger\gamma^0\gamma^\mu(\partial_\mu - ig_W T^a A^a_\mu - ig_Y Y^I_L B_\mu - ig_s t^b G^b_\mu)Q_{LI}$	left-handed quark kinetic energies and their interactions with $W^\pm_\mu$, Z_μ, A^γ_μ, and G^b_μ ($I = 1, 2, 3$, $a = 1..3$, $b = 1..8$, $Y^I_L = +\frac{1}{6}$)
$+(u_{RI})^\dagger\gamma^0\gamma^\mu(\partial_\mu - ig_Y Y^I_{Ru} B_\mu - ig_s t^b G^b_\mu)u_{RI}$ $+(d_{RI})^\dagger\gamma^0\gamma^\mu(\partial_\mu - ig_Y Y^I_{Rd} B_\mu - ig_s t^b G^b_\mu)d_{RI}$	right-handed quark kinetic energies and their interactions with B_μ and G^b_μ ($I = 1, 2, 3$, $b = 1..8$, $Y^I_{Ru} = +\frac{2}{3}$, $Y^I_{Rd} = -\frac{1}{3}$)
$-\lambda^I_u {Q^I_L}^\dagger\gamma^0 H u^I_R - \lambda^I_u (H u^I_R)^\dagger\gamma^0 Q^I_L$ $-\lambda^I_d {Q^I_L}^\dagger\gamma^0 H d^I_R - \lambda^I_d (H d^I_R)^\dagger\gamma^0 Q^I_L$.	quarks coupling to Higgs ($I = 1, 2, 3$, Q^I_Ls are written with the CKM matrix.)

2.8 The Minimum Stueckelberg Extension

A mass term for the gauge bosons like $C_\mu C^\mu$ is not gauge invariant. If another scalar field transforms together with the C_μ and cancels the gauge broken terms, the total Lagrangian can be gauge invariant. Suggested by this idea, the prototype Stueckelberg Lagrangian reads

$$\mathcal{L}_{\text{prototype-Stu}} = -\frac{1}{4}C_{\mu\nu}C^{\mu\nu} - \frac{1}{2}(\partial_\mu\sigma + M_1 C_\mu)(\partial^\mu\sigma + M_1 C^\mu),$$

where the C_μ is an abelian vector boson in a hypothetical dimension $U(1)_X$ and the σ is a pseudo-scalar field. $C_{\mu\nu} \equiv \partial_\mu C_\nu - \partial_\nu C_\mu$. The σ transforms together with C_μ:

$$\begin{aligned} C_\mu &\rightarrow C_\mu + \partial_\mu \epsilon_X \\ \sigma &\rightarrow \sigma - M_1 \epsilon_X, \end{aligned}$$

and thus the Lagrangian is invariant under $U(1)_X$[25, 26].

To decouple the C_μ and σ, the model defines a gauge. The gauge fixing term that is invariant in the gauge transformation reads [27]

$$-\frac{1}{2\xi}(\partial_\mu C^\mu + \xi M_1 \sigma)(\partial^\mu C_\mu + \xi M_1 \sigma).$$

By adding the gauge fixing term and setting the boundary condition $\lim_{x\to\infty} C_\mu \sigma \rightarrow 0$, terms $-M_1(C^\mu\partial_\mu\sigma + \sigma\partial_\mu C^\mu)$ disappear in the action S so that the C_μ decouples with σ. The total Lagrangian reads

$$\mathcal{L}_{\text{prototype-Stu}} = -\frac{1}{4}C_{\mu\nu}C^{\mu\nu} - \frac{{M_1}^2}{2}C_\mu C^\mu - \frac{1}{2\xi}\partial_\mu C^\mu \partial^\mu C_\mu - \frac{1}{2}\partial_\mu\sigma\partial^\mu\sigma - \xi\frac{{M_1}^2}{2}\sigma^2.$$

For the minimal extension of the standard model Lagrangian by the Stueckelberg mechanism, we assume the scalar field σ couples with the abelian gauge bosons, the hypercharge field B_μ and the C_μ. Because of the gauge invariance, the scalar field σ also transforms together with the hypercharge field B_μ:

$$\begin{aligned} B_\mu &\rightarrow B_\mu + \partial_\mu \epsilon_Y \\ \sigma &\rightarrow \sigma - M_2 \epsilon_Y. \end{aligned}$$

Because C_μ does not couple with any standard model fields, the gauge derivatives for the standard model fermions are not changed. Thus, the Lagrangian of the minimum Stueckelberg extension is

$$\begin{aligned} \mathcal{L}_{\text{Stu}} &= -\frac{1}{4}C_{\mu\nu}C^{\mu\nu} + g_X C_\mu J^\mu_X - \frac{1}{2}(\partial_\mu\sigma + M_1 C_\mu + M_2 B_\mu)(\partial^\mu\sigma + M_1 C^\mu + M_2 B^\mu) \\ &\quad \boxed{-\frac{1}{2\xi_1}(\partial_\mu C^\mu + \xi_1 M_1\sigma)(\partial^\mu C_\mu + \xi_1 M_1\sigma) - \frac{1}{2\xi_2}(\partial_\mu B^\mu + \xi_2 M_2\sigma)(\partial^\mu B_\mu + \xi_2 M_2\sigma)}, \end{aligned}$$

where the gauge fixing terms are boxed. J_X^μ is the current in the hidden sector, which does not contain any field in the standard model.

Adding $\mathcal{L}_{\rm Stu}$ to the standard model Lagrangian $\mathcal{L}_{\rm SM}$, the mass matrix of (C_μ, B_μ, A_μ^3) reads

$$\mathcal{L}_{\text{mass of } (C_\mu,B_\mu,A_\mu^3)} = \frac{1}{2}\begin{bmatrix} C_\mu & B_\mu & A_\mu^3 \end{bmatrix} \begin{bmatrix} M_1^2 & M_1M_2 & 0 \\ M_1M_2 & M_2^2+\frac{1}{2}g_Y^2v^2 & -\frac{1}{4}g_Wg_Yv^2 \\ 0 & -\frac{1}{4}g_Wg_Yv^2 & \frac{1}{4}g_W^2v^2 \end{bmatrix} \begin{bmatrix} C_\mu \\ B_\mu \\ A_\mu^3 \end{bmatrix},$$

where $v^2 = \frac{4}{g_W^2}{M_{\rm W}}^2$ and where $M_{\rm W}$ is the standard model W boson mass.

Diagonalizing this mass term, we get three eigenvalues: $M_+, M_-, 0$, where

$$M_\pm^2 = \frac{1}{2}[{M_{\rm Z}}^2 + M_1^2(1+\epsilon^2)] \pm \frac{1}{2}\sqrt{[{M_{\rm Z}}^2 + M_1^2(1+\epsilon^2)]^2 - 4M_1^2({M_{\rm Z}}^2 + M_{W^\pm}^2\epsilon^2)},$$

and where $M_{\rm Z} = v\sqrt{(g_W^2+g_Y^2)/2}$, which is the standard model predicted Z boson mass, $\epsilon = M_2/M_1$. Thus the mass of the Z is predicted as M_- and a new particle $\mathrm{Z}'_{\rm St}$ with mass $M_{\mathrm{Z}'_{\rm St}} = M_+$ is indicated. In the limit of $\epsilon \to 0$ (large $\mathrm{Z}'_{\rm St}$ mass limit), the Stueckelberg sectors decouple with the Standard Model. The current experimental value of $M_{\rm Z} = 91.1876 \pm 0.0021\text{GeV}$ (Table 2.1) constrains ϵ to be

$$|\epsilon| \lessapprox 0.061\sqrt{1-\left(\frac{M_{\rm Z}}{M_1}\right)^2}\ [28]. \tag{2.12}$$

The observable fields $(Z'_\mu, Z_\mu, A_\mu^\gamma)$ are connected with the fields (C_μ, B_μ, A_μ^3) as [28]:

$$(Z'_\mu, Z_\mu, A_\mu^\gamma)_j = R_{ij}(C_\mu, B_\mu, A_\mu^3)_i,$$

where

$$R_i = \frac{1}{\sqrt{\left(\frac{\epsilon M_1^2}{-t_W {M_{\rm W}}^2}\frac{{M_{\rm W}}^2-\lambda_i}{M_1^2-\lambda_i}\right)^2 + \left(\frac{{M_{\rm W}}^2-\lambda_i}{t_W {M_{\rm W}}^2}\right)^2 + 1}} \begin{bmatrix} \frac{\epsilon M_1^2}{-t_W {M_{\rm W}}^2}\frac{{M_{\rm W}}^2-\lambda_i}{M_1^2-\lambda_i} \\ \frac{{M_{\rm W}}^2-\lambda_i}{t_W {M_{\rm W}}^2} \\ 1 \end{bmatrix},$$

and where $t_w = g_Y/g_W$, $\lambda_i = \{M_+, M_-, 0\}$.

The visible neutral current part of the $\mathcal{L}_{\rm Stu} + \mathcal{L}_{\rm SM}$ is thus given by

$$\mathcal{L}_{\text{NC of (Stu+SM)}} = \sum_{\text{fermions}} \Bigg\{ \frac{\sqrt{g_W^2+g_Y^2}}{2}\bar{f}\gamma^\mu[(v_f-\gamma^5 a_f)Z_\mu + (v'_f-\gamma^5 a'_f)\mathrm{Z}'_{\mathrm{St}\mu}]f + e' A_\mu^\gamma(\bar{f}\gamma^\mu Y_f f + \bar{f}\gamma^\mu T^3 f)\Bigg\},$$

where

$$\begin{aligned}
\frac{1}{e'^2} &= \frac{1}{g_W^2} + \frac{1}{g_Y^2}(1+\epsilon^2) \\
v'_f &= \frac{1}{\sqrt{g_W^2+g_Y^2}}(g_W R_{31} - g_Y R_{21})T_f^3 + 2Q_f g_Y R_{22} \\
a'_f &= \frac{1}{\sqrt{g_W^2+g_Y^2}}(g_W R_{31} - g_Y R_{21})T_f^3,
\end{aligned} \tag{2.13}$$

and where the Y_f is the hypercharge of f and T_f^3 is the projection of f on the T^3 dimension. The vector and axial vector (V-A) coupling constants are v'_f and a'_f.

Thus the fermions branching ratio of the $\mathrm{Z}'_{\mathrm{St}}$ can be calculated from the v'_f and a'_f [28].

The W^+W^- decay widths determined from the triple gauge boson vertex [28],

$$\mathcal{L}_{\mathrm{Z}'_{\mathrm{St}}\to WW} = ig_W R_{31}(W^+_{\mu\nu}W^{-\mu}\mathrm{Z}'^{\ \nu}_{\mathrm{St}} + W^-_{\mu\nu}W^{+\nu}\mathrm{Z}'^{\ \mu}_{\mathrm{St}} + W^{+\mu}W^{-\nu}\mathrm{Z}'_{\mathrm{St}\mu\nu}),$$

where $W^\pm_{\mu\nu} \equiv \partial_\mu W^\pm_\nu - \partial_\nu W^\pm_\mu$, $\mathrm{Z}'_{\mathrm{St}\mu\nu} \equiv \partial_\mu \mathrm{Z}'_{\mathrm{St}\nu} - \partial_\nu \mathrm{Z}'_{\mathrm{St}\mu}$.

Figure 2.2 shows the calculated branching ratios of the $\mathrm{Z}'_{\mathrm{St}}$ into $\bar{f}f$ and W^+W^- final states with $\epsilon = 0.06$. The large branching ratio of the $\mathrm{Z}'_{\mathrm{St}}$ into charged leptons (shown as the green line in Figure 2.2) makes it the major distinguishing channel to search [28].

2.9 Observation — Cross Section

If one wants to find out the substructure of an item, the scale of the probe must be equal or smaller than the target's. Based on this concept, to know the interactions among the elementary particles, we have to use the particles as probes for themselves, because we know nothing smaller. In order to penetrate deep into the particles, the particles are accelerated close to the speed of light and then collide with other particles. By collecting information from the collisions, we count different kinds of events and turn them into statistical results. That has been the basic method for particle physics over a hundred years. In the following section, I introduce the theory of such collisions briefly.

2.9.1 Definition of Cross Section

Suppose that inside bunch A and bunch B cross area A, bunch A has N_A scatterers, bunch B has N_B scatterers and the number of observed scattering events is N, the

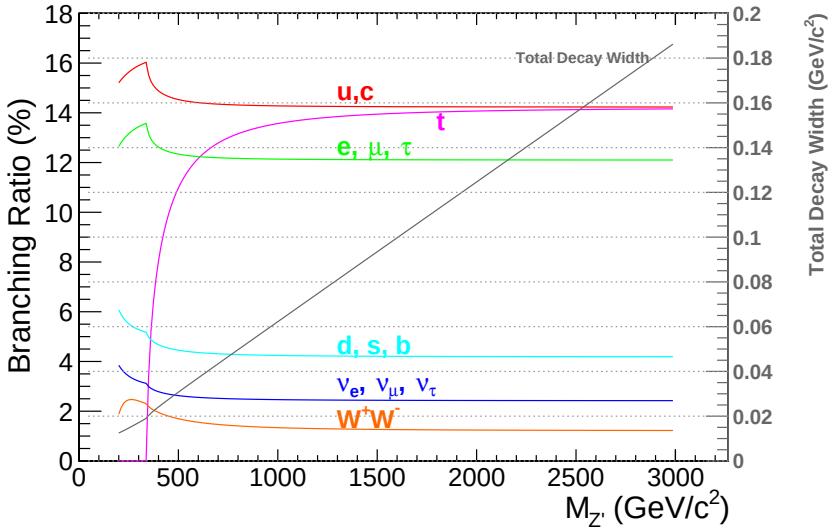

Figure 2.2: The Z'_{St} branching ratios into $\bar{f}f$ and W^+W^- final states as a function of $M_{Z'_{St}}$ with $\epsilon = 0.06$. The gray line shows the total decay width of all visible channels with $\epsilon = 0.06$, assuming the Z'_{St} only couples to the SM fields.

cross section σ is defined as

$$\sigma \equiv N \cdot \frac{A}{N_A N_B}, \tag{2.14}$$

which is interpreted as "the scattering area per scatterer". The quantity $\frac{N_A N_B}{A}$ is called the luminosity, which is interpreted as "the number of incident pairs per area".

The luminosity depends on the collider and the accelerator. The cross section depends only on the physics models, which is calculated theoretically. The number of scattering events is the sum of the probabilities of all possible initial and final states. Each probability is the quadratic mode of the projection of the initial state onto the final state, which is expressed as

$$N = \sum_{\substack{\text{all incident} \\ \text{pairs}}} P_i, \text{ where } P_i = |_{\text{out}} \langle \phi_1 \phi_2 \cdots | \, \phi_A \phi_B \rangle_{\text{in}} |^2.$$

We can differentiate the cross section and write it down in the final state momentum space,

$$\mathrm{d}\sigma = \frac{1}{2E_A 2E_B |v_A - v_B|} \prod_f \frac{\mathrm{d}^3 p_f}{(2\pi)^3} \frac{1}{2E_f} |M(p_A, p_B \to p_f)|^2 (2\pi)^4 \delta^{(4)}(p_A + p_B - \sum_f p_f),$$

where the E_A and E_B are the energies of particles in bunch A and B, v_A and v_B are their velocities, p_A and p_B are their momenta, p_f indicates the momenta of particles

in the final states, and where f runs over the final states particles, the elements of matrix M is defined in the momentum space as,

$$\begin{aligned}
{}_{\text{out}}\langle p_1 p_2 \cdots | \, p_A p_B \rangle_{\text{in}} &= \underbrace{\langle p_1 p_2 \cdots |}_{T\to+\infty} \underbrace{| p_A p_B \rangle}_{T\to-\infty} \\
&= \lim_{T\to\infty} \langle p_1 p_2 \cdots | \, e^{-iH(2T)} \, | p_A p_B \rangle \\
&= \langle p_1 p_2 \cdots | \, p_A p_B \rangle \\
&\quad + (2\pi)^4 \delta^{(4)}(p_A + p_B - \sum_f p_f) \cdot i\mathcal{M}(p_A, p_B \to p_f),
\end{aligned}$$

where T is the time and H is the Hamiltonian of the interaction. The first term is elastic scattering, which is not interesting and can be dropped. The LSZ reduction [29] proves that the $\mathcal{M}$ matrix is the sum of all connected and amputated Feynman diagrams with p_A, p_B incoming particles and p_f outgoing particles. The $\mathcal{M}$ matrix can be computed by the perturbation theory, calculating the Feynman diagrams or propagators order by order.

2.9.2 Drell–Yan process cross section in CMS

The Drell–Yan process produces the majority of Z, γ, and Z′ in CMS. The $\mathrm{Z}/\gamma/\mathrm{Z}' \to \ell^+\ell^-$ process is the most significant channel in the experiment and is the main subject of this thesis. In CMS, the leading order(LO) diagram of the major Drell–Yan process reads:

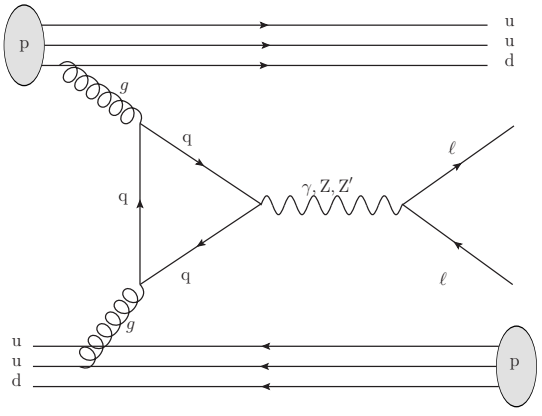

Figure 2.3: The leading order (LO) diagram of the major Drell–Yan process in CMS.

In the latter Feynman diagrams, we only consider the interaction among partons (the diagram after the $q\bar{q}$ part in Figure 2.3).

The QCD corrected next leading order(NLO) Feynman diagram reads

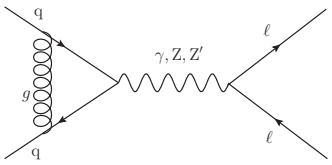

Some of the electro-weak(EW, QED) next leading order(NLO) corrections to the QCD leading order Feynman diagrams read

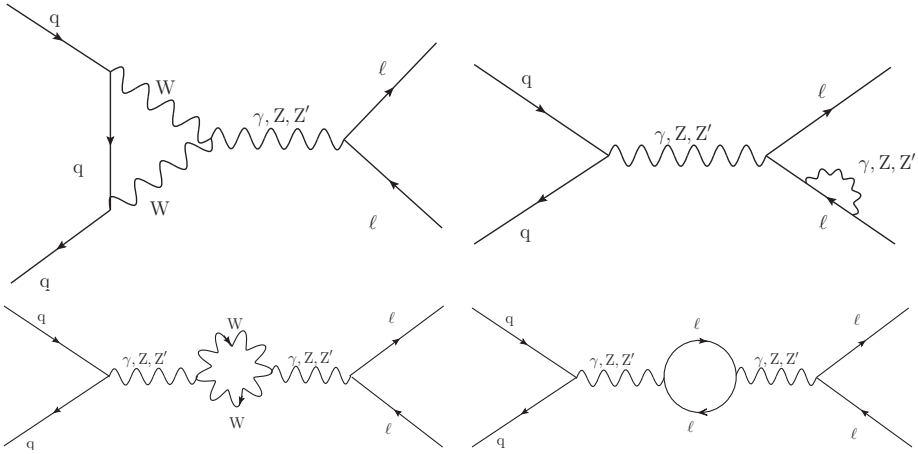

Combining the QCD and EW NLO becomes corrections complicated. The following diagrams show a few examples of them,

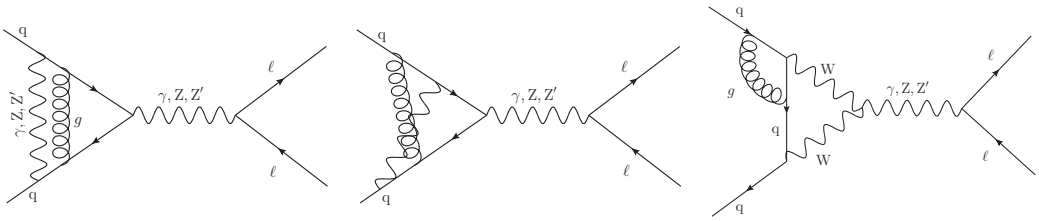

For the pure QCD case, the differential cross section $\mathrm{d}\sigma$ is proportional to

$$(\alpha_s)^{(2+n_{\mathrm{QCD}})} \approx (0.118)^{(2+n_{\mathrm{QCD}})}.$$

For the QCD⊗EW correction terms, $\mathrm{d}\sigma$ is proportional to

$$(\alpha_s)^{(2+n_{\mathrm{QCD}})}(\alpha)^{n_{\mathrm{EW}}} \approx (0.118)^{(2+n_{\mathrm{QCD}})}(0.0073)^{n_{\mathrm{EW}}} \text{ [21]},$$

where for the LO, $n_{\mathrm{QCD/EW}} = 0$, for the NLO, $n_{\mathrm{QCD/EW}} = 1$, and so on. Thus the magnitude factor of $\mathrm{d}\sigma$ of the NNLO QCD correction terms is $0.118^{2+2} = 0.00019$, that of the NLO EW correction terms is $0.0073^1 = 0.0073$, and that of the NNLO EW

correction terms is $0.0073^2 = 0.00005$. It is reasonable to keep the LO+NLO+NNLO QCD corrected terms and the the NLO EW correction terms[4].

As seen in Figure 2.3, if the collision energy is high enough, the proton should be considered as a collection of quarks and only part of its energy will join the reaction. The parton momentum distribution function (PDF) $f_i(x)$ describes the probability that the interacting parton i carries a fraction x of the proton's momentum. As a result, from proton to parton [30],

Initial Energy	E	$\rightarrow$	xE
Initial Longitudinal Momentum	p_{L}	$\rightarrow$	xp_{L}
Initial Transverse Momentum	$p_{\mathrm{T}} = 0$	$\rightarrow$	$xp_{\mathrm{T}} = 0$
Initial Mass	M	$\rightarrow$	xM

The CTEQ6L1 [31] PDF sets that we used in this analysis are tuned particularly for LHC proton-proton interactions. The uncertainties of the PDF in the detector acceptance will be discussed in Section 4.5.1 and will not be considered in the calculations in this section.

Based on the ZWPROD [32, 33, 34] and the CTEQ6L1 [31] PDF set, at the center of mass energy, $\sqrt{s} = 7\,\mathrm{TeV}$ at the LHC, and using the CTEQ6L1 PDF set, the ratio of the LO+NLO+NNLO QCD corrected cross section to the LO cross section of the Drell–Yan process is calculated. This ratio is called *k-factor*. Figure 2.4 shows the k-factor versus the invariant mass of the dilepton. The fitted k-factor function

$$k = 1.23312 - 0.154901\frac{m_{\ell\ell} - 1000}{1000} + 0.0516781\left(\frac{m_{\ell\ell} - 1000}{1000}\right)^2$$

and the fitted k-factor error function

$$\delta k = 9.96^{-3}\ln\left(\frac{m_{\ell\ell}}{250}\right) \tag{2.15}$$

are used in the signal extraction fitting and DY background estimation, where $m_{\ell\ell}$ is in units of GeV.

In conclusion, the theoretical calculation of the cross sections of the γ, Z, and Z$'$ were done at QCD LO+NLO+NNLO level with uncertainties and the CTEQ6L1 PDF set.

[4]It is what we did for the DY background in the 2012 analysis. In the 2011 analysis and the signal cross section calculation, only LO+NLO+NNLO QCD corrected terms are considered. For the signal cross section calculations, only the QCD corrections are considered.

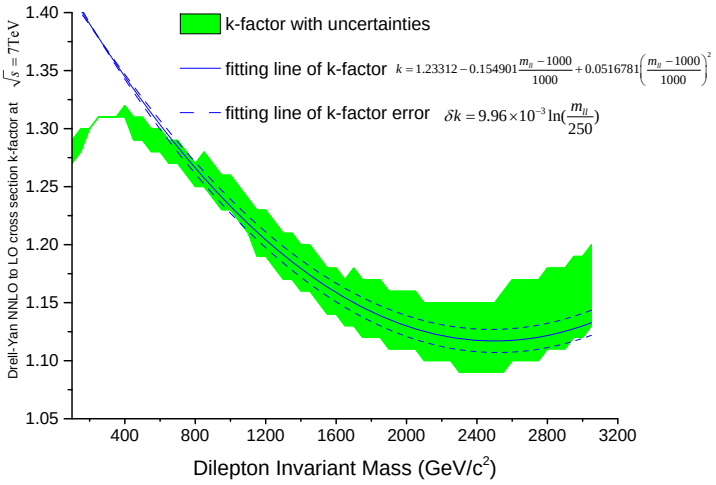

Figure 2.4: The ZWPROD calculated ratio of up to the NNLO QCD cross section (with uncertainties) to the LO cross section of the Drell–Yan process versus the invariant mass of the dilepton. The blue solid line shows the quadratic fitting function of the k-factor. The blue solid line show the fitting function of the k-factor error. (based on the CMS internal note AN-2010-312 Table 7)

2.9.3 Drell–Yan Cross Section in Terms of Up and Down Quark Coupling Constants (C_u and C_d)

The cross section of the Drell–Yan process can be written in terms of the Z′ couplings to up and down quark [35]:

$$\sigma(pp \to \mathrm{Z}' + X \to \ell^+\ell^- + X) = \frac{\pi}{48s}[C_u W_u(s, M^2_{\mathrm{Z}'}) + C_d W_d(s, M^2_{\mathrm{Z}'})], \qquad (2.16)$$

where $W_u(s, M^2_{\mathrm{Z}'})$ and $W_d(s, M^2_{\mathrm{Z}'})$ only depend on the collision energy and the Z′ mass but does not depend on the neutral boson. C_u and C_d depend on the Z or Z′ model, which can be expressed by the the vector and axial vector coupling constants:

$$\begin{aligned} C_u &= \frac{g_W^2 + g_Y^2}{2}({v'_u}^2 + {a'_u}^2)Br(\mathrm{Z}' \to \ell^+\ell^-) \\ C_d &= \frac{g_W^2 + g_Y^2}{2}({v'_d}^2 + {a'_u}^2)Br(\mathrm{Z}' \to \ell^+\ell^-), \end{aligned}$$

where g_W and g_Y are the weak interaction constants, introduced in section 2.6; v'_u, a'_u, v'_d, and a'_d are the V-A coupling constants defined in Equation 2.13; $Br(\mathrm{Z}' \to \ell^+\ell^-)$ is the branching ratio of the Z′ decaying to lepton and anti-lepton pair (one generation).

For the Stueckelberg mechanism, the V-A coupling constants to fermions depend on the $\mathrm{Z}'_{\mathrm{St}}$ mass, which results in both C_u and C_d depending on the $\mathrm{Z}'_{\mathrm{St}}$ mass. Figure 2.5 shows this dependence.

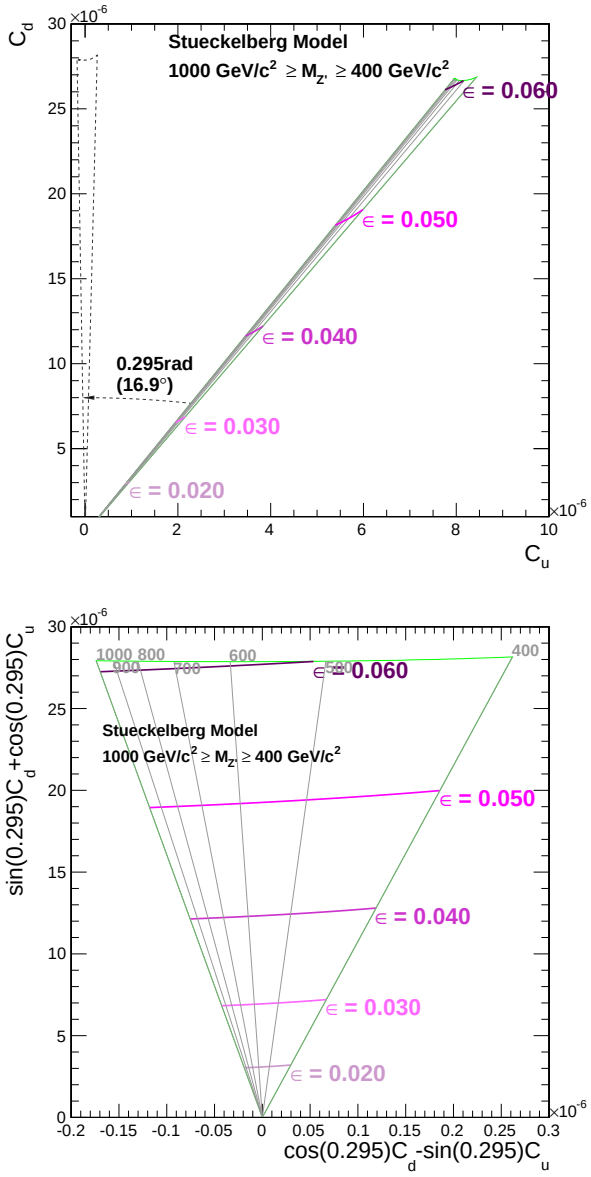

Figure 2.5: The Z'_{St} in the (C_d, C_u) plane where the ϵ constraint (Equation 2.12) from the uncertainty of the SM Z boson mass is considered. The ϵ dependence is shown by magenta lines. Along each line the mass varies from 400 GeV to 1000 GeV. The mass dependence is shown by gray lines. On the top plot, the lower gray line corresponds to $M_{Z'_{St}} = 400$ GeV and the upper gray line corresponds to 1000 GeV. On the bottom plot, the coordinate of (C_d, C_u) is rotated by 0.295 rad counterclockwise, as indicated by the axis title, in order to have a clear view of $(M_{Z'_{St}}, \epsilon)$ to (C_d, C_u) mapping. The numbers on the top of the gray lines indicate the Z'_{St} masses in units of GeV.

Chapter 3

Experiment

3.1 The Large Hadron Collider (LHC)

The LHC, located at the European Organization for Nuclear Research (CERN), on the border of Switzerland and France, near Geneva, is a 27 km circumference synchrotron. Seven independent experiments operate on the LHC: CMS [36], ATLAS [37], ALICE [38], MoEDAL [39], TOTEM [40], LHCb [41] and LHCf [42]. The locations of those experiments as well as the LHC injection rings are shown in Figure 3.1.

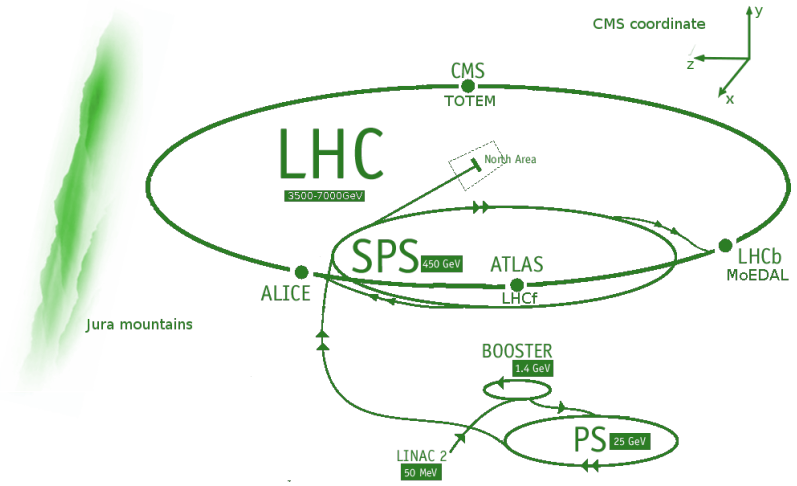

Figure 3.1: The LHC injector complex and the locations of the detectors[1].

[1]Modified from http://physics.stackexchange.com/questions/257/particle-colliders-why-do-they-need-an-accelerator-chain.

While running proton-proton collisions, the protons are accelerated by the following path:

$$\text{LINAC2} \xrightarrow{50\text{MeV}} \text{PS booster} \xrightarrow{1.4\text{GeV}} \text{PS} \xrightarrow{25\text{GeV}} \text{SPS} \xrightarrow{450\text{GeV}} \text{LHC} \xrightarrow{3.5\sim7\text{TeV}},$$

with the text above the arrows indicating the output beam energy. The protons are injected as bunches into the main ring every 25 to 50 ns in opposite circulating directions. As a result, two opposite direction bunches will cross each other inside the detectors and the protons inside the bunches will collide. Each such crossing is called a *bunch crossing*.

Up to now, the main proton-proton collision physics data taking periods are from March to October, 2011 and from April to December, 2012. In 2011, the LHC delivered proton beams with 7 TeV center of mass energy ($\sqrt{s}$). The instantaneous luminosity was around $10^{32} \sim 10^{33}\,\text{cm}^{-2}\text{s}^{-1}$. In 2012, $\sqrt{s}$ was updated to 8 TeV and the instantaneous luminosity was updated to $10^{33} \sim 10^{34}\,\text{cm}^{-2}\text{s}^{-1}$.

3.2 The Compact Muon Solenoid (CMS)

The CMS detector is a high-energy physics multi-purpose detector. It contains three major subdetector systems from the interaction point to outside – the trackers, including silicon pixels detectors at the center and strip tracking detectors around; the calorimeters, a $PbWO_4$ crystal electromagnetic calorimeter (ECAL) and a hadron calorimeter (HCAL) made of stainless steel, brass and plastic scintillators; and the muon systems, including aluminum drift tubes (DTs) in the barrel region and cathode strip chambers (CSCs) in the endcap region, complemented by resistive plate chambers (RPCs), as shown in the top panel of Figure 3.2. The tracker system and the calorimeters are surrounded by a superconducting solenoid, producing an approximately 4 T magnetic field, as shown in the bottom panel of Figure 3.2. The muon system is outside of the solenoid, experiencing less magnetic field [43].

3.2.1 Coordinate System and Conventions

CMS uses a right handed, Cartesian coordinate system, with the origin centered at the nominal collision point inside the experiment (the origin in Figure 3.2), the y-axis pointing vertically upward, and the x-axis pointing radially inward toward the center of the LHC. Thus the z-axis points along the beam direction toward the Jura mountains, as shown in Figure 3.1. Five barrel wheels, 0, ±1, and ±2 are installed in the central region of CMS. Each wheel has four stations labeled 1 to 4 from inner to outer. Four muon stations with yokes, labeled ME$\pm1 \sim \pm4$, are installed in the

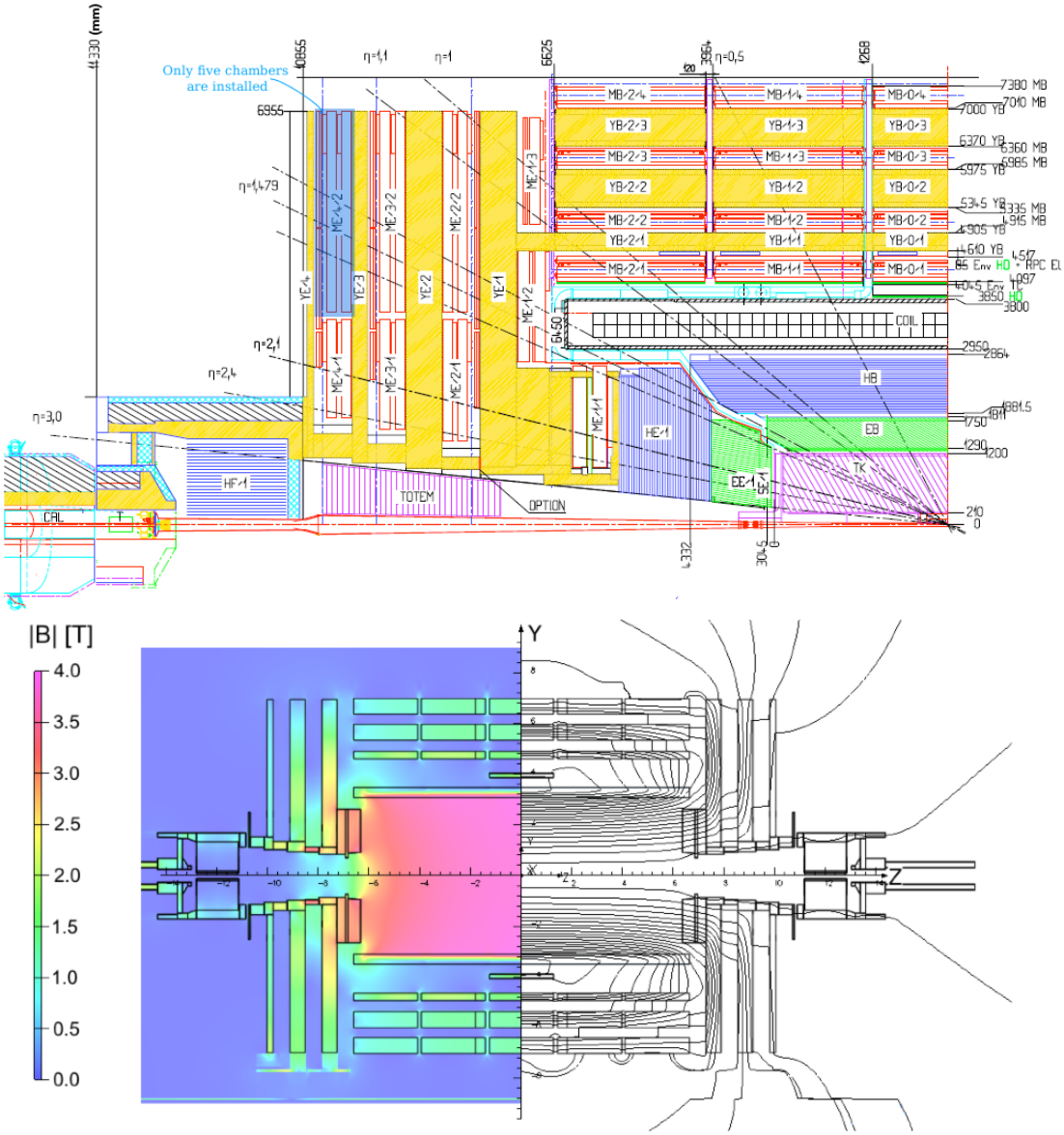

Figure 3.2: Top: One quarter longitudinal view of the CMS Experiment [1]. Acronyms: TK - tracker system; EB - barrel part of ECAL; EE - endcap part of ECAL; SE - silicon preshower detector; HB - barrel part of HCAL; HE - endcap part of HCAL; HO - barrel outer part of HCAL; HF - forward part of HCAL; MB - barrel region of muon system ; ME - endcap region of muon system; RPC - resistive plate chambers; YB - barrel part of iron yoke; YE - endcap part of iron yoke; η - pseudo-rapidity. Bottom: Simulated value of $|\vec{B}|$ (left) and field lines (right) projected on a longitudinal section of the CMS detector, for the underground model at a central magnetic flux density of 3.8 T. YE1 $\sim$ 3 are shown. Each field line represents a magnetic flux increment of 6 Wb [44].

endcap region. Endcap stations ± 1 have three rings. The other endcap stations have two rings.

The following conventions are defined:

- Radius: $r = \sqrt{x^2 + y^2}$;
- Azimuthal angle: $\phi = \tan^{-1}\left(\frac{x}{y}\right)$;
- Pseudorapidity: $\eta = -\ln\left(\frac{r}{2z}\right) = \frac{1}{2}\ln\left(\frac{|\vec{p}| + p_{\mathrm{L}}}{|\vec{p}| - p_{\mathrm{L}}}\right)$;
- Transverse impact parameter: the distance from the beam-spot (BS) to the trajectory of the track on the xy-plane, noted as d_{xy};
- d_z: the distance from the beam-spot (BS) to the trajectory of the track on the z direction;
- Solid angular distance in the (η, ϕ)-plane: $\Delta R = \sqrt{(\Delta\eta)^2 + (\Delta\phi)^2}$;
- Underlying events: Underlying events are events from the primary proton-proton collision but do not come from the primary hard scattering process (the process with highest total p_{T}). They have chromodynamics color connections with the primary hard scattering process;
- Pile-up events: Pile-up events are events from all proton-proton collisions except the primary proton-proton collision containing the primary hard scattering process. They happen at the same time as the primary collision.

3.2.2 Tracker System

The purpose of the tracker system is to determine the track of a particle. It is the most inner subdetector of CMS, and covers the region $|\eta| < 2.5$, $|z| < 280\,\mathrm{cm}$ and $r < 120\,\mathrm{cm}$, as shown in Figure 3.3.

The tracker system includes two types of silicon detectors, the pixel detectors and the strip detectors, which are introduced in the following sections.

Pixel Detector

The pixel detector is the innermost subdetector of CMS. Due to the extremely high particle fluxes at small distances (up to 6×10^{14} hadrons per cm^2 and about 7 cm from the interaction point), it is designed to have small element size ($150\,\mu\mathrm{m}^2$) and

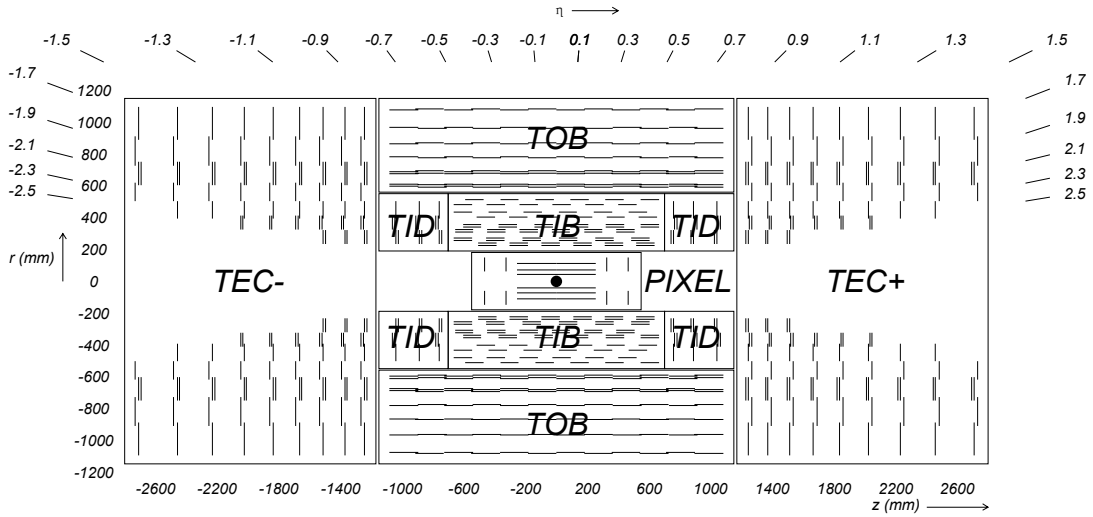

Figure 3.3: Schematic cross section through the CMS tracker. Each line represents a detector module. Double lines indicate back-to-back modules which deliver stereo hits (hit position in three coordinates). Acronyms: TIB - tracker inner barrel; TID - tracker inner disk; TOB - tracker outer barrel; TEC - tracker endcap. [45].

be able to measure the particle positions in three dimensions, which provides the highest space point resolution among all subdetectors.

The pixel detector has 3 barrel layers and 4 endcap disks, with 2 disks on each side[2].

The main elements of the pixel detector are doped silicon sensors, as shown in Figure 3.4. When a charged particle passes through the sensor, thousands or tens of thousands of electron-hole pairs are generated and pulled in opposite directions by an electric field. Only charged tracks could be detected by such sensors. The neutral particles, like photons and neutrons, do not leave any signal in the silicon sensors.

Silicon Strip Tracker

As the particle flux rate per unit area is reduced outside of the pixel detector region, silicon strip tracker (SST) detectors are installed. Instead of reading out information point by point, the SST readouts one and two coordinates. A single-sided module of the strip tracker sensor is shown in Figure 3.5. The working principle is quite similar to that of the pixel detector.

[2]It is planned to be upgraded to 4 barrel layers and 6 endcap disks, with 3 disks on each side before 2020.

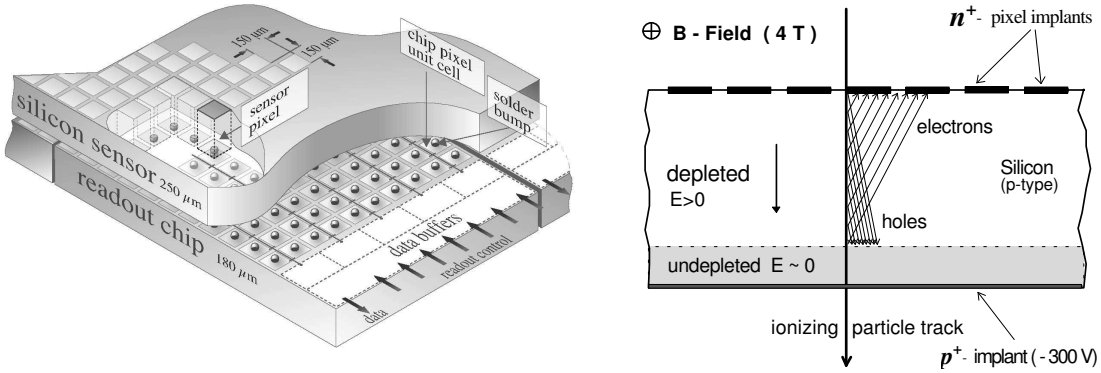

Figure 3.4: The pixel silicon sensor element and its working principle [46]. Left: Schematic view of a pixel detector element. Each sensor pixel is connected via a solder bump to a pixel unit cell on the readout chip, where the signal is amplified. The hit data are stored on the edge of the chip where they wait for trigger confirmation. Right: The working principle of the pixel silicon sensor. The picture shows the charge sharing induced by Lorentz drift.

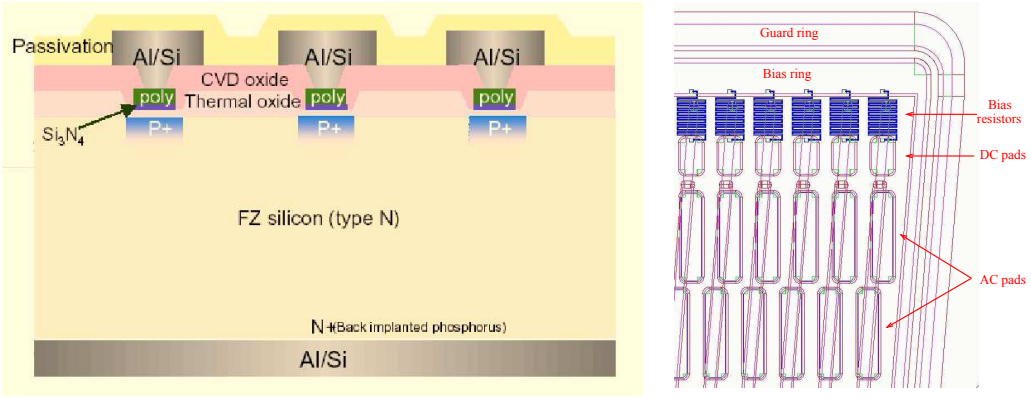

Figure 3.5: Left: Schematics of a section of a silicon strip detector sensor. Right: View of one edge of the active region in a detector at the outer endcap. [47]

	Shape	Pitch[3]	Coordinates
TIB Layer 1-2	rectangular	80 μm	r, ϕ, and z
TIB Layer 3-4	rectangular	120 μm	r and ϕ
TID Ring 1	wedge	80/112 μm, 0.019852°	r, ϕ, and z
TID Ring 2	wedge	113/143 μm, 0.019852°	r, ϕ, and z
TID Ring 3	wedge	123/158 μm, 0.01799°	ϕ, and z

Table 3.1: Tracker inner barrel sensors. The layers/rings are labeled from inner to outer. For wedge sensors, the first two pitch values in the table refer to the shorter and longer side respectively; the third pitch value is the angular pitch. [47]

The SST elements are installed in two multi-layer cylinders, the tracker inner and outer, which wrap around the central area of the CMS. Both single-sided and double-sided sensors are used. The double-sided modules are made of two independent single-sided detection units, mounted back to back, with the second one being rotated at 100 mrad with respect to the first [47]. This design allows the sensor to provide space information both perpendicular and parallel to the strip orientation [45].

Inner Tracker

The inner barrel of the SST consists of 4 layers equipped with differently designed rectangular sensors. The two innermost layers host double-sided modules, which provide r, ϕ, and z coordinates; the outer two layers host single-sided modules, which provide r and ϕ coordinates only.

Each end of the inner disk of the SST consists of three identical disks with three rings on each disk. The two innermost rings host back-to-back modules while the outer one hosts single-sided ones.

Detailed inner barrel sensor parameters are shown in Table 3.1.

Outer Tracker

The outter barrel (TOB) has six layers. The first two layers are instrumented with double-sided modules. The endcap of the tracker (TEC) has nine disks on both $\pm z$ sides of the detector. The innermost disk has 7 rings while the number of rings of the outermost disk is reduced to 4 rings. Labeled from inner to outer at the innermost disk, rings 1, 2, and 5 in TEC are equipped with double-sided modules. Table 3.2 gives an overview of the tracker outer sensors.

[3]Pitch is the distance between two strips centers.

	Shape	Pitch	Coordinates
TOB Layer 1-2	rectangular	183 μm	r, ϕ, and z
TOB Layer 3-4	rectangular	183 μm	r and ϕ
TOB Layer 5-6	rectangular	122 μm	r and ϕ
TEC Ring 1	same with TID Ring 1		
TEC Ring 2	same with TID Ring 2		
TEC Ring 3	same with TID Ring 3		
TEC Ring 4	wedge	113/139 μm, 0.012856°	ϕ and z
TEC Ring 5	two wedges 	126/156 μm, 0.011909°	r, ϕ, and z
TEC Ring 6		143/185 μm, 0.012874°	ϕ and z
TEC Ring 7		140/172 μm, 0.009°	ϕ and z

Table 3.2: Tracker outer barrel sensors. The layers/rings are labeled from inner to outer. For wedge sensors, the first two pitch values in the table refer to the shorter and longer side respectively; the third pitch value is the angular pitch. For TEC ring 5 ,6, and 7 the wedge sensors are assemblies of two small wedge sensors, as shown by the picture in cell. In those cases, the first two pitch values in the table refer to the shorter side of the bottom wedge and longer side of the upper wedge, respectively. [47]

Alignment

The alignment system uses infrared laser beams with a wavelength $\lambda = 1075\,\text{nm}$ to monitor the positions of selected detector modules of the strip tracker and of special alignment sensors in the muon system. The alignment information is provided to determine the tracker substructure locations at the level of 100 μm [45]. An overview of the laser alignment system is shown in Figure 3.6.

Besides the laser alignment system, three track-based alignment algorithms using collision, cosmic muon, beam gas, and minimum bias event data[4] are being developed. They are the extension to the global Millepede algorithm [48] that takes all correlations into account, the Kalman Filter [49] that takes the most important correlations into account, and the HIP [50] algorithm that only takes correlations of parameters within a silicon tracker module into account.

Performance

The simulated performance of the tracker system is shown in Figure 3.7. The resolution of the tracker system can be summarized in the central region, where $|\eta| < 1.6$,

[4]Minimum bias events are the collision events kept with minimal trigger requirements.

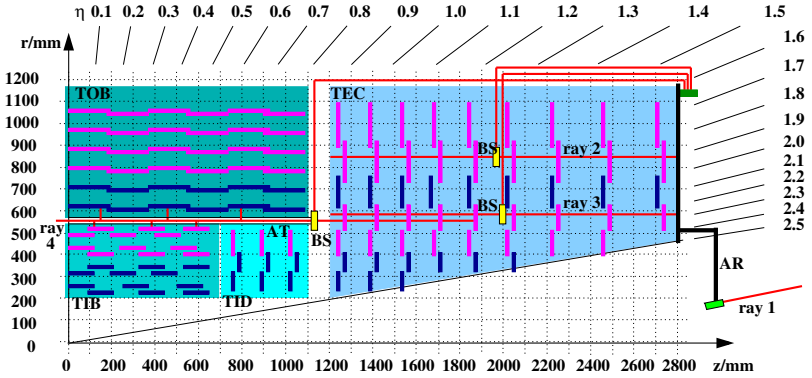

Figure 3.6: Overview of the tracker system with the laser alignment system [1]. Acronyms: BS - beam splitters; AT - alignment tubes; AR - alignment ring that is used to link with the muon system.

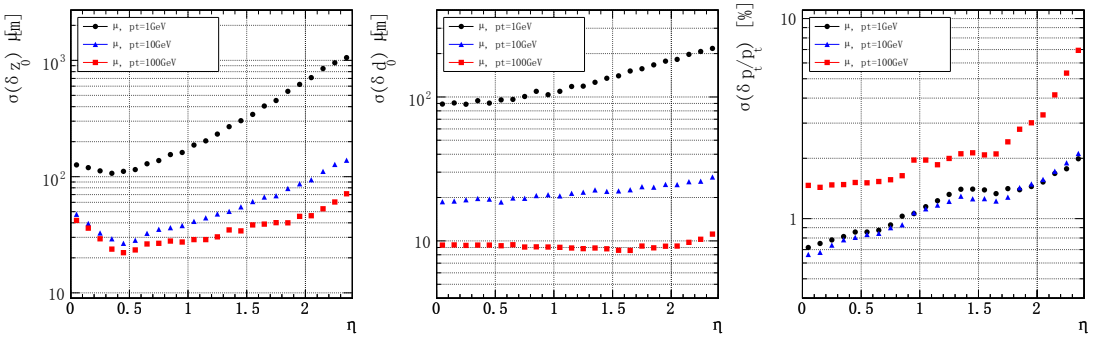

Figure 3.7: CMS Tracker stand-alone resolution of transverse momentum (left), transverse impact parameter (middle), and longitudinal impact parameter (right) as a function η, for muons whose $p_{\mathrm{T}} = 1$, 10 and 100 GeV . [45]

as

$$\frac{\delta p_{\mathrm{T}}}{p_{\mathrm{T}}} \approx \left(\frac{15}{\mathrm{TeV}} p_{\mathrm{T}} + 0.5\right) \%$$

and in the endcap region, where $1.6 < |\eta| < 2.5$, as

$$\frac{\delta p_{\mathrm{T}}}{p_{\mathrm{T}}} \approx \left(\frac{60}{\mathrm{TeV}} p_{\mathrm{T}} + 0.5\right) \%$$ [46].

The simulated global reconstruction efficiency of muons and pions is shown in Figure 3.8. The $|\eta| \approx 0$ efficiency drops because of the gaps between the ladders of the pixel detector at $|z| \approx 0$ [45]. The pion and hadron efficiency is generally lower because of interactions with the material in the tracker.

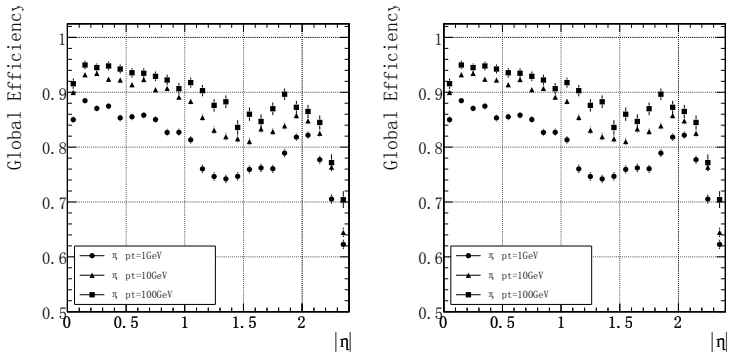

Figure 3.8: Global track reconstruction efficiency for muons (left panel) and pions (right panel) whose $p_{\mathrm{T}} = 1$, 10 and 100 GeV. [45]

3.2.3 Calorimeters

If a particle passes through the detector, the calorimeters measure the energy that the particle loses. CMS has two major types of calorimeters – the electromagnetic calorimeter (ECAL) that is mainly used to measure the photon and electron energy and the hadron calorimeter (HCAL) whose priority is to measure the hadron energy.

3.2.3.1 Electromagnetic Calorimeter (ECAL)

As radiation passes through the scintillating material, it excites the atoms and molecules making up the scintillating material causing light to be emitted [51]. The ECAL is designed to stop most photons and electrons entirely coming from the collision so that their total energy could be measured. In order to have a large stopping energy and be transparent to light, lead tungstate ($PbWO_4$) crystals are

chosen. The crystals emit blue-green scintillation light with a broad maximum at $420 \sim 430\,\text{nm}$ [52, 53]. The light is collected by avalanche photodiodes in the barrel region and vacuum phototriodes in the encaps.

Geometry

As shown in Figure 3.9, the geometrical crystals cover $|\eta| < 3.0$. Precision energy measurements, involving photons and electrons, are carried out to $|\eta| < 2.6$ with assistance from the tracker system and the preshower.

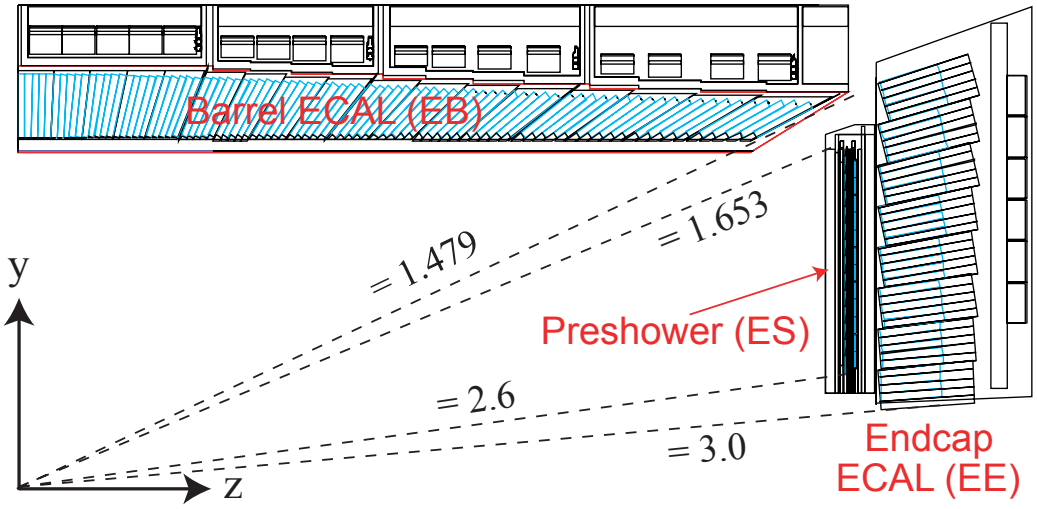

Figure 3.9: Transverse section through the ECAL, showing geometrical configuration [1].

Energy Resolution of Crystals

Because of the photon-electron cascade, the energy deposited by a photon/electron will be shared with several nearby crystals. Consequently, the crystals are clustered as 3×3 and 5×5 arrays for read-out. As an example, Figure 3.10 shows the energy resolution of the ECAL $PbWO_4$ 5×5 crystal arrays. For an energy range of about 20 GeV to 500 GeV, the energy resolution can be parameterized as

$$(\frac{\delta E}{E})^2 = (\frac{S}{\sqrt{E}})^2 + (\frac{N}{E})^2 + (0.30\%)^2,$$

where S is the stochastic term, N is the noise term. The parameter values are shown in Table 3.3.

	S (in $\sqrt{1\,\text{GeV}}$)	N (in 1 GeV)
5×5 barrel	$\sqrt{(2.1\%)^2 + (1.5\%)^2} = 2.58\%$	0.05
5×5 endcap at about 10^{33} cm^{-2}s^{-1}		$0.008 \times 5 = 0.04$
5×5 endcap at about 10^{34} cm^{-2}s^{-1}		$0.03 \times 5 = 0.15$
3×3 barrel	$\sqrt{(2.1\%)^2 + (2.0\%)^2} = 2.9\%$	0.05
3×3 endcap at about 10^{33} cm^{-2}s^{-1}		$0.08 \times 3 = 0.024$
3×3 endcap at about 10^{34} cm^{-2}s^{-1}		$0.03 \times 3 = 0.09$
3×3 with test beam	2.8%	0.12

Table 3.3: The ECAL energy resolution parameters in the barrel and endcap detectors. Except for the last row, expectation values were calculated according to [45]. The last row shows a typical resolution fit for a 3×3 array readout using the 2004 CERN test beam [54], which verifies the expectations.

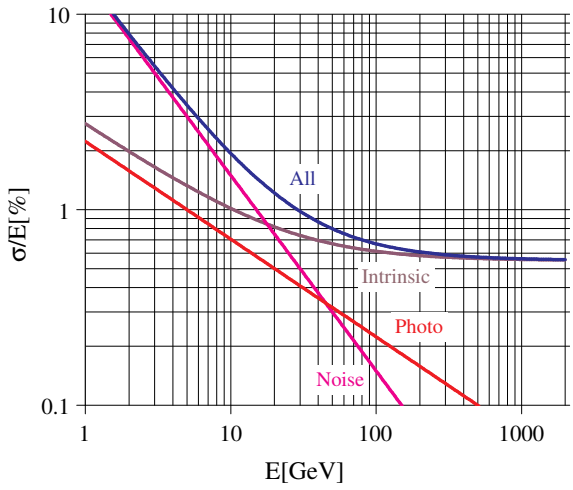

Figure 3.10: Different contributions to the energy resolution of the barrel $PbWO_4$ 5×5 crystal array ($\eta = 0$, luminosity at about $10^{32} \sim 10^{33}$ cm^{-2}s^{-1}) [55].

Endcap Preshower

The endcap preshower covers $1.65 < |\eta| < 2.61$. It is an array of silicon sensors that measure precisely the positions of incident high-energy electrons and photons. The energy measured in the silicon sensors is used to correct the energy measurement in the ECAL crystal. Its main function is to provide π^0/γ separation, as a π^0 decays into two close-by photons that appear to be one single photon. Figure 3.11 shows the structure of the preshower.

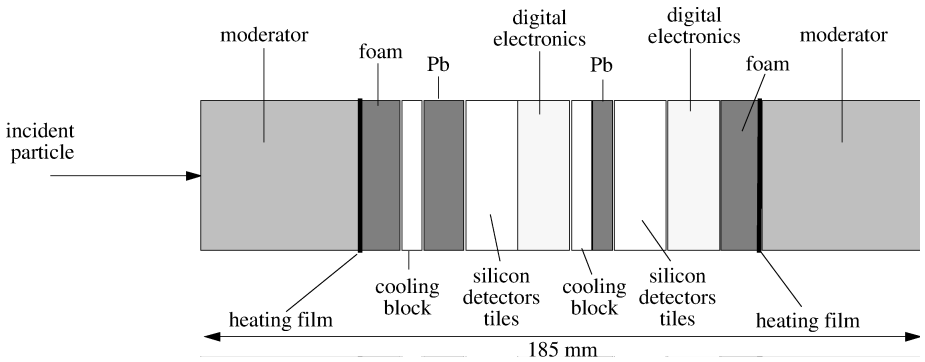

Figure 3.11: Schematic section through the endcap preshower [55].

The energy resolution of the preshower device can be approximately parameterized as [45, 56]

$$\frac{\delta E}{E} = \frac{5\%}{\sqrt{E}}.$$

3.2.3.2 Hadron Calorimeter (HCAL)

The hadron calorimeter is designed to stop most hadrons coming from the inner part of the detector. The components of the HCAL have been shown in Figure 3.2. The barrel (HB) extends to $|\eta| < 1.3$ and endcap (HE) covers the overlapping range $1.3 < |\eta| < 3.0$. Central shower containment in the region $|\eta| < 1.3$ is improved with an array of scintillators located outside the magnet in the outer barrel hadronic calorimeter (HO). Double layers of HO are located at barrel wheel 0 and single layers of HO are located at barrel wheels ± 1 and ± 2, as shown in green text in Figure 3.2. The forward calorimeters (HF) are located 11.2 m from the interaction point and extend the pseudorapidity coverage from 2.9 to 5.0. [45]

The HB, HE and HF are composed of active plastic scintillator tiles interspersed between the stainless steel and brass absorber plates. When a hadronic particle hits a plate of absorber, a cascade of particles results. Caused by this cascade of particles,

the active scintillation material emits blue-violet light. The blue-violet light is then shifted into the green light by the *wavelength-shifting fibres* located near the edge of the scintillator. Finally, clear optical cables carry the green light away to the readout electronics. Figure 3.12 shows a picture of 3 barrel HCAL towers and the scintillator of HCAL.

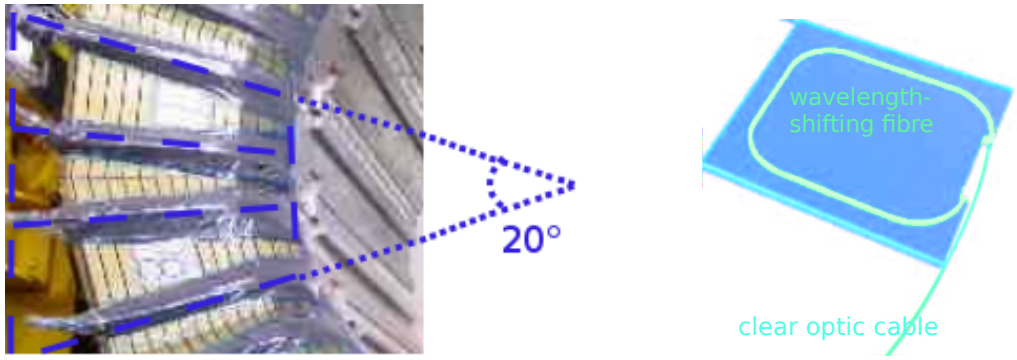

Figure 3.12: Left: 3 barrel HCAL towers (cut from [1]); Right: HCAL scintillator[5].

The HO is a single layer of plastic scintillator with wavelength-shifting fibres and optical cable readout. It is to ensure that no energy leaks from a hadronic shower deep inside HCAL.

The HF has three purposes [1, 45]:

1. The profile of the hadronic shower is described in both the longitudinal direction along the hadron's movement and the lateral direction perpendicular to the hadron's movement. The HF is intended to better measure the narrow lateral shower profile of the energetic forward jets;

2. With the installation of HF, the resulting increase in the hermeticity of the detector provides a more precise measurement of the missing transverse energy. The missing transverse energy is the imbalance of energy measured in the transverse (x, y)-plane. It is calculated by taking the minus sign of the summation of all observed transverse energies;

3. The HF is used to monitor the instantaneous luminosity by comparing the observed counts/energy with the predictions.

The performance of the HCAL was determined using a pion test beam. By use of the cluster-based weighting technique [57], the energy resolution of ECAL+HB can

[5]The picture is from `http://indico.cern.ch/event/46651/contribution/8/material/slides/1.ppt` with descriptive text added.

be parameterized as

$$\frac{\sigma}{E} = \frac{70\%\sqrt{\mathrm{GeV}}}{\sqrt{E}} + 8\%,$$

as shown in Figure 3.13.

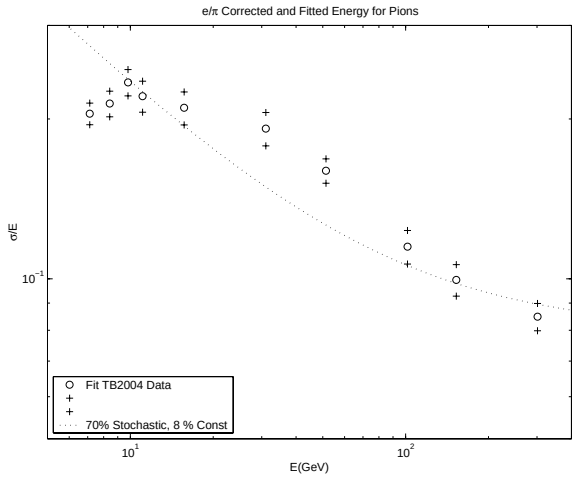

Figure 3.13: The fractional energy resolution as a function of ECAL+HB energy for pions [1]. The uncertainty band on the data points is indicated by the crosses.

3.2.4 The Muon System

Three types of gaseous detectors, together with the inner detectors mentioned above, are installed to identify muons and measure their momenta. Table 3.4 shows the configuration of those types of detectors and their working conditions. Figure 3.14 shows the locations of those detectors.

	$\lvert\eta\rvert < 1.2$	$0.9 < \lvert\eta\rvert < 2.4$	$\lvert\eta\rvert < 1.6^*$
neutron induced background	low	high	low and high
muon rate	low	high	low and high
residual magnetic field	$\approx 0.5 \sim 2.5$ T	$\approx 1.0 \sim 3.5$ T	$\approx 0.5 \sim 3.0$ T
type of detectors	drift tube (DT)	cathode strip chambers (CSC)	resistive plate chambers (RPC)

Table 3.4: The geometry configuration and the working conditions of the muon subdetectors. *The current installed RPCs measure up to $|\eta| = 1.6$. The plan is to install RPCs up to $|\eta| = 2.4$.

The following sub-sections introduce the detectors in detail.

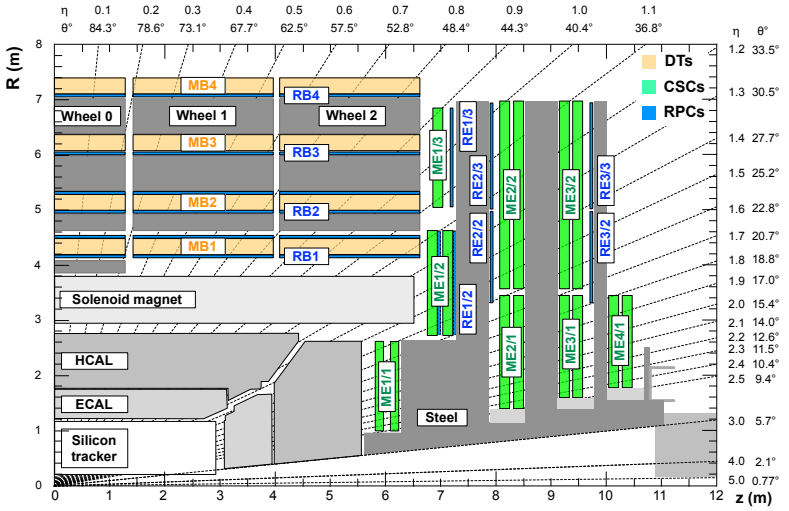

Figure 3.14: Layout of one quarter of the CMS muon system (from [58] with RPC locations corrected). Five CSC chambers that are on the ME+4 ring 2 are not shown in the figure.

3.2.4.1 Drift tube

The drift tube chambers are located in the places labeled MB in Figure 3.14. The distribution of DT chambers at barrel wheel 0 is shown in Figure 3.15. The other barrel wheel has the same arrangement of DT chambers. The layout of each chamber is shown in Figure 3.16. Figure 3.17 shows the structure of each cell of superlayers of each chamber.

Figure 3.17 also shows the DT working under the influence of a magnetic field of 0.45 T parallel to the anode wires: the cell is fulfilled with Ar (85%) CO_2(15%) and the high voltages are distributed as shown in the figure. When a charged particle goes though the cell, electron/ion pairs are created. Because of the existence of the electric field, the pairs resulting cascade and the electrons/ions then drift to the anode/cathode. Thus an electronic signal is made. In order not to mix the signals, the next signal has to be created after the charge from any earlier track has been collected. As a result, the drift tubes are used in the low background and low muon rate region.

The performance of the DT will be shown together with other muon detectors as the muon p_T resolution in Figure 3.24.

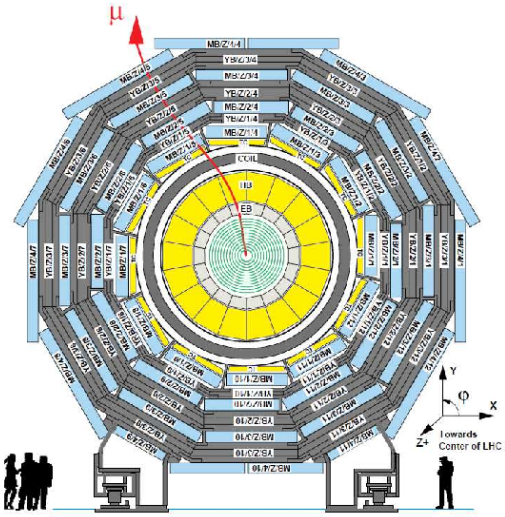

Figure 3.15: Transverse view of DT chambers at $z = 0$ [45]. The barrel muon detector elements are denoted as MB$Z/N/S$, where $Z = -2..+2$ is the barrel wheel number, $N = 1..4$ is the station number and $S = 1..12$ is the sector number. Similarly, the steel return yokes are denoted YB$Z/N/S$ ($N = 1..3$).

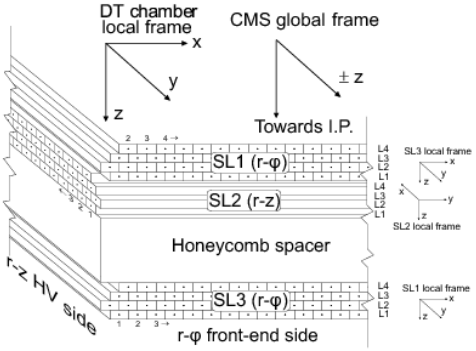

Figure 3.16: Schematic layout of a DT chamber. The distance between the innermost and outermost superlayer (SL) in the chamber is about 25 cm. The SL1 and SL3 superlayers measure the $r - \phi$ coordinate in the bending plane of CMS; the SL2 superlayer measures the z coordinate, along the direction parallel to the beam (CMS global frame $\pm z$). [59]

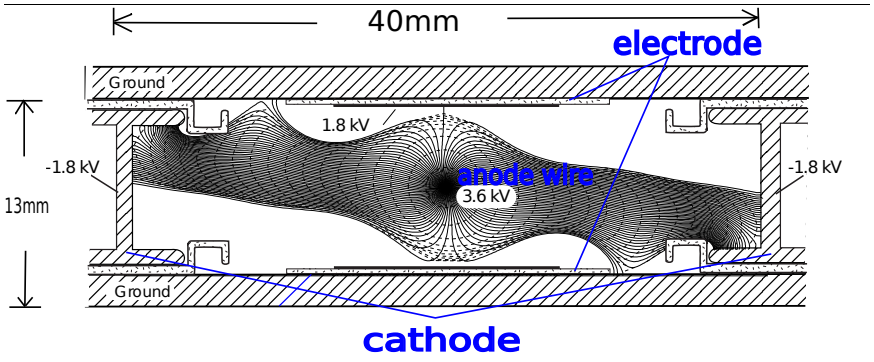

Figure 3.17: The drift cell of the CMS barrel muon detector under the influence of a magnetic field of 0.45 T parallel to the anode wires. The drift gas is Ar (85%) and CO_2(15%). The lines connecting the cathode with the anode are electron/ions drift lines and isochrones. The drift lines and isochrones are tilted by the Lorentz force $\vec{v} \times \vec{B}$. If the magnetic field is perpendicular to the anode wires, the drift lines and isochrones are un-tilted, resulting a shorter drift time. [60]

3.2.4.2 Cathode Strip Chamber

The cathode strip chambers are located in the places labeled ME in Figure 3.14. For ME±1 station, there are three rings. Each ring has 36 chambers. For the other ME stations, two rings are installed with 18 chambers on each ring. The chamber is a multiwire proportional chamber in which one cathode plane is segmented into strips running across wires. In each chamber, six layers of anode wires and cathode strips measuring the track of muons are assembled, as shown in the left panel of Figure 3.18. In a CSC layer, the anode wires are in the azimuthal direction and the cathode strips are in the radial direction [60]. For non-ME±1/1 chambers, the right panel of Figure 3.18 shows the arrangement of the strips and wires. For the ME±1/1 chambers, the wires are tilted by 25° corresponding to the bases of the trapezoid. Besides providing the azimuthal position, the anode wires provide precise timing measurement of a hit as well as a coarse measurement of its radial position.

Working Principle

While operating, the gaps among the layers are filled with Ar(30%), CO_2(50%), and CF_4(20%); the anode wires are fed with +2900V high voltage for ME±1/1 chambers and +3600V for the others. When a muon is passing by, an avalanche developed on a wire induces charges on the cathode plane, as shown in Figure 3.19. As one can see from Figure 3.19, close wire spacing allows for faster chamber response

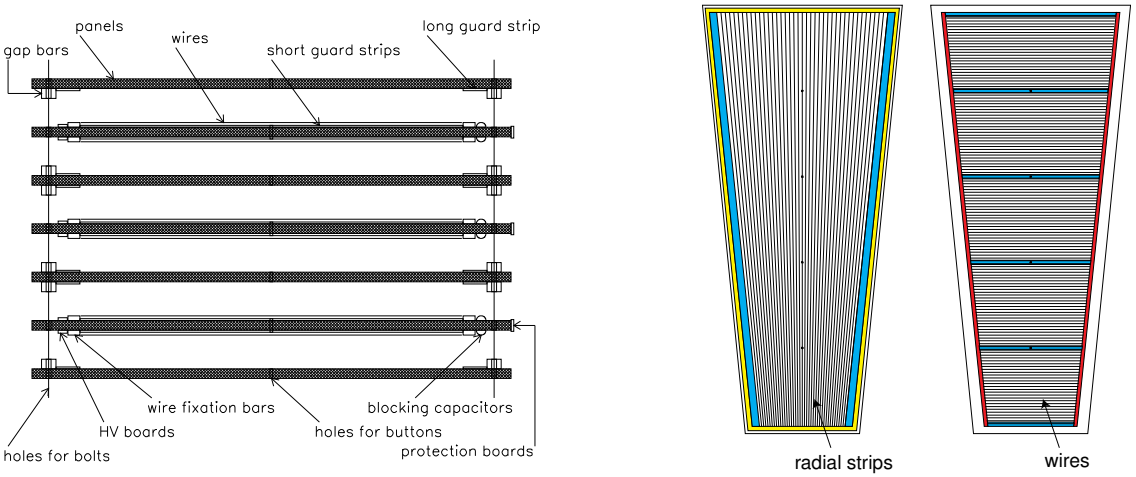

Figure 3.18: Left: Exploded view of a cathode strip chamber showing its main components and the way the chamber is assembled. Right: Face of a cathode panel (except ME±1/1) showing the arrangement of strips and face of an anode panel showing subdivision of wires into five independent HV segments. [60]

than the drift tubes. Thus the CSCs are used in relatively high background and high muon rate region.

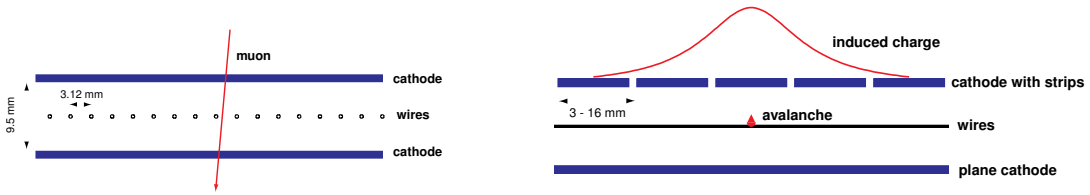

Figure 3.19: Principle of coordinate measurement with a cathode strip chamber: cross-section across wires (left) and across cathode strips (right). [60]

Electronics

The schematic of the electronics of the CSC system is shown in Figure 3.20. Four to five cathode front-end boards (CFEB), 12 to 42 anode front-end boards (AFEB), and one anode local charged track (ALCT) board are mounted directly on each CSC chambers.

When a muon passes a chamber, anode hit patterns are created by the ALCT board, combining all 6 layer signals in AFEBs. Similarly, cathode hit patterns (CLCT) are created by the trigger mother board (TMB), combining data from

CFEBs. The TMB located in the peripheral crates then finds the best match between the anode patterns and the cathode patterns. The matched two dimensional hit patterns are sent to the muon port card (MPC). Each MPC serves 9 chambers in three stations. For each bunch crossing, it finds out the three best 2D hit patterns and sends them as the local CSC trigger (shown in Figure 3.25) to the upstream level 1 trigger electronics. The level 1 trigger system will be described in Section 3.2.5.

The above mentioned procedure is part of the level 1 trigger system. The data used in high level data filtering[6] and offline reconstruction[7] are collected by the data acquisition motherboards (DMB) located in the peripheral crates. There is one DMB for each chamber. The data consist of ALCT and CLCT decisions, anode and cathod hits, and digitized strip signal waveforms. Upon a readout request sent from the global trigger system in CMS[8], the data collected by the DMB are passed to a detector-dependent unit (DDU) board, then to a data concentration card (DCC), and finally to the CMS computing farm [45].

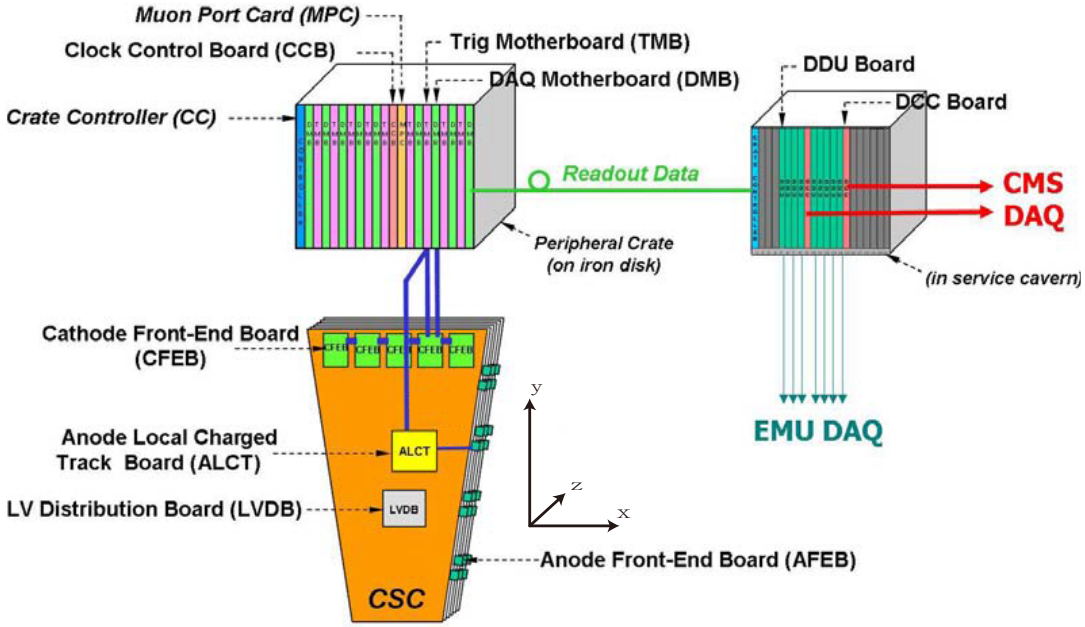

Figure 3.20: Schematic layout of the CSC trigger and read-out electronics [45]. Acronyms: DAQ - data acquisition system, DDU - detector-dependent unit board, DCC - data concentration card, EMU - endcap muon system.

[6]It will be introduced in Section 3.2.5.
[7]It will be described in Section 3.4.
[8]It is an L1A. The L1A will be mentioned in Section 3.2.5

3.2.4.3 Resistive Plate Chambers

The location of the resistive plate chambers is shown in Figure 3.14. Six layers of RPCs are installed in the barrel region: MB1 and MB2 DT chambers are sandwiched with two RPCs; MB3 and MB4 has one RPC with each DT chamber. In the endcap region, the RPCs are currently installed on ring 2 and 3.

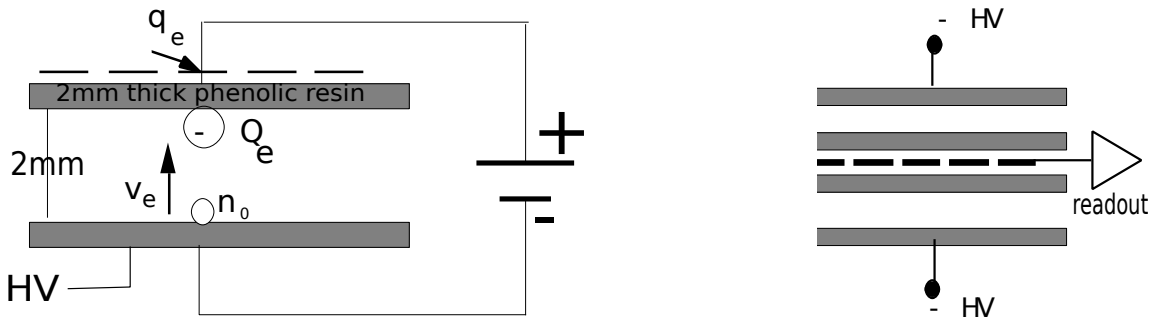

Figure 3.21: Left: Model of the charge formation in the RPC gap. Right: The double-gap RPC layout used in CMS. [60]

The RPCs are gaseous parallel-plate detectors. Two parallel plates made with phenolic resin (resistivity $\rho = 10^{10} \sim 10^{11}\Omega$·cm) are coated with conductive graphite paint to form the HV and ground electrodes. The gap is fulfilled with CF_3-CH_2F (tetrafluoroethane, 95%) and i-C_4H_{10} (isobutane, 5%). As shown in Figure 3.21 left, when an ionizing particle passes through the RPC, a cluster of n_0 electrons ignites the avalanche multiplication. An electronic charge Q_e is then developed inside the gap. The drift of such charge towards the graphite anode induces the "fast" charge q_e, which represents the useful signal of the RPC. Double-gap RPCs see the sum of the single gap signals, which is then able to be operated at lower high voltage with an effective detector efficiency [60]. As a result, CMS uses the double-gap RPCs, as shown in Figure 3.21 right.

Because of the small drift length/time and the thin shape compared with the DT and CSC, the RPCs are good in timing, have low cluster size, and are capable with different particle rates. Thus they are mainly used for triggering events with high efficiency under a wide range of neutron induced background and muon rate.

3.2.4.4 Alignment System

As mentioned in section 3.2.2, the CMS detector is equipped with a laser alignment system for tracker and muon systems. The overview of the system is shown in Figure 3.22. Each of the 250 DT chambers is monitored while one sixth of CSCs in the 4 endcap stations are directly monitored. Alignment sensors located in the

region between the muon barrel wheels and endcap disks allow the tracker and muon detectors to be aligned with respect to each other. [45]

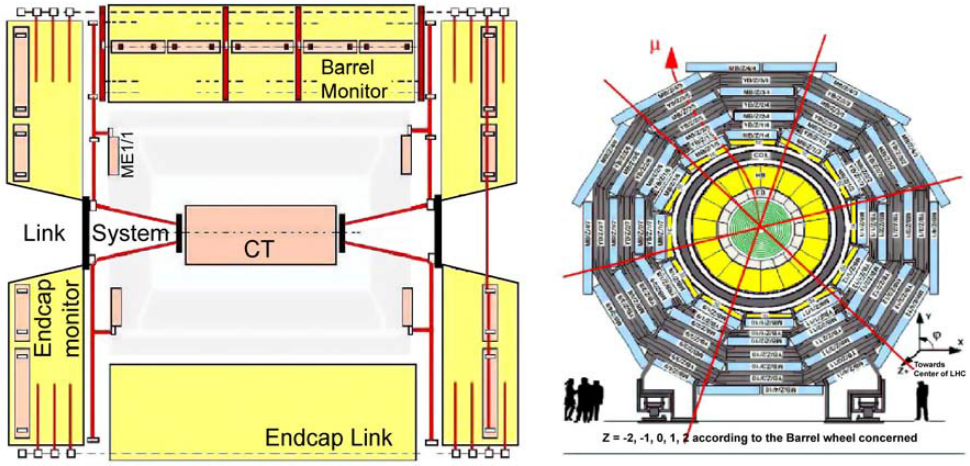

Figure 3.22: Schematic view of the muon alignment system. Left panel: longitudinal view of CMS. The continuous red lines and dotted black lines show different optical light paths. Right panel: transverse view of the barrel muon detector. The crossing red lines indicate the r-z alignment planes with 60° staggering in ϕ. [45] CT: central tracker.

3.2.4.5 Performance

Combining the DT and CSC signals, tracks named *stand-alone muons* are built by the Kalman filter algorithm [61]. The stand-alone muons are reconstructed using only hits from the muon system with a vertex constraint at the interaction point. If a muon leaves hits in only one DT/CSC station, the RPCs will help with the identification of the DT/CSC hits but the RPC hits will not be aggregated in the stand-alone muon trajectory. The simulated stand-alone muon reconstruction efficiency versus $|\eta|$ for selected p_{T} is shown in the left panel of Figure 3.23. The stand-alone muons are further matched with the tracks built in the tracker system, resulting in *global muons*. The efficiency of the global muons is shown in the right panel of Figure 3.23. The efficiency drops around $|\eta| = 0.25$ and $|\eta| = 0.8$ is because of the gaps between two DT wheels. The transition region between the DT and CSC systems results in a drop in efficiency around $|\eta| = 1.2$.

The simulated relative p_{T} resolution versus $|\eta|$ of the standalone muons and global muons is shown in Figure 3.24.

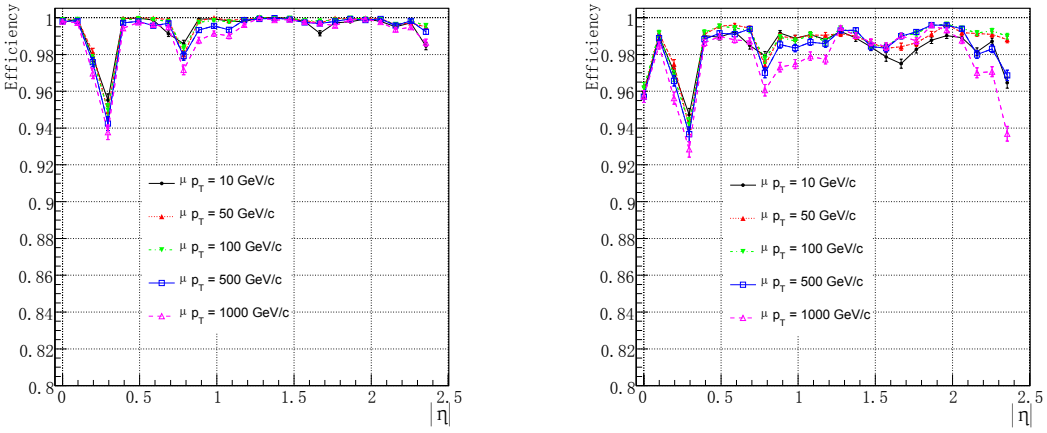

Figure 3.23: Muon reconstruction efficiency as a function of pseudorapidity for selected values of p_{T}. Left panel: standalone muon. Right panel: global muon. [45]

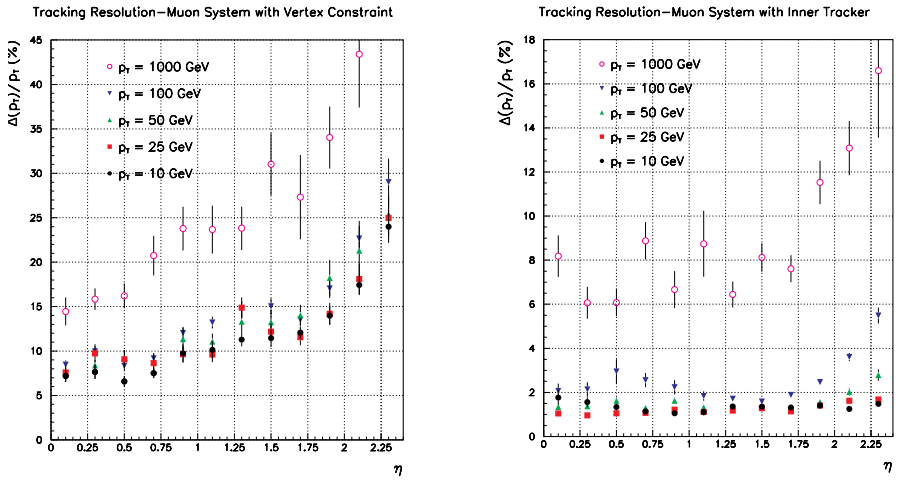

Figure 3.24: Momentum resolution of simulated muon tracks. Left panel: standalone muon. Right panel: global muon. [60]

3.2.5 Trigger and Data Acquisition System

Due to limitations from the electronics and the storage, not all of the interactions created in CMS could be recorded. The trigger system is designed to select the events containing interesting physics. Only the selected (triggered) events will be recorded. CMS contains two levels of triggers, the level-1 trigger system (L1) that is the initial filter and the high level trigger (HLT) that further reduces the rate of the events.

The organization of the level 1 trigger system is shown in Figure 3.25. The global trigger incorporates the decisions from the global L1 calorimeter trigger and the global L1 muon trigger. If the decision made by the global trigger is to trigger on a specific branch crossing event, an *L1 accept* (L1A) signal will be sent via the trigger timing and control system to all of the subdetector front-end and readout systems. Then all data (trigger primitive data) in the subdetector front-end buffers along with the global trigger objects are transmitted to a computer farm (high level trigger event filter) that reconstructs the events. The high level trigger (HLT) performs simpler and faster reconstruction of the physics objects and provides less accurate information than the offline reconstruction[9]. The events selected by the HLT will be recorded as RAW data and be further reconstructed offline. The offline reconstructed data are used in the physics analysis.

The complete data acquisition procedure is shown in Figure 3.26: at the LHC design bunching crossing frequency (40 MHz) and design luminosity (about $10^{34}\,\mathrm{cm}^{-2}\mathrm{s}^{-1}$), the level 1 trigger reduces the event rate to about 100 kHz. Further HLT selections reduce the event rate to about 100 Hz.

3.3 Luminosity Calculation

The luminosity is theoretically defined in Equation 2.14. In CMS, the luminosity is measured by taking the observed number of inelastic collisions and the expected total inelastic cross section into account. The observed number of inelastic collisions is recorded by the pixel detector using zero-bias trigger. The zero-bias trigger requires only the two bunches of particles cross at the CMS interaction point. The expected total inelastic cross section is measured by the Van der Meer scan technique [12]. More details about the CMS luminosity calculation are given in [12].

[9] A view of the offline reconstruction is introduced in section 3.4.

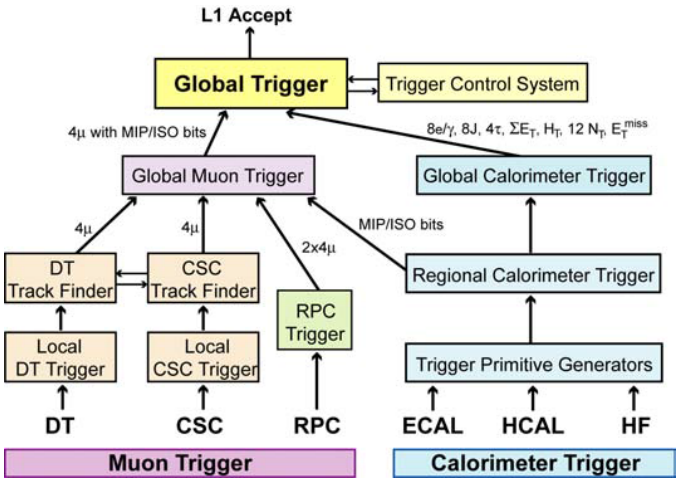

Figure 3.25: Overview of CMS Level 1 Trigger [45]. MIP: minimum-ionizing particle; ISO: isolation bits.

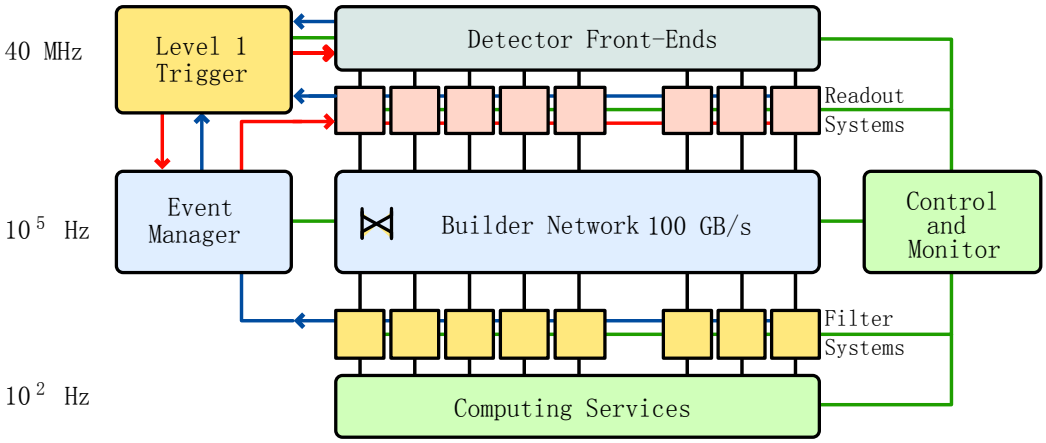

Figure 3.26: Architecture of the CMS DAQ system at the design luminosity of $10^{34}\,\mathrm{cm}^{-2}\mathrm{s}^{-1}$. [45] The blue arrows and connections indicate the data upload path for the level 1 trigger. The red arrows and connections indicate the L1A command transmittal path. The black connections indicate the data upload path for physics analysis (from the Detector Front-Ends). The green lines indicate the control and monitoring connections. The text on left of the picture shows the event rate at each level.

3.4 Reconstruction

A sketch of the particle offline reconstruction is shown in Figure 3.27. Table 3.5 summarizes the major information and algorithm used for identifying each kind of physics object.

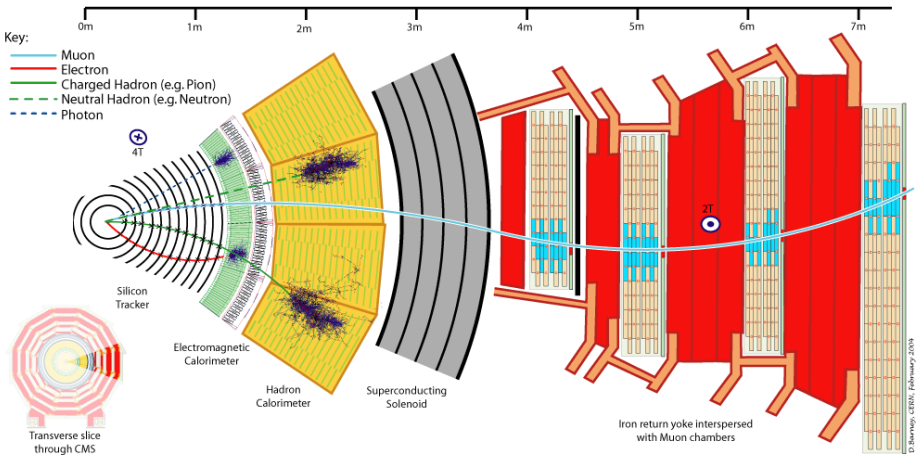

Figure 3.27: A slice view of the CMS detector that illustrates particle tracks and energy deposits [2].

	Tracker	ECAL	Preshower	HCAL	DT+CSC	Major algorithm
Muon	√	√		√	√	the Kalman filter (KF) [61]
Electron	√	√				the Gaussian Sum Filter (GSF) [62], a nonlinear generalization of the KF
Photon		√	√			superclustering [1]
Jet*	√	√	√	√	√	anti-k_{T} clustering[63]

Table 3.5: An overview of subdetector signals and algorithms used in offline reconstruction. *A jet originated from a quark/gluon may contain photons, leptons and hadrons.

Specifically and briefly [1], for each major detector and physics object, the algorithms used in building the physics objects are listed as follows:

- Tracker track:

    1. Reconstructing hits, clustering the signals from the pixel and silicon strip detectors and then estimating positions with uncertainty;

2. Finding seed, using two or three hits in the tracker system plus beam constraint as the seed;
3. Building trajectory, based on a combinatorial Kalman filter method;
4. Cleaning, if one seed results in more than one track candidates or one track candidate comes from different seeds, only one of them will be kept based on the number of shared hits, the number of hits, and the track fitting χ^2.
5. Smoothing, after determining the track hits, a fit (smoothing) of all selected hits by the Kalman filter.

- Primary interaction vertex (PV):
  1. Pre-selecting tracks, based on their distance of closest approach to the beam and their p_{T};
  2. Forming clusters of tracks, based on the z-coordinate of their point of closest approach with respect to the beam line;
  3. Fitting, based on *Adaptive Vertex Fit* [64, 65] of a primary-vertex candidate for each of these clusters, discarding tracks incompatible with the candidate vertex;
  4. Cleaning, removing the poor fits and vertices incompatible with the beam line.
- Secondary vertex in jets:
  1. Applying *Trimmed Kalman Vertex Finder* [66] to find out the secondary vertex candidate;
  2. Looking for additional tracks that are close to the flight-line of a possible b-hadron;
  3. Reconstructing the vertex with those additional tracks.
- Muon: To be described in detail in the next section;
- Electron:
  1. Superclustering 3×3 or 5×5 ECAL crystals energy deposit;
  2. Matching geometry and energy-momentum loosely between the reconstructed tracker tracks and the corresponding supercluster. Taking the first two track hits as the seed;

3. Building tracks by GSF [62] algorithm;
4. Correcting electron energy scale: This is because different ECAL crystals have different response to the same energy deposit;
5. Matching both geometry and energy-momentum of the GSF reconstructed tracks and the superclusters;
6. Checking energy leakage in HCAL;
7. Combining the energy measured in ECAL and momentum measured in the tracker system.

- Photon that reaches ECAL:

1. Superclustering 5×5 ECAL crystals energy deposit;
2. Rejecting π^0 based on the position-sensitive preshower detector.

- Converted photon that originates from the primary interaction vertex and then converts to most likely electron pairs in the tracker material:

1. Building seed, based on energy clusters including superclusters and single crystals;
2. Searching for compatible hits in the outer most 2 tracker layers, assuming that the hits lie on a straight line in the (r,z) plane from the primary interaction vertex to the cluster;
3. Extrapolating the trajectory inward into the tracker system to find compatible hits and the conversion vertex;
4. Cleaning and smoothing the track (the final track refit);
5. Rejecting π^0 based on the position-sensitive preshower detector.

- Jets: Based on the performance of different jet clustering algorithms, the anti k_{T} with radius parameter $R = 0.5$ [63] using the particle-flow objects [67] as input is used in most physics analyses. This method is insensitive to underlying events and pile-up events.

For muons, electrons and photons, the isolation is studied depending on the comparison of the total energy deposited in a cone around the particle with a predefined threshold.

3.5 Muon Reconstruction

3.5.1 Global Muon

There are two major steps to build a global muon track. The first step is to match two seeds, the stand-alone muon tracks introduced in the last chapter and the tracker tracks. The second step is to apply a global refit of the hits from the tracker and the muon system.

In the first step, both stand-alone muon tracks and tracker tracks are extrapolated to a common surface. On the common surface, a comparison of the track Kalman filter parameters [68] is made, involving the tracks' charge, position and momentum information (from the CMS internal note AN-2008-097) . Because those variables are stable on the innermost muon hit surface, that surface is chosen as the common surface.

In the second step, all of the hits from the tracker system are included. To reduce the affect from muon Bremsstrahlung (shower) and contaminated muon chambers, several refit algorithms are performed as following.

- Picky: Tracker hits with the muon hits selected by tight cuts for hit compatibility with the trajectory (picky muon reconstructor);
- Tracker-only: Tracker hits only;
- TPFMS: Tracker hits with the first muon station hits.

The final selection among those algorithms is made by comparing the tail probability of the χ^2 of the fit. By use of the selected hits, a global fit for those hits is applied, which results in the trajectory of the global muon.

In the following analysis, all muon parameters used are the parameters of the global muons reconstructed by this algorithm.

3.5.2 Tracker Muon

The tracker muon algorithm starts from reconstructed tracker tracks and then searches for compatible segments in the DT/CSC detectors. The ratio of the calorimeter energy deposit to the total energy of the track is used for muon identification. The momentum vector of a tracker muon is the same as that of the tracker track. The tracker muon helps in solving ambiguities of the global muon algorithm: Few reconstructed global muons cannot pass the tracker muon selection, which are considered as fake muons.

3.6 CSC Primitive Efficiency Measurement

The CSC primitive efficiency measurement is carried out to verify the performance of the CSC detector. We developed a method to achieve this goal by use of the proton-proton collision data.

The measurement is based on the *tag-and-probe* method using the Standard Model Z or the J/Ψ invariant mass region. The tag-and-probe is a standard method to measure the efficiency of real muons. It can be described as: There are N pairs of tracks. For each pair, the invariant mass of the two tracks are inside a resonance peak, such as the Z or the J/Ψ invariant mass region. We know that one of the two tracks is a real muon (tag). The other track (probe) may be a muon. We want to know how many probing tracks that are real muons pass the "efficient" selections.

The measurement can be approached by the following steps:

1. Make a dimuon invariant mass histogram using all of N pairs of tracks;
2. Fit the histogram by expected signal and background probability distribution functions (pdf);
3. Integrate the fitted background pdf to get the number of background events, noted as N_{bkg};
4. Obtain the pairs of tracks in which the probing track passes the "efficient" selections. The number of such pairs is N_P;
5. Repeat step 1 to step 3 using the N_P pairs obtained in the step 4. The number of background, N_P, is thus obtained as $N_{P\text{bkg}}$;
6. Calculate the efficiency of the real muons that pass the "efficient" selections:

$$\frac{N_P - N_{P\text{bkg}}}{N - N_{\text{bkg}}},$$

   where the denominator is the number of real muons from the resonance decays; the numerator is the number of real muons that pass the "efficient" selections.

The inefficiency of observing the probing muons can either because it does not leave any signal in the CSC detector or because such muon is scattered and does not pass the CSC detector as expected. Thus the efficiency obtained by the above mentioned steps is the CSC detector efficiency times the efficiency that the muon is not scattered.

In this section, the proton-proton collision data taken from Aug 30th, 2012 to Sep 06th, 2012 by CMS are used as an example of this method. The Drell-Yan and J/Ψ

simulations, with the pileup distribution reweighted to that of the corresponding data taking period, are used for the systematic uncertainty study. Five ME+4/2 chambers are not included in this example measurement.

3.6.1 Track Pair Selection

As long as the event is triggered by any single muon trigger and it is neither a pile-up nor a underlying event, the tracks in the events can be used in this method.

To get a real muon as the tag, a track is required to pass a tight selection:

- The track is reconstructed as a tracker muon[10];
- track $p_T > 5\,\text{GeV}$;
- track d_{xy} with beam spot $< 2\,\text{cm}$ and d_z with beam spot $< 24\,\text{cm}$;
- normalized track fit $\chi^2 < 4$;
- number of strip tracker hits$\geqslant 8$;
- number of matched segments in muon system$\geqslant 3$;
- $\Delta R < 0.01$ to any single muon trigger objects. A trigger object is a online reconstructed physics object that triggers the L1A.

In order to have a reliable extrapolation, the quality of the probing track reconstruction must be good enough. The quality requirements of the probing tracks are

- track momentum $p > 3\,\text{GeV}$;
- track d_{xy} with beam spot $< 2\,\text{cm}$ and d_z with beam spot $< 24\,\text{cm}$;
- normalized track fit $\chi^2 < 4$;
- number of strip tracker hits$\geqslant 8$;
- number of strip tracker and pixel tracker hits$\geqslant 10$;
- track $|\eta| < 2.4$ and its uncertainty $\Delta\eta < 0.003$;
- track ϕ uncertainty $\Delta\phi < 0.003$;

[10]Requiring a reconstructed global muon still works and results in little difference.

- track p_{T} relative uncertainty $\Delta p_T/p_T < 0.05$.

In addition, the probability of the probing track coming from the same resonance as the tagged muon should be high enough to increase the signal to background ratio. The additional requirements of the probing tracks are

- It is from the same primary vertex with the tagged muon;
- Its charge is different with the tagged muon;
- The invariant mass with the tagged muon $\in (2.5, 3.6)\,\mathrm{GeV}$ (J/Ψ pole) or $\in (75, +\infty)\,\mathrm{GeV}$ (Z pole and high mass off-shell Z/γ).

Upon the above selections, the probing track is extrapolated to the CSC chambers by the GEANT4 [69, 70] package in the CMS software. The GEANT4 is a package to predict the unknown path of a given track using Kalman filter [61] according to the detector material. Because the tagged muon may have associated CSC signals, any track close to the tagged muon could be matched with those CSC signals and considered as an efficient measurement. To avoid such a bias, the probing track should be away from the tagged muon. Thus, we require that at the primary vertex, at the extrapolated position on the ME$\pm$1 stations, and at the extrapolated position on the probing CSC chamber, the track ΔR with the tagged muon is > 0.2.

3.6.2 Definitions of Good Measurements

In this section, the extrapolated probing track is used to check whether a CSC chamber is working properly. The chambers known to be dead entirely are excluded from this measurement but the known partially working chambers are included in this measurement.

To be included in the denominator of the efficiency calculation, the extrapolated probing track has to pass through the active region of a CSC chamber. As shown in the right panel of Figure 3.18, the wire groups are divided into several independent HV segments. The gaps between those HV segments have no electronics. As a result, on the investigating CSC chamber, the extrapolated track position (point P in Figure 3.28) has to be:

- 5 cm and $3\sigma_{\mathrm{ex.trk.}}$ away from the chamber edge;
- 1 cm and $3\sigma_{\mathrm{ex.trk.}}$ away from the HV gap,

where $\sigma_{\mathrm{ex.trk.}}$ is the uncertainty of the position. Figure 3.28 illustrates those requirements.

Figure 3.28: Sketch of the track extrapolation on the CSC chamber. The two dotted lines are the required distances from the extrapolated track position to the chamber edge and HV gap.

As introduced in Section 3.2.4.2, the CSC provides two types of data: one is for the level 1 trigger; the other is for the high level trigger and offline reconstruction. The efficiency measurement of both types of data are performed.

A good local CSC trigger data is defined as: as long as an intercept of the triggered anode wire group and the strip is found in the same chamber with the point P in Figure 3.28, the chamber is considered as working properly. The efficiency calculated is the *CSC primitive LCT efficiency*.

Combing the anode wire group and strip signals from the six layers of the CSC chamber, segments of CSC hits are reconstructed offline. Those segments of CSC hits are used to build the stand-alone muons. A good CSC HLT and offline data in this measurement requires that the segment built in the chamber has to be less than 40 cm away from the point P. The efficiency calculated is the *CSC reconstructed segment efficiency*.

3.6.3 Systematic Uncertainties

The systematic uncertainties coming from the modeling of the probability distribution function (pdf) of the resonance signal and its background are studied by changing the models of fit in tag and probe method. The default pdf of the signal for both the SM Z and the J/Ψ is the Voigtian distribution. By changing the pdf to the Gaussian distribution, the signal modeling uncertainty of the efficiency is just the difference between the Voigtian modeling and the Gaussian modeling. Similar effort is made for the background: the default pdf of the background of the SM Z is an exponential function. The uncertainty is found by changing it to a quadratic polynomial function; The default pdf of the background of the J/Ψ is a linear func-

tion. The uncertainty is found by changing it to a quadratic polynomial function as well.

Another systematic uncertainty comes from the difference between the true muon efficiency and the tag and probe muon efficiency. This is studied with the simulation. In the simulation, both reconstructed tagged and probing tracks are matched to the simulated track by looking at how many reconstructed tracker hits associated with the reconstructed track match with the simulated tracker hits associated with the simulated track. Then we find whether the simulated track is a muon from a SM Z or a J/Ψ. If both simulated tracks are from a SM Z or a J/Ψ, the probing track is taken into the efficiency measurement otherwise the pair of tracks is not considered The difference between this Monte-Carlo truth efficiency and the efficiency obtained from the tag and probe method using the same simulation data is as uncertainty because our initial goal is to measure the efficiency of real muons.

Using the SM Z pole, the calculated systematic uncertainties of the LCT efficiency and the segment efficiency for CSC stations are listed in Table 3.6 and Table 3.7. In general, the total systematic uncertainty is around 1% or less, which shows this method is convincible. The systematic uncertainties for CSC chambers are listed in Figure 3.29 and Figure 3.30. Because the data are split into more than 400 chambers, the uncertainty of the calculation of the systematic uncertainties is larger. The systematic uncertainty runs from 1% to 5%, which is still good for monitoring the performance of the CSC detector because a electronic failure, e.g. a broken CFEB, always causes 20% inefficiency of a chamber.

Using the J/Ψ pole, the calculated systematic uncertainties of the LCT efficiency and the segment efficiency for CSC stations are listed in Table 3.8 and Table 3.9. In general, the total systematic uncertainty is about 1% to 2%, which provides a reliable measurement especially for low p_{T} muons. There are not enough data to calculate the efficiency for each individual CSC chamber using the J/Ψ pole.

station	ME11	ME12+13	ME2	ME3	ME4
MC truth (%)	0.171	0.059	0.087	0.009	0.003
Background modeling (%)	0.883	0.058	0.420	0.275	0.065
Signal modeling (%)	0.095	0.021	0.058	0.057	0.034
Total Sys(%)	0.90	0.085	0.43	0.28	0.07

Table 3.6: The systematic uncertainties of the CSC primitive LCT efficiency using the SM Z pole for CSC stations. The components of the uncertainties are combined in quadrature.

station	ME11	ME12+13	ME2	ME3	ME4
MC truth (%)	0.138	0.004	0.068	0.008	0.065
Background modeling (%)	0.874	0.020	0.406	0.258	0.052
Signal modeling (%)	0.099	0.029	0.062	0.047	0.033
Total Sys(%)	0.89	0.04	0.41	0.26	0.09

Table 3.7: The systematic uncertainties of the CSC reconstructed segment efficiency using the SM Z pole for CSC stations. The components of the uncertainties are combined in quadrature.

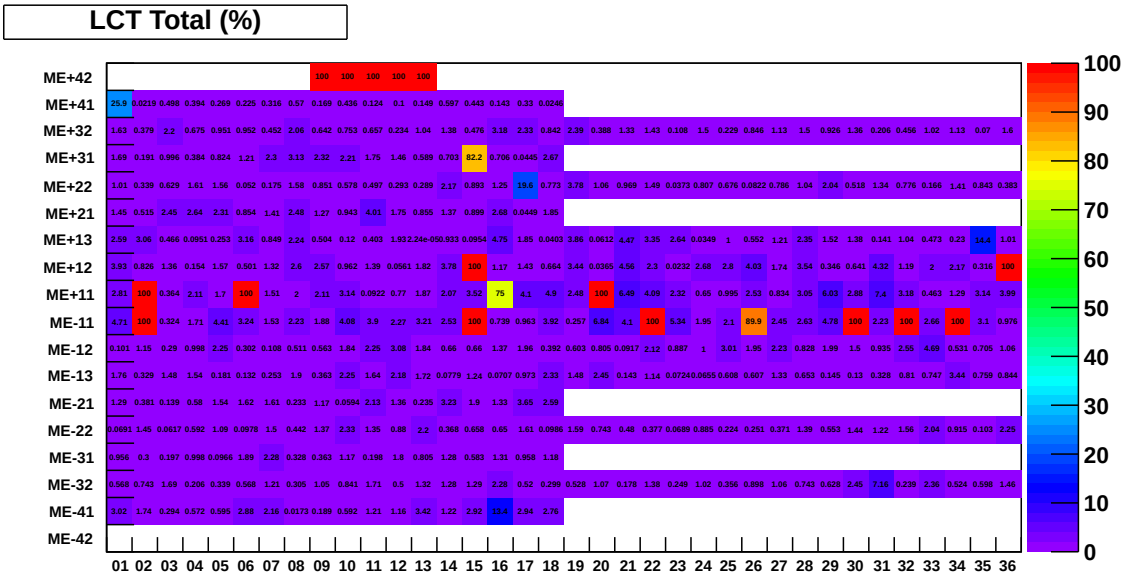

Figure 3.29: The total systematic uncertainties of the CSC primitive LCT efficiency using the SM Z pole for CSC chambers. The chambers with 100% uncertainty are dead or were not considered chambers.

station	ME11	ME12+13	ME2	ME3	ME4
MC Truth (%)	0.228	0.424	0.144	0.808	0.003
Background modeling (%)	1.303	0.722	0.034	0.926	0.061
Signal modeling (%)	0.050	0.039	0.000	0.198	0.061
Total Sys (%)	1.32	0.84	0.14	1.24	0.09

Table 3.8: The systematic uncertainties of the CSC primitive LCT efficiency using the J/Ψ pole for CSC stations. The components of the uncertainties are combined in quadrature.

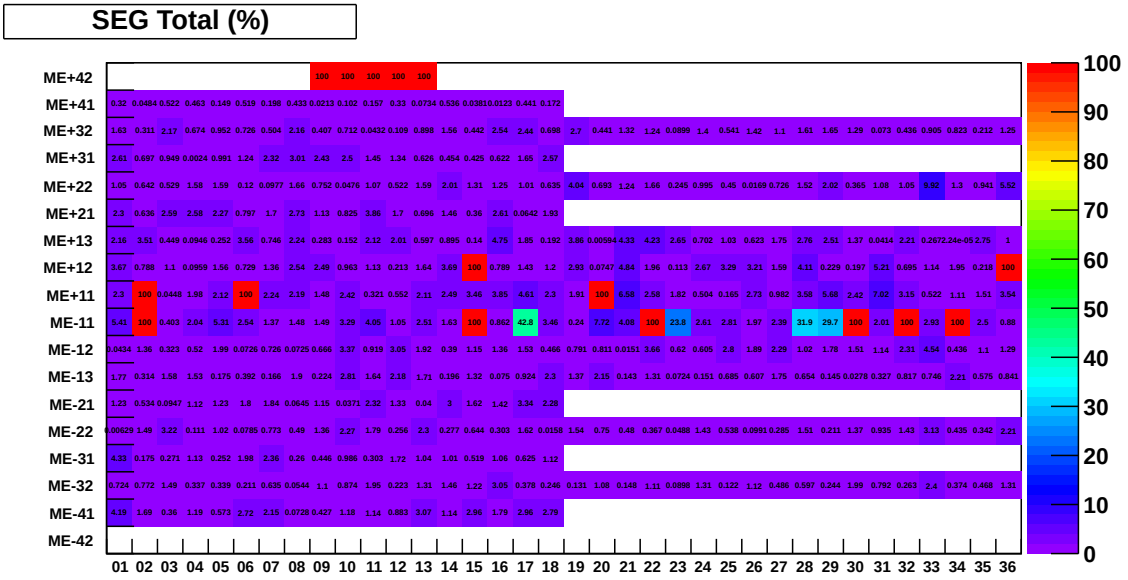

Figure 3.30: The total systematic uncertainties of the CSC reconstructed segment efficiency using the SM Z pole for CSC chambers. The chambers with 100% uncertainty are dead or were not considered chambers.

station	ME11	ME12+13	ME2	ME3	ME4
MC Truth (%)	0.374	1.315	0.171	0.740	0.290
Background modeling (%)	1.235	0.854	0.959	0.539	0.357
Signal modeling (%)	0.098	0.056	0.000	0.223	0.039
Total Sys (%)	1.30	1.57	0.97	0.94	0.46

Table 3.9: The systematic uncertainties of the CSC reconstructed segment efficiency using the J/Ψ pole for CSC stations. The components of the uncertainties are combined in quadrature.

3.6.4 Example Results

Using the SM Z pole, the LCT efficiency and the segment efficiency for CSC stations are shown in Figure 3.31 and Figure 3.32. Comparing the data with MC, the ME11 efficiency drops because the ME±1/1 stations have a higher rate of partially working chambers than the other stations. The dead chambers will be excluded in simulations. However, those partially working chambers are considered as fully working in simulations. In detail, using only data, the LCT efficiency and the segment efficiency for CSC chambers are shown in Figure 3.33 and Figure 3.34. If the chamber efficiency is less than 95%, it always means that some boards on the chambers have not been working or partially working during the data taking period. The list of known dead boards confirms this result with only few exceptions.

Using the J/Ψ pole and as a supplementary for low p_{T} muons, the LCT efficiency and the segment efficiency for CSC stations are shown in Figure 3.35 and Figure 3.36.

As a result, this CSC primitive efficiency measurement algorithm provides a reliable data monitoring and rechecking method. It reflects the performance of each CSC chamber in reality.

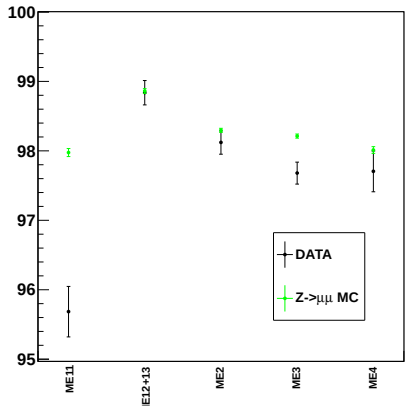

stations	efficiency±Systematic±Statistic
ME11	$95.69 \pm 1.01 \pm 0.36$
ME12+13	$98.84 \pm 0.09 \pm 0.18$
ME2	$98.12 \pm 0.46 \pm 0.17$
ME3	$97.68 \pm 0.28 \pm 0.16$
ME4	$97.71 \pm 0.13 \pm 0.29$

Figure 3.31: The CSC primitive LCT efficiency using the SM Z pole for CSC stations. Left Panel: The efficiency comparing data with the simulation, including statistic uncertainties only. Right Panel (Table): The efficiency of the data in numbers.

3.7 Identification of b-quark jets

B-quark jets arise from bottom-quark hadronization (b jets). The balance of the efficiency and the purity of b-quark jets crucially affects all related physics analysis channels. However, the analysis of this thesis does not use any b-quark jet. I will

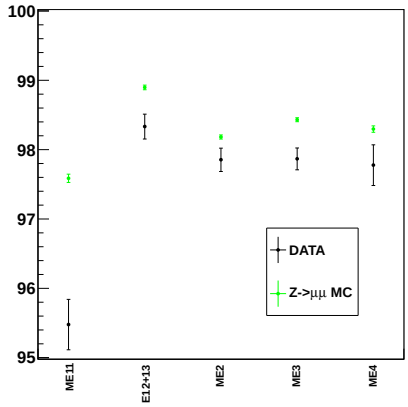

stations	efficiency±Systematic±Statistic
ME11	$95.48 \pm 0.89 \pm 0.36$
ME12+13	$98.33 \pm 0.04 \pm 0.18$
ME2	$97.86 \pm 0.41 \pm 0.17$
ME3	$97.87 \pm 0.26 \pm 0.16$
ME4	$97.78 \pm 0.09 \pm 0.29$

Figure 3.32: The CSC reconstructed segment efficiency using the SM Z pole for CSC stations. Left Panel: The efficiency comparing data with the simulation, including statistic uncertainties only. Right Panel (Table): The efficiency of the data in numbers.

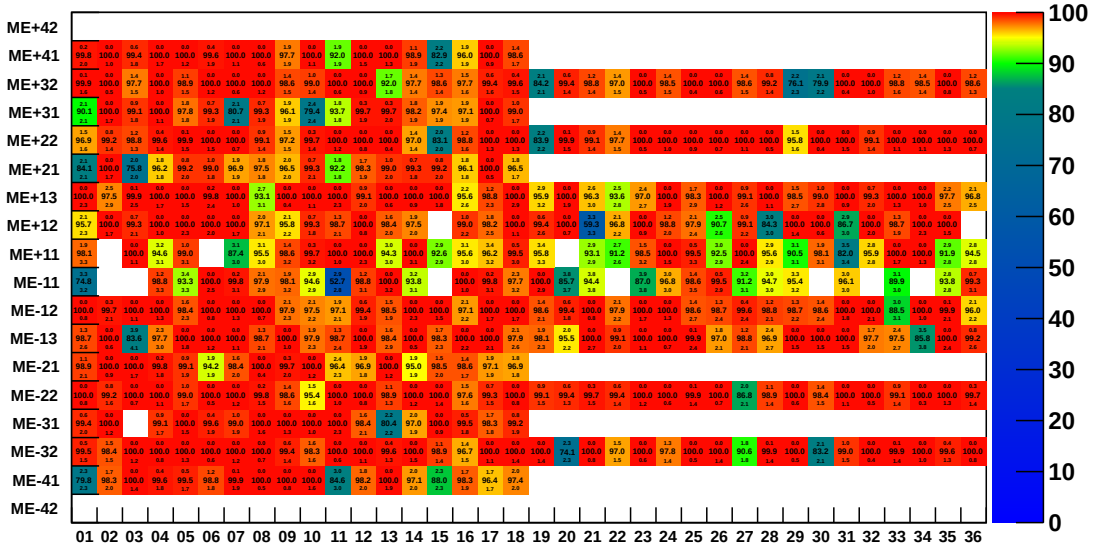

Figure 3.33: The CSC primitive LCT efficiency using the SM Z pole data for CSC chambers. The blank cells indicate dead or not considered chambers.

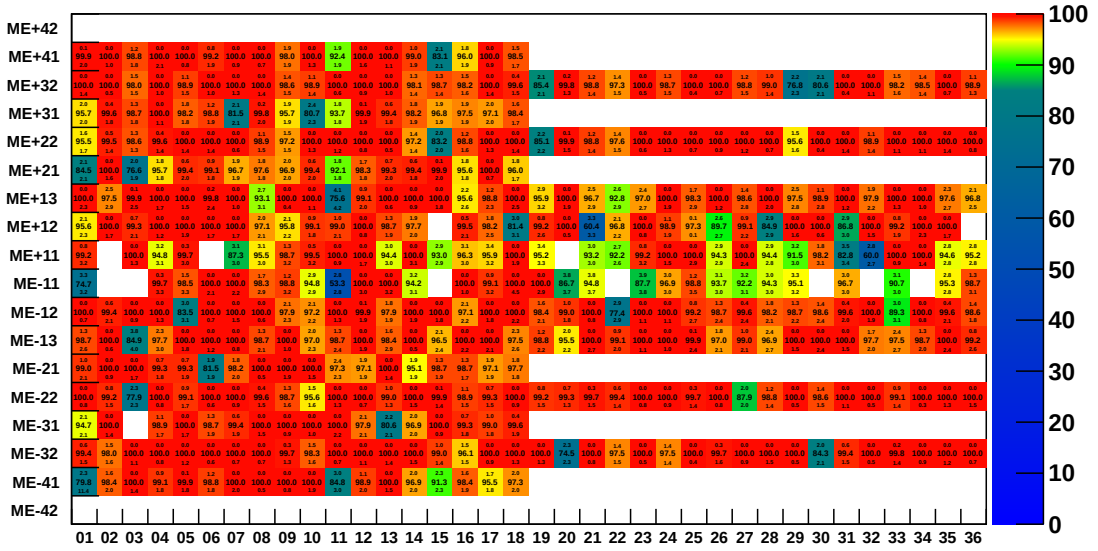

Figure 3.34: The total systematic uncertainties of the CSC reconstructed segment efficiency using the SM Z pole data for CSC chambers. The blank cells indicate dead or not considered chambers.

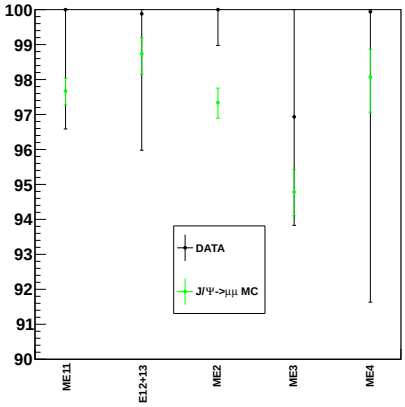

stations	efficiency±Systematic±Statistic
ME11	$100.00 \pm 1.32 \pm 3.41$
ME12+13	$99.88 \pm 0.84 \pm 3.90$
ME2	$100.00 \pm 0.14 \pm 1.03$
ME3	$96.93 \pm 1.24 \pm 3.10$
ME4	$99.94 \pm 0.09 \pm 8.31$

Figure 3.35: The CSC primitive LCT efficiency using the J/Ψ pole for CSC stations. Left Panel: The efficiency comparing data with the simulation, including statistic uncertainties only. Right Panel (Table): The efficiency of the data in numbers.

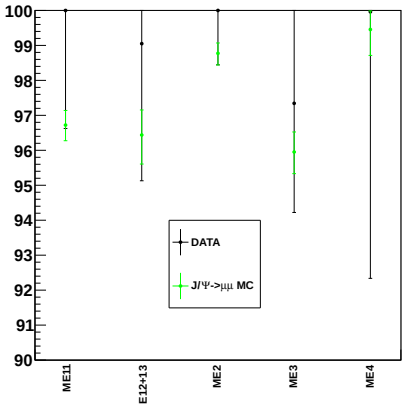

stations	efficiency±Systematic±Statistic
ME11	$100.00 \pm 1.29 \pm 3.38$
ME12+13	$99.05 \pm 1.57 \pm 3.92$
ME2	$100.00 \pm 0.97 \pm 1.56$
ME3	$97.34 \pm 0.94 \pm 3.12$
ME4	$99.96 \pm 0.46 \pm 7.62$

Figure 3.36: The CSC reconstructed segment efficiency using the J/Ψ pole for CSC stations. Left Panel: The efficiency comparing data with the simulation, including statistic uncertainties only. Right Panel (Table): The efficiency of the data in numbers.

briefly introduce part of my work corresponding to b jets in this section. Details of this work are described in [71].

The bottom and charm hadrons have relatively large masses, long lifetimes and daughter particles with hard momentum spectra. Because of those features, such hadrons can be distinguished from jets arising from the gluons (g) and light-flavour quarks (u, d, s). There are two major algorithms to identify the b-quark jets, the identification using track impact parameters and the identification using secondary vertices (SV).

In CMS, the algorithms using track impact parameters are [71]

- Track Counting High Efficiency (TCHE): The impact parameter (IP3D) of a track with respect to the primary vertex in three dimensions (3D) is used. The sign of the IP3D is taken as the sign of the scalar product of the vector pointing from the primary vertex to the point of closest approach with the jet direction. The significance of the IP3D is ratio of the IP3D and its uncertainty. The tracks in a jet are sorted decreasingly according to the significance of the IP3D. The second sorted significance is taken as the discriminator because the probability to have several tracks with high positive values is low for light-parton jets;

- Track Counting High Purity (TCHP): Similar with TCHE, instead of taking the second sorted track, it takes the third sorted track as the discriminator;

- Jet B Probability (JP): The b jet probabilities of up to four tracks in a jet are calculated as a likelihood based on the significance of the IP3D of the tracks.

Figure 3.37 shows the distributions of the TCHE and JP discriminators.

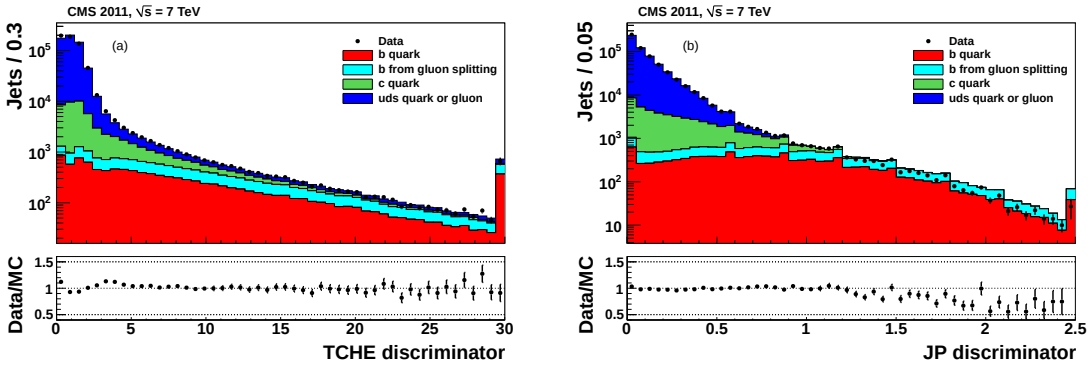

Figure 3.37: Discriminator values for (a) the TCHE and (b) the JP algorithms [71]. The data sample corresponds to a trigger selection with jet $p_{\mathrm{T}} > 60\,\mathrm{GeV}$. The distributions of the simulation are reweighted according to the pile-up distribution of the data taking period.

in CMS, the algorithms using secondary vertices are [71]:

- Simple Secondary Vertex High Efficiency (SSVHE): The flight distance is the distance between the primary vertex and the secondary vertex in 3D. The significance of the flight distance is the ratio of the flight distance to its estimated uncertainty. The SSVHE uses the significance of the flight distance of secondary vertices with at least two associated tracks as the discriminator;

- Simple Secondary Vertex High Purity (SSVHP): Similar with SSVHE, instead of requiring that the secondary vertices associate with at least two tracks, the SSVHP requires three associated tracks with the secondary vertices;

- Combined Secondary Vertex (CSV): Besides the jets with secondary vertices, the CSV algorithm also takes the jets without any secondary vertex into account. Two likelihood ratios are built from secondary vertices parameters, track impact parameters, number of tracks, and the orientations of the tracks relative to the jet. They are to discriminate between b and c jets and between b and light-parton jets. The CSV is the combination of the two likelihood ratio with prior weights of 0.25 and 0.75, respectively.

Figure 3.38 shows the distributions of the CSV discriminators and the significance of the flight distance of the secondary vertex candidates.

Comparing those algorithms, as shown in Figure 3.39, the CSV discriminator keeps less light-parton and c- jets under the same b-jet efficiency. It balances the b-jet efficiency and the b-jet purity the best.

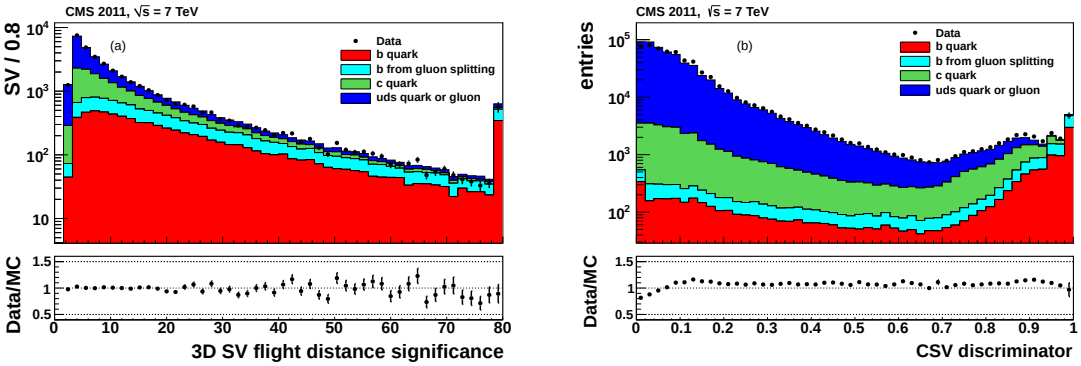

Figure 3.38: Discriminator values for (a) the significance of the 3D secondary vertex (3D SV) flight distance and (b) the CSV discriminator [71]. The data sample selection and the reweighting algorithm are the same with Figure 3.37.

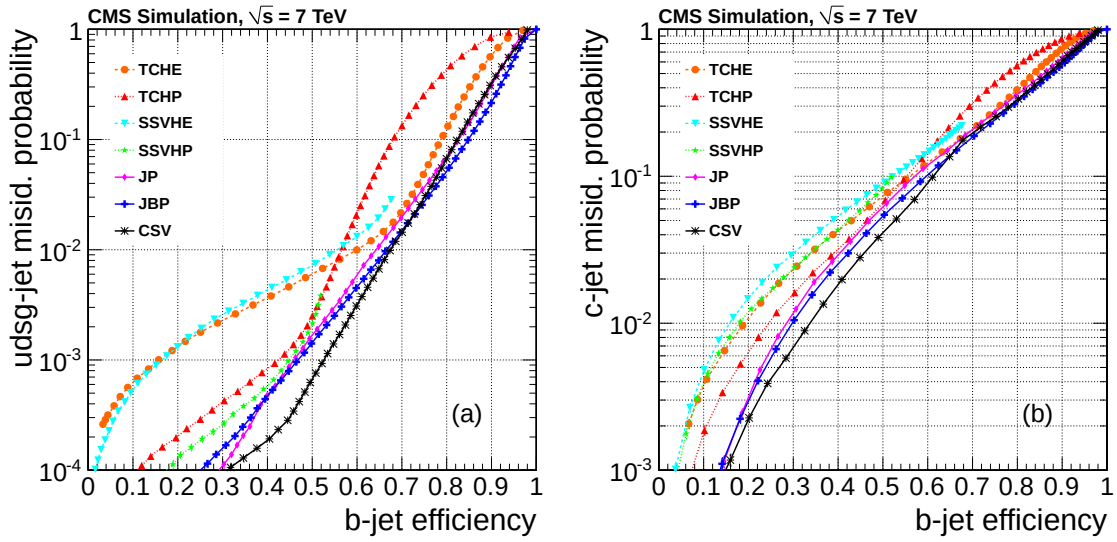

Figure 3.39: (a) light-parton- and (b) c-jet misidentification probabilities as a function of the b-jet efficiency [71]. The data sample selection and the reweighting algorithm are the same with Figure 3.37.

The high instantaneous luminosity in LHC results in 10 to 20 pile-up events per bunch crossing in CMS. I investigated the pile-up effect of the b jets identification performance by simulations. Comparing the performance without pile-up and with 12 to 16 pile-ups, Figure 3.40 shows that only the very high purity region has noticeable but not significant changes for the TCHP and SSVHP algorithms. The other IP3D based algorithms and the CSV performs similarly to the TCHP. The SSVHE performs similarly to the SSVHP.

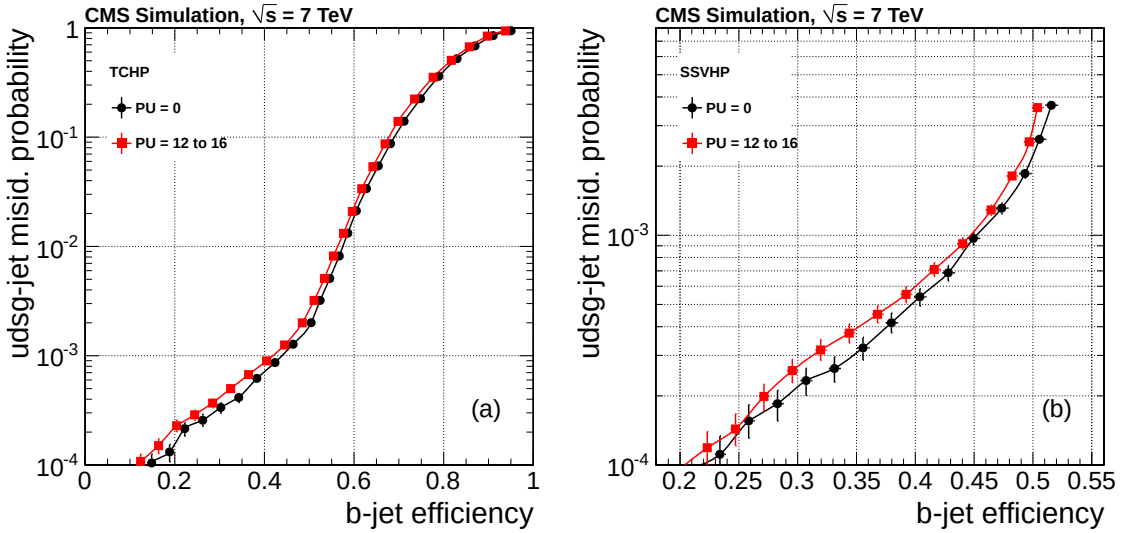

Figure 3.40: Light-parton misidentification probability versus b-jet tagging efficiency for jets with $p_{\mathrm{T}} > 60\,\mathrm{GeV}$ at generator level for the (a) TCHP and (b) SSVHP algorithms for different pile-up (PU) scenarios [71].

As a result, because the CMS pile-up events in 2011 has little effect on the CSV discriminator (Figure 3.40) and because the CSV discriminator keeps less light-parton and c- jets under the same b-jet efficiency comparing with other discriminators (Figure 3.39), the CSV is the best discriminator to distinguish the b-jets from the light-parton- and c- jets. This discriminator is widely used in all b-quark jet relating analysis in CMS.

Chapter 4

Search for High-Mass Resonances Decaying to Muon Pairs in pp Collisions

The high-mass resonance is one of the objects that most high energy experiments look for. This chapter describes the search for high-mass resonances decaying to muon pairs at an LHC center of mass energy of 7 TeV in pp collisions, corresponding to an integrated luminosity of $5.28 \pm 0.12\,\mathrm{fb}^{-1}$ as collected in 2011 [72]. The instantaneous luminosity was around $10^{32} \sim 10^{33}$ $\mathrm{cm}^{-2}\mathrm{s}^{-1}$ corresponding to an average about 10 pile-up events happening simultaneously each bunch crossing. The result will be presented as the ratio of the production cross section times branching fraction for high-mass resonances (Z') to that for the standard model Z boson:

$$R_\sigma = \frac{\sigma(\mathrm{Z}') \times \mathrm{BR}(\mathrm{Z}' \to \mu^+\mu^-)}{\sigma(\mathrm{Z}) \times \mathrm{BR}(\mathrm{Z} \to \mu^+\mu^-)}. \tag{4.1}$$

The search uses events in which dimuon invariant mass is larger than 200 GeV. The events in $120 \sim 200$ GeV invariant mass region are investigated as a monitoring sample. The resonance peak limit setting starts at 300 GeV.

Since the result of the search of $\sqrt{s} = 8$ TeV with an integrated luminosity of $19.6\,\mathrm{fb}^{-1}$ electron data and $20.6\,\mathrm{fb}^{-1}$ muon data collected in 2012 has not been published yet, the preliminary results are put in the appendix.

4.1 Selections

4.1.1 Trigger

The lowest p_T threshold un-prescaled[1] single muon trigger is selected. Because of the huge number of low p_T muons and because of the limitation of the networking capacity and computing power, the low p_T muons are highly prescaled and are not used in the high-mass resonances search. The lowest un-prescaled single muon trigger p_T threshold in both 2011 and 2012 data is 40 GeV.

Because the ME±1/1 stations read out three strip signals simultaneously, the online momentum measurement is compromised in the ME±1/1 covered region. As a result, though the coverage of the muon system extends to $|\eta| < 2.4$, because the ME±1/1 stations cover $2.1 < |\eta| < 2.4$, the acceptance of this single muon trigger is restricted to the pesudorapidty range $|\eta| < 2.1$ in both 2011 and 2012 data taking.

The simulated trigger efficiency is plotted in Figure 4.1.

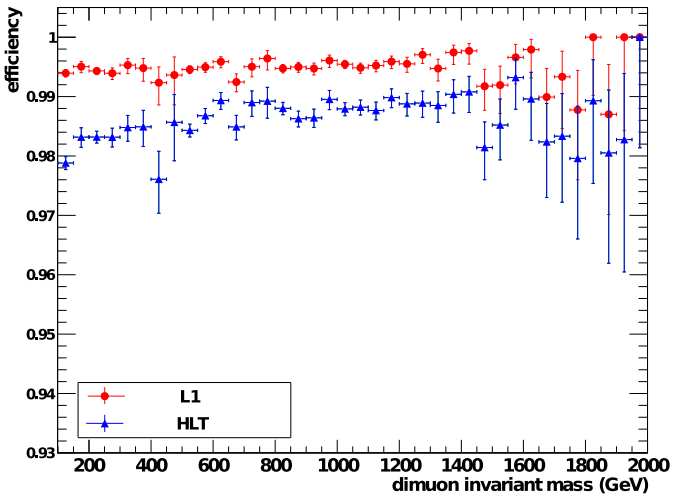

Figure 4.1: The simulated efficiency of the level 1 single muon path (p_T threshold = 12 GeV) and the HLT single muon path (p_T threshold = 40 GeV, $|\eta| < 2.1$) (from the CMS internal note AN-2011-472) .

4.1.2 Event Selection

In order to remove the underlying events, if less than a quarter of tracker tracks are marked as *high-purity*, the event will be removed. After the standard track recon-

[1] *Prescale* means that instead of filtering on all events, only a set fraction of events goes into the trigger selection. The reciprocal of that fraction is the prescale factor.

struction, high-purity tracks [73] require, in addition, $|d_z| < 10\Delta_{d_z}$ and $\Delta_{p_T}/p_T < 10\%$, where d_Z is the longitudinal distance from the primary vertex to the track; Δ represents the uncertainty.

Another requirement to reduce the underlying and cosmic event rates is to demand at least one good primary interaction vertex (PV). A *good primary vertex* has to associate at least four tracker tracks and satisfy $|z| < 24\,\text{cm}$, $r < 2\,\text{cm}$ according to the beam interaction spot (BS).

The reconstructed primary vertices are sorted according to the sum of the ${p_T}^2$ of the tracks associated with each vertex, from large to small. Only the physics objects associated with the first (the largest sum of ${p_T}^2$ of the tracks) primary vertex are used in this analysis, because the rest of the primary vertices are likely from underlying events and pile-up events and because the more energy the event has, the less likely it is from QCD or $t\bar{t}$ background process.

4.1.3 Muon and Dimuon Selection

Muon Isolation

As opposed to the muons from the QCD jets, the muons from the electroweak interaction vertex do not tend to be produced near tracks in jets. Tracker tracks inside a cone around the muon tracker track and from the same primary vertex with the muon tracker track are considered, as indicated by Figure 4.2. The size of the hollow cone can be expressed as solid angular distance in the (η, ϕ)-plane: $0.015 < \Delta R = \sqrt{(\Delta\eta)^2 + (\Delta\phi)^2} < 0.3$, where $\Delta\eta$ and $\Delta\phi$ are the differences of η and ϕ between the momentum of the muon tracker track and that of the investigating tracker track. The ratio of the sum of the p_T of all tracker tracks inside the cone to the muon tracker track p_T is used as the isolation discriminator in this analysis, which is named *tracker relative isolation*.

Single Muon Selection

Balancing the fake rate and the efficiency [74], the following cuts have been tuned and used in the dimuon analysis.

- the muon must be reconstructed as both global muon and tracker muon;
- muon $p_T > 35\,\text{GeV}$;
- muon $|\eta| < 2.4$;

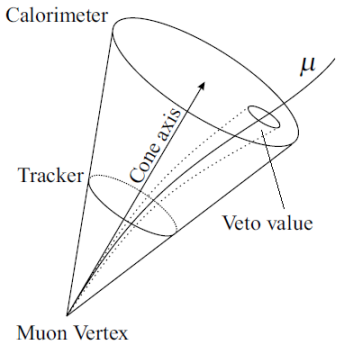

Figure 4.2: The muon isolation cone [1]. The cone axis it along the momentum of the muon tracker track. In this analysis, the veto value of the cone size is 0.015.

- in the $xy-$plane, the distance from the beam-spot (BS) to the trajectory of the tracker track seed of the global muon (transverse impact parameter, d_{xy}) must be less than 2 mm;
- the global muon track must include more than ten hits in the tracker system. At least one of those tracker hits must come from the pixel detector;
- the global muon track must include more than one hits in the muon system;
- the tracker muon must be matched to segments in at least two muon stations;
- isolation cut – the tracker relative isolation:

$$\sum_{\text{tracks inside the cone}} p_{\mathrm{T}} < 10\% \cdot p_{\mathrm{T}} \text{ of the muon tracker track.}$$

Dimuon Selection

The dimuon selection critera and the corresponding motivations are listed below:

- require opposite-charge muons because of the theory requirement and further because the charge flip of a track results a suspect momentum measurement: If the quality of the reconstruction of a particle path is bad, the reconstructed track could bend on a opposite direction to the reality, which results in a charge flip. In this case, the low quality of the reconstructed momentum of the track is not trustable;
- in order to remove the cosmic-ray muons that pass through the interaction point in time, the angle between the two muon momenta in three dimensions must be less than $\pi - 0.02$ rad;

- the normalized χ^2 of the fit to the dimuon vertex must be less than 10, as a muon reconstruction quality cut;

4.2 Pile-up and Alignment Effect

The pile-up events create more tracks, especially in the tracker system, and deposit more energy into the calorimeters.

Because this analysis requires that both muons come from the first primary vertex and because the tracks from the pile-up events are not associated with the first primary vertex, the effect of the extra tracks in the tracker system is not significant.

Figure 4.3 shows a comparison between the tracker relative isolation and an isolation method in which the energy summation includes both tracker tracks and the calorimeter energy deposits. It indicates that the tracker relative isolation that is used in this analysis is not sensitive to pile-up events.

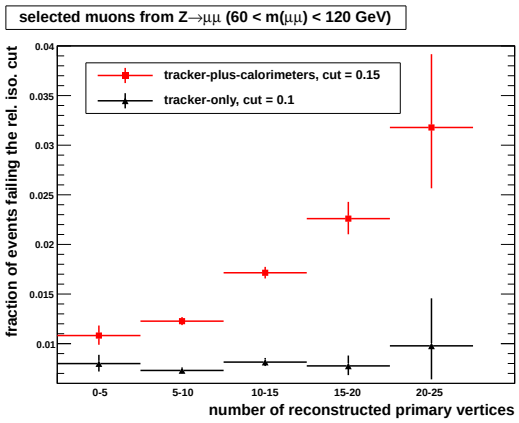

Figure 4.3: The fraction of muons failing the isolation cut from dimuons on the standard model Z peak ($60 < M_{\mu\mu} < 120\,\text{GeV}$) as a function of the number of primary vertices (from the CMS internal note AN-2011-472) . The tracker relative isolation cut is at 10%. The tracker-plus-calorimeters relative isolation cut is at 15%.

The detector mis-alignment effect has been already considered in the simulation and studied with the invariant mass resolution. It has negligible impact on the result.

4.3 Dimuon Efficiency

In Figure 4.4, the blue line shows the total reconstruction efficiency (geometry acceptance $\times$ trigger efficiency $\times$ selection efficiency) for dimuons from simulated

Drell–Yan events. The efficiency is modeled as:

$$\epsilon(M_{\mu\mu}) = a_\epsilon + \frac{b_\epsilon}{(M_{\mu\mu} + c_\epsilon)^3} \tag{4.2}$$

where $a_\epsilon = 0.849$, $b_\epsilon = -1.22 \times 10^8$, and $c_\epsilon = 510.0$ for the simulation corresponding to the 2011 CMS data.

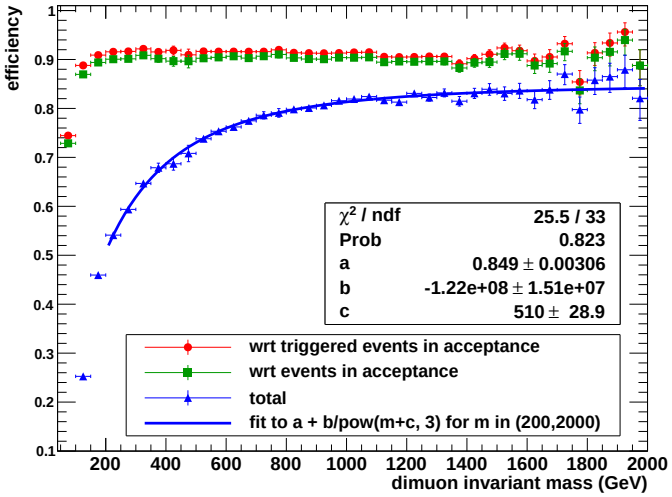

Figure 4.4: The reconstruction efficiency for dimuons from simulated Drell–Yan events passing the single muon and dimuon selections with respect to triggered events in acceptance (red) and with respect to all events in acceptance (green) (from the CMS internal note AN-2011-472) . The acceptance means that both muons satisfy $|\eta| < 2.4$ and $p_{\mathrm{T}} > 35\,\mathrm{GeV}$. The total acceptance times efficiency is shown as a blue line .

Because limit setting is based on the ratio of cross sections for Z′ bosons relative to standard model Z bosons, the uncertainty of the total efficiency comes from the following three parts.

- the uncertainty in the counts of the standard model Z boson excluding the luminosity uncertainty: because the luminosity cancels while taking the ratio, the other uncertainties are evaluated as 2% [75];
- the uncertainty in the ratio of the efficiency of this analysis to that of the standard model Z analysis: This analysis takes dimuons from the Z pole to the high mass region into account while the Z analysis uses the uncertainty around the Z pole with a little different dimuon selections. This uncertainty is estimated roughly as 1.5% by taking the region close to 1 TeV in Figure 4.4 as a typical example;

- the uncertainty in the muon showering in the high mass region: by calculation [76], for a 1 TeV muon, about 2.6% muons lost more than 10% of their energy while passing through 3 m iron. For the $1 \sim 2$ TeV invariant mass region that we are concerned about, 2% uncertainty is assigned.

By adding the above three components in quadrature, the total efficiency uncertainty is estimated as

$$\sqrt{(2\%)^2 + (1.5\%)^2 + (2\%)^2} = 3.2\%. \tag{4.3}$$

4.4 Dimuon Invariant Mass Resolution

By use of the simulation and based on the selections mentioned in the previous sections, the reconstructed dimuon invariant mass is compared with the generation level muon dimuon invariant mass. Figure 4.5 illustrates the mass resolution of the dimuon as a function of the generator level dimuon invariant mass.

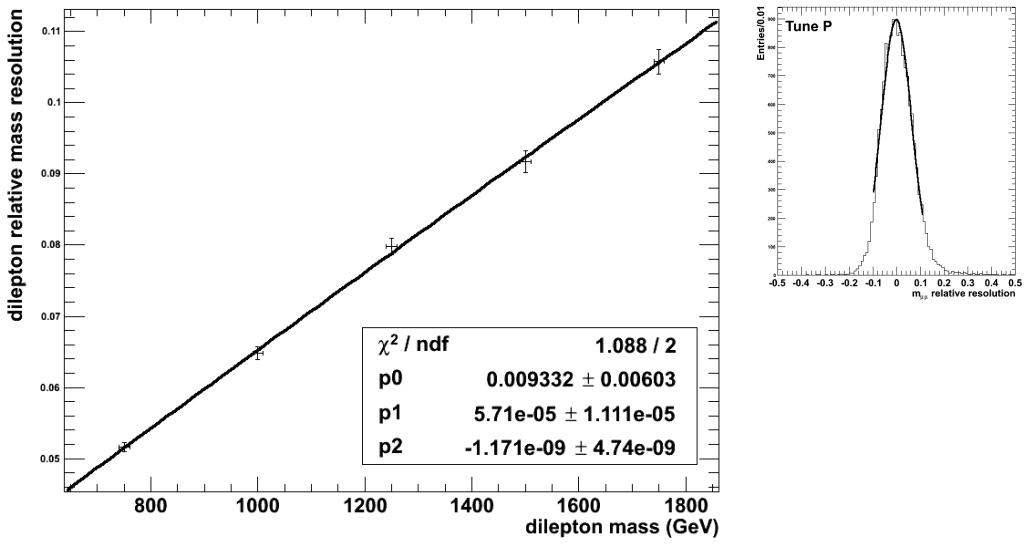

Figure 4.5: The dimuon mass resolution as a function of the generator level dimuon invariant mass (from the CMS internal note AN-2011-278). A quadratic polynomial fit is overlaid. At each dimuon mass point, a fitted Gaussian width of the relative resolution distributions ($|M_{\mu\mu}{}^{\text{reconstructed}} - M_{\mu\mu}{}^{\text{generated}}|/M_{\mu\mu}{}^{\text{generated}}$) is plotted, as illustrated in the top right panel.

The quadratic polynomial fit in Figure 4.5 shows that the dimuon invariant mass resolution is:

$$\Delta_{M_{\mu\mu}} = M_{\mu\mu} \times (p_0 + p_1 M_{\mu\mu} + p_2 M_{\mu\mu}^2), \tag{4.4}$$

where $M_{\mu\mu}$ is the dimuon invariant mass.

For the simulation used with the 2011 CMS data, the values obtained from a fit of the dimuon invariant mass are $p_0 = 0.009332$, $p_1 = 5.71 \times 10^{-5}\,\mathrm{GeV}^{-1}$, and $p_2 = -1.171 \times 10^{-9}\,\mathrm{GeV}^{-2}$ (from the CMS internal note AN-2011-278) .

Because this resolution function is only fitted for the high invariant mass region, the standard model Z resonance peak does not yield good results. As mentioned in Section 3.5.1, the refit algorithm used in the global muon reconstruction is selected among three algorithms — picky, tracker-only, and TPFMS. The simulation is checked with data by comparing how often each algorithm is chosen. The results of the comparison are taken from the CMS internal note AN-2011-278 and shown in Table 4.1. The comparison shows that the simulation agrees well with data with $|\eta| < 2.4$. As the dimuon invariant mass is obtained from the global muons' momenta, this check on the global muon reconstruction algorithm shows that the resolution result from simulation is reliable.

Muon location	DY Simulation			$1.1\,\mathrm{fb}^{-1}$ Data		
	Events	% TPFMS	% picky	Events	% TPFMS	% picky
$\lvert\eta\rvert < 0.85$	1386	44 ± 1	55 ± 1	87	47 ± 6	52 ± 6
$0.85 < \lvert\eta\rvert < 1.2$	1886	$47 - 2 + 1$	$53 - 1 + 2$	110	$49 - 4 + 6$	50 ± 5
$1.2 < \lvert\eta\rvert < 2.4$	1136	$68 - 2 + 1$	31 ± 1	66	$58 - 7 + 6$	41 ± 7

Table 4.1: The fraction of muons (in percent) in which the global muon reconstruction chooses either TPFMS or picky (from the CMS internal note AN-2011-278). The comparison is between $1.1\,\mathrm{fb}^{-1}$ proton-proton collision data in 2011 and the DY simulation. The uncertainties are shown by the + and − signs with numbers. For tracker-only algorithm, it is around or below 1% and is not shown.

4.5 Background Estimation

Sorted by the background rates from large to small, the backgrounds in this analysis include dimuons for the Drell–Yan process, $\mathrm{t\bar{t}}$, *$\bar{t}t$-like* processes, mis-identified muons from jets and cosmic-ray events. The $\mathrm{t\bar{t}}$-like processes include $W^+W^- \to \mu^+ + \nu_\mu + \mu^- + \bar{\nu_\mu}$, WZ, ZZ, tW, $\bar{\mathrm{t}}$W, and $\mathrm{Z}/\gamma \to \tau^+\tau^-$. Figure 4.6 gives a comparison between the backgrounds and the data.

The following sections describe and model the backgrounds in detail.

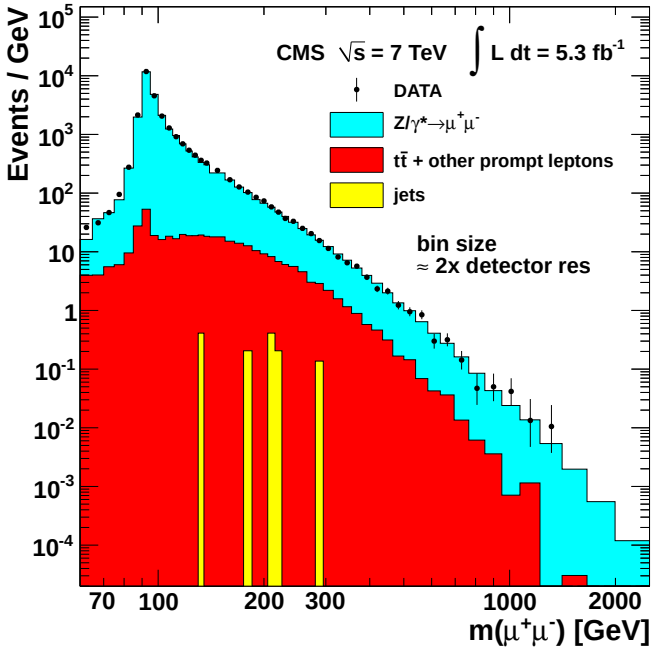

Figure 4.6: The invariant mass spectrum of dimuons under $5.3\,\mathrm{fb}^{-1}$.[72]. Except for Drell–Yan, jets and cosmic background, the other kinds of backgrounds are shown in red . The cosmic background is supposed to be reduced to a negligible rate by the anti-cosmic dimuon cut (the angle between the two muon momenta in three dimensions must be less than $\pi - 0.02\,\mathrm{rad}$) so that they are not shown.

4.5.1 Drell–Yan (DY) Background

The Drell–Yan background is the process where dimuons result from the decays of the photons and the off-mass shell standard model Zs. These events are indistinguishable from a new heavy-resonance decay. Thus DY is the dominant and irreducible background in this analysis.

The Drell–Yan background shape is modeled as,

$$pdf_{\,\mathrm{DY}}(M_{\mu\mu}; a_{\mathrm{DY}}, b_{\mathrm{DY}}) = Ae^{a_{\mathrm{DY}} \cdot M_{\mu\mu}} {M_{\mu\mu}}^{b_{\mathrm{DY}}}, \tag{4.5}$$

where *pdf* means the probability distribution function; A is the normalization factor; $a_{\mathrm{DY}} = -0.002423$ and $b_{\mathrm{DY}} = -3.625$ for the simulation corresponding to the 2011 CMS data, as shown in Figure 4.7.

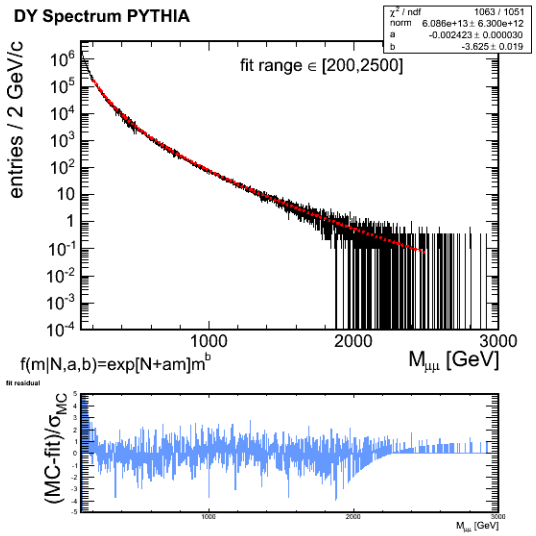

Figure 4.7: Fit to the LO DY dimuon mass spectrum simulated by PYTHIA6.4 [77] (from the CMS internal note AN-2011-472) . The residuals are shown in the lower panel.

The uncertainties in the Drell–Yan background shape come from the higher order cross section correction and the uncertainty in the CTEQ6L1 PDF set. As seen from the k-factor uncertainty discussed in the last chapter (Equation 2.15), the uncertainty in the DY background higher order cross section is conservatively assigned as 6%. The PDF uncertainty is calculated using the LHAGLUE interface to the parton distribution functions library LHAPDF [78, 79]. As seen from Figure 4.8, the PDF uncertainties vary from 4% at 400 GeV to 16% at 1.5 TeV and 20% at 2 TeV. An average uncertainty of 10% was set. Because there are about 0 to 1 events in the

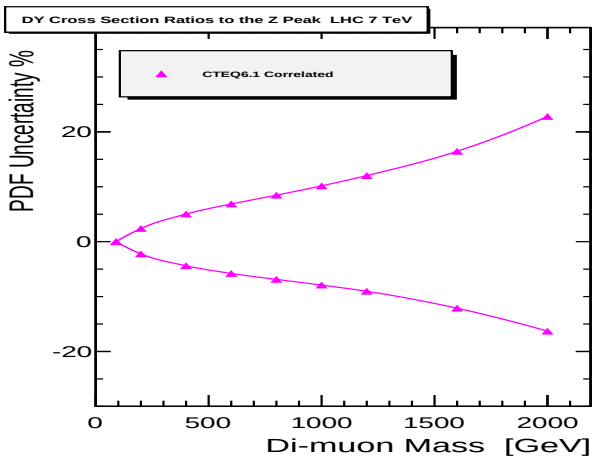

Figure 4.8: PDF uncertainties in the Drell–Yan dimuon channel predictions for the acceptance (from the CMS internal note AN-2007-038) . The cross section is normalized to events at the standard model Z peak. Each DY dimuon sample is generated for each data point. As a set of 40 PDFs for CTEQ6L1 is used, one could expect the upward or downward deviations from the central value for a given PDF member from the PDF set to be preserved for adjacent mass bins, and thus have a reduced impact on the cross section ratios. This "correlated" effect is computed by the reweighting technique with asymmetric errors as described in [80].

Drell–Yan simulation above 1.5 TeV, $15 \sim 20\%$ uncertainty and less than one event has little effect on the dimuon invariant mass spectrum.

As a result, the DY background estimation has $\sqrt{(6\%)^2 + (10\%)^2} = 11.7\%$ uncertainty on its shape.

4.5.2 Other Prompt Muon Pairs – $t\bar{t}$ and $t\bar{t}$-like Backgrounds

In the $t\bar{t}$ decay, $t(\bar{t}) \to W^+(W^-) + b(\bar{b}), W^+(W^-) \to \mu^+(\mu^-) + \nu_\mu(\bar{\nu_\mu})$, if both muons appear to come from the same vertex rather than from heavy flavor decay, the event will go into the spectrum of dimuon invariant mass. The $t\bar{t}$-like events have a similar effect.

Because the decay rate of a heavy flavor boson/fermion to a muon and to an electron are theoretically the same,

$$\frac{N_{\mu^\pm\mu^\mp}}{\epsilon_{\mu^\pm\mu^\mp}} = \frac{1}{2}\frac{N_{e^\pm\mu^\mp}}{\epsilon_{e^\pm\mu^\mp}},$$

where N is the number of reconstructed $\mu^\pm\mu^\mp(e^\pm\mu^\mp)$ events from heavy flavor decays and $\epsilon_{\mu^\pm\mu^\mp}(\epsilon_{e^\pm\mu^\mp})$ is the total acceptance times efficiency. Thus the number of reconstructed $\mu^\pm\mu^\mp$ events from heavy flavor decay is expected to be

$$N_{\mu^\pm\mu^\mp} = \frac{1}{2}\frac{\epsilon_{\mu^\pm\mu^\mp}}{\epsilon_{e^\pm\mu^\mp}} N_{e^\pm\mu^\mp}.$$

The ratio of the acceptance times efficiency, $\epsilon_{\mu^\pm\mu^\mp}/\epsilon_{e^\pm\mu^\mp}$, is slightly different in different mass bins and varies a little for different decay processes. By use of $t\bar{t}$ simulation, a general $\epsilon_{\mu^\pm\mu^\mp}/\epsilon_{e^\pm\mu^\mp}/2$ factor is calculated for each mass bin. For the other $t\bar{t}$-like processes, because of their smaller contribution to the spectrum and because the difference in $\epsilon_{\mu^\pm\mu^\mp}/\epsilon_{e^\pm\mu^\mp}$ with respect to $t\bar{t}$ is tiny, the general factors derived from the $t\bar{t}$ simulation are accurate enough. The expected number of $t\bar{t}$ and $t\bar{t}$-like events in the dimuon spectrum are thus estimated from the $e\mu$ events from collisions. Table 4.2 summarizes the results at $4.98\,\text{fb}^{-1}$ (the integrated luminosity of the electron data).

4.5.3 Non-prompt Muon Pairs – Misidentified Muons from Jets

Tracks from jets can be misreconstructed as prompt muons from the interaction point and pass the isolation cut. The main sources that could form muon pairs are QCD jets and W+jets where the muon from W boson leptonic or hadronic decay

$M_{\mu\mu}$ (GeV)	$\frac{1}{2}\frac{\epsilon_{\mu^\pm\mu^\mp}}{\epsilon_{e^\pm\mu^\mp}}$	$N^{\text{observed}}_{e^\pm\mu^\mp}$	$N^{\text{prediction}}_{\mu^\pm\mu^\mp}$
$120 \sim 200$	0.55 ± 0.01	1961	1079 ± 31
$200 \sim 400$	0.64 ± 0.02	836	535 ± 24
> 400	0.65 ± 0.08	69	45 ± 8

Table 4.2: The predicted number of dimuon events from observed heavy flavor decays at $5.3\,\text{fb}^{-1}$ (numbers are from the CMS internal note AN-2011-472) . The uncertainties of $N^{\text{prediction}}_{\mu^\pm\mu^\mp}$ given are the combination of the observed statistical uncertainties and simulated $\epsilon_{\mu^\pm\mu^\mp}/\epsilon_{e^\pm\mu^\mp}/2$ uncertainties, e.g. $31 = 1079\sqrt{(0.01/0.55)^2 + 1/1961}$.

is reconstructed as a prompt muon and one jet is reconstructed as another prompt muon.

The estimation is done by the following steps.

1. Obtain $p(\text{isolated muon}|\eta, p_{\text{T}})$ from collision data: It is the the probability that a single muon could pass the isolation cut. The probability $p(\text{isolated muon}|\eta, p_{\text{T}})$ equals the number of muons that pass all single muon selections divided by the number of muons that pass single muon selections except the isolation cut. The result is shown in Figure 4.9.

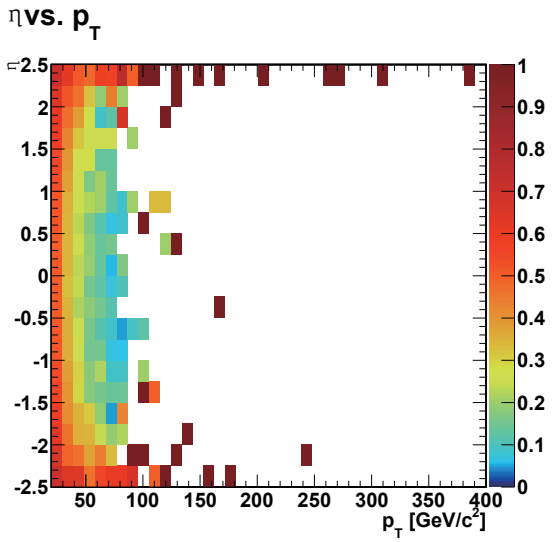

Figure 4.9: The probability of a muon passing the isolation cut as a function of global muon η and p_{T} (from the CMS internal note AN-2010-317) .

2. Calculate p(QCD and W+jets muon$|\eta, p_{\mathrm{T}}$) from simulation: It is the probability of a single muon arising from the QCD jets or W+jets with respect to all single muons used in this analysis. The probability

$$p(\text{QCD and W+jets muon}|\eta, p_{\mathrm{T}})$$

is calculated as the fraction of muons from the QCD jets and W+jets for each (η, p_{T}) bin.

3. Calculate the probability of an isolated muon that is from the QCD jets and W+jets:

$$p(\text{iso jet muon}|\eta, p_{\mathrm{T}}) = p(\text{isolated muon}|\eta, p_{\mathrm{T}})p(\text{QCD and W+jets muon}|\eta, p_{\mathrm{T}}).$$

4. Calculate the probability of a dimuon event in which both muons are from QCD jets and W+jets:

$$\begin{aligned} & p(\text{QCD and W+jets fake dimuon}) \\ = \; & p(\text{iso jet muon 1}|\eta_1, p_{\mathrm{T}1})p(\text{iso jet muon 2}|\eta_2, p_{\mathrm{T}2}). \end{aligned}$$

The correlation between the two muons is found to be insignificant when $M_{\mu\mu} > 50\,\mathrm{GeV}$ (from the CMS internal note AN-2010-317) . Since the signal region of this analysis is above 200 GeV, the two muons can be considered as independent from each other.

5. Reweigh each dimuon event with the probability found in step four and give the predicted jet muon spectrum.

Calculating from the 2011 CMS data, the result is given in the following table (numbers are from the CMS internal note AN-2011-472) .

$M_{\mu\mu}$ (GeV)	number of predicted $\mu^+\mu^-$ from QCD and W+jets
$120 \sim 200$	8.25 ± 0.33
$200 \sim 400$	2.91 ± 0.19
$400 \sim 600$	0.29 ± 0.07
> 600	0.05 ± 0.04

4.5.4 Cosmic-ray Muons

In order to remove the cosmic-ray muons that pass through the interaction point in time, we require that the angle between the two muon momenta in three dimensions must be less than $\pi - 0.02\,\mathrm{rad}$. Based on a comparison between collision and cosmic

data, Figure 4.10 indicates that approximately 99% of cosmic events are rejected by this cut. The number of cosmic events in the signal region can be estimated roughly by dividing the number of events observed in the 3D angle$\geqslant \pi - 0.02$ rad region by 99.

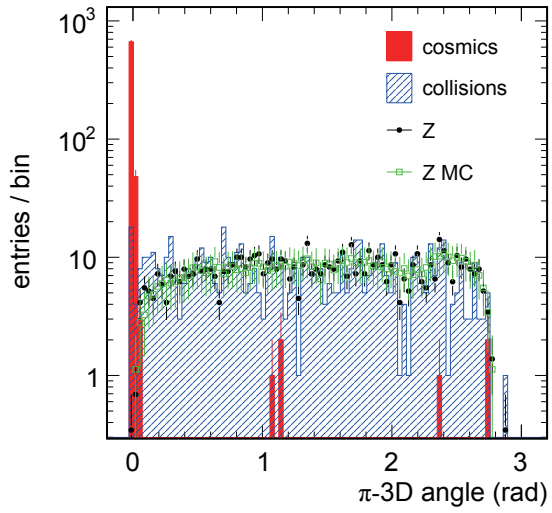

Figure 4.10: Distribution of the 3D angle of the cosmic muons and the collision single muon sample (corrected from the CMS internal note AN-2010-317) .

The dimuon events with 3D angle$\geqslant \pi - 0.02$ contains both cosmic muons and dimuon events from collisions. To further accurately estimate the number of cosmic muons that do not pass the 3D angle cut, the good primary vertex requirement[2] and the transverse impact parameter $d_{xy} < 2$mm cuts are removed alternatively. For a cosmic muon, those two cuts practically have negligible correlation. The cut efficiency of applying both cuts thus equals the product of the efficiencies of applying the two cuts separately. The number of cosmic events with 3D angle$\geqslant \pi - 0.02$ is thus expressed as

$$
\begin{aligned}
& N_{\text{cosmic}}(n\text{PV} > 0, d_{xy} < 2\,\text{mm}) \\
= \; & \frac{N_{\,\text{cosmic}}(n\text{PV} > 0)}{N_{\text{cosmic}}(\text{total})} \times \frac{N_{\,\text{cosmic}}(d_{xy} < 2\,\text{mm})}{N_{\text{cosmic}}(\text{total})} \times N_{\,\text{cosmic}}(\text{total}),
\end{aligned}
$$

where $N_{\text{cosmic}}(\text{total})$ is the total number of cosmic events with 3D angle$\geqslant \pi - 0.02$ but without 3D angle cut and d_{xy} cut; $N_{\,\text{cosmic}}(n\text{PV} > 0)$ is the number of cosmic events with 3D angle$\geqslant \pi - 0.02$ and with at least one good primary vertex but

[2]The definition of the good primary vertex is mentioned in section 4.1.2.

no d_{xy} requirement; $N_{\text{cosmic}}(d_{xy} < 2\,\text{mm})$ is the number of cosmic events with 3D angle$\geqslant \pi - 0.02$ and with $d_{xy} < 2\,\text{mm}$ but no good primary vertex requirement; $N_{\text{cosmic}}(n\text{PV} > 0, d_{xy} < 2\,\text{mm})$ is the number of cosmic events with all three cuts applied, which is the number that we want to know.

Figure 4.11 indicates that once we release the d_{xy} requirement, the number of cosmic events is increased hundreds of times more while the number of collision events is almost unchanged. The situation is similar for the good primary vertex requirement. It implies that $N_{\text{cosmic}}(d_{xy} < 2\,\text{mm}) \approx N_{\text{cosmic+collision}}(d_{xy} < 2\,\text{mm})$, $N_{\text{cosmic}}(n\text{PV} > 0) \approx N_{\text{cosmic+collision}}(n\text{PV} > 0)$, and $N_{\text{cosmic}}(\text{total}) \approx N_{\text{cosmic+collision}}(\text{total})$[3]. Those $N_{\text{cosmic+collision}}$s can be obtained from the collision data by removing the good primary vertex cut and d_{xy} cut alternatively.

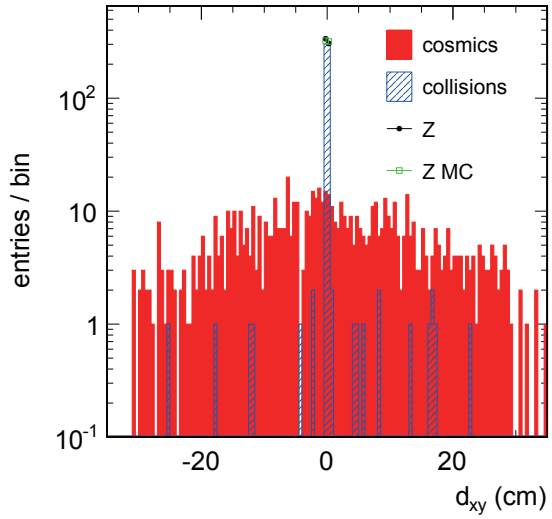

Figure 4.11: Distribution of d_{xy} of the cosmic muons and the collision single muon sample (from the CMS internal note AN-2010-317) .

The result is shown in the following table.

$M_{\mu\mu}$ (GeV)	number of predicted cosmic events with 3D angle$\geqslant \pi - 0.02$	number of predicted cosmic events with 3D angle$< \pi - 0.02$ (left column divided by 99)
> 50	less than 39	less than 0.39
> 120	less than 30	less than 0.30
> 200	less than 19	less than 0.19

[3]Notice that $N_{\text{cosmic}}(n\text{PV} > 0, d_{xy} < 2\,\text{mm}) \not\approx N_{\text{cosmic+collision}}(n\text{PV} > 0, d_{xy} < 2\,\text{mm})$.

4.5.5 Background Summary

In 2011 data, in the $M_{\mu\mu} > 200\,\text{GeV}$ region, we observed 4250 dimuon events that pass all the cuts. Estimated from data, the observed dimuon events include about $535 + 45 = 580$ $t\bar{t}$ type events, $2.91 + 0.29 + 0.05 = 3.25$ events that are QCD and W+jets processes, and less than 0.19 cosmic muon events. The non-prompt muon pairs and cosmic muon background are thus negligible. Because the $t\bar{t}$ does not change the DY shape significantly, we still use the DY shape in the background fitting with assigning $t\bar{t}$ type events as uncertainty: $580/4250 = 13.6\% \xrightarrow{\text{conservatively}} 15\%$. Taking account of the PDF uncertainty and the k-factor uncertainty obtained in section 4.5.1, the total background uncertainty is

$$\sqrt{(6\%)^2 + (10\%)^2 + (15\%)^2} = 19\% \approx 20\%. \tag{4.6}$$

4.6 Limit Setting Method

Because we did not see any obvious dilepton resonance peak above the standard model Z resonance, the ratio limits are set based on Bayes' theorem by the unbinned likelihood function, which is based on the analytic model hypothesis.

4.6.1 Analytic Model

In order to use an unbinned likelihood method, the expected dimuon spectrum shape is modeled as an analytic function. It corresponds to the number of expected signal events, the expected signal shape, the expected number of background events, and the expected background distribution, which are introduced in the following sections.

Number of Expected Signal Events

The number of expected new resonance events is modeled as a function of R_σ:

$$N_{\text{sig}}^{\text{expected}}(R_\sigma) = R_\sigma \times N_{\text{Z}}^{\text{observed}} \times \omega_{\text{pre}} \times \frac{\epsilon(M_{\mu\mu})}{\epsilon_{\text{Z}}} \times \theta_{\text{sig}}, \tag{4.7}$$

where R_σ is defined in Equation 4.1; $N_{\text{Z}}^{\text{observed}}$ is the number of observed standard model Z bosons in $60\,\text{GeV} < m_{\text{res}} < 120\,\text{GeV}$, background subtracted; ω_{pre} is the prescale factor of the trigger used for measuring the standard model Z boson; $\epsilon(M_{\mu\mu})$ is the total acceptance times efficiency of the dimuon events as a function of the resonance mass, which is defined in Equation 4.2; ϵ_{Z} is the total acceptance times efficiency of the standard model Z boson in $60\,\text{GeV} < m_{\text{res}} < 120\,\text{GeV}$; θ_{sig} is a nuisance parameter standing for the systematic uncertainty.

The nuisance parameter is modeled as a log-normal distribution:

$$Lognormal(\theta_{\rm sig};\Delta_{\rm\ sig}) = \frac{1}{\sqrt{2\pi}}\frac{1}{\theta_{\rm sig}\Delta_{\rm\ sig}}\exp\left(\frac{-\ln^2(\theta_{\rm sig})}{2\Delta^2_{\rm sig}}\right), \tag{4.8}$$

where $\theta_{\rm sig} \in [0.3, 1.7]$ to avoid extra large inputs. This range is chosen to include the most important population of the distribution (around 1) — changing the range affects the result negligibly; $\Delta_{\rm sig}$ is the efficiency systematic uncertainty that we got in Equation 4.3, 3%.

In the 2011 analysis, the number of standard model Z is counted using a prescaled single muon trigger with online calculated $p_{\rm T}$ threshold at 15 GeV and $|\eta| < 2.1$. Because the prescale factors are different in different periods, random numbers are used to select events in order to achieve an overall prescale factor of 2000, which is larger than the largest prescale factor of this trigger in 2011 data taking period. After this adjustment, 680 standard model Zs have been observed. In the 2012 analysis, similar adjustment is done. The $p_{\rm T}$ threshold of the trigger is 24 GeV. The pseudorapidity range is still $|\eta| < 2.1$. The overall prescale factor is 300. 24306 standard model Zs have been observed.

The values of the above mentioned parameters have been summarized in Table A.2 in Appendix A.

Expected Signal Shape

Theoretically, near the resonance energy, the probability distribution function (pdf) of the invariant mass follows the relativistic Breit–Wigner distribution:

$$pdf_{\rm resonance\ peak}(M_{\mu\mu};m_{\rm res},\Gamma) = \frac{1}{\pi}\frac{\Gamma/2}{\Gamma^2/4+(M_{\mu\mu}-m_{\rm res})^2}, \tag{4.9}$$

where Γ is the decay width of the resonance, $M_{\mu\mu}$ is the dimuon invariant mass, and $m_{\rm res}$ is the investigating resonance mass.

The natural decay width is smeared by the detector mass response, which follows the Gaussian distribution:

$$pdf_{\rm mass\ respond}(M_{\mu\mu};m_{\rm res},\Delta_{M_{\mu\mu}}) = \frac{1}{\sqrt{2\pi}\Delta_{M_{\mu\mu}}}\exp\left(-\frac{(M_{\mu\mu}-m_{\rm res})^2}{2\Delta^2_{M_{\mu\mu}}}\right), \tag{4.10}$$

where $\Delta_{M_{\mu\mu}}(M_{\mu\mu})$ is from Equation 4.4.

The $pdf_{\rm sig}$ distribution is the convolution of the above two:

$$\begin{aligned} & pdf_{\rm sig}(M_{\mu\mu};m_{\rm res},\Gamma,\Delta_{M_{\mu\mu}}) \\ = \ & pdf_{\rm resonance\ peak}(M_{\mu\mu};m_{\rm res},\Gamma)\otimes pdf_{\rm mass\ respond}(M_{\mu\mu};m_{\rm res},\Delta_{M_{\mu\mu}}), \end{aligned} \tag{4.11}$$

which is the Voigtian distribution.

In the published analysis [81], Γ is chosen to be the decay width of the sequential standard model Z′, which depends on the mass of the resonance:

$$\Gamma(m_{\text{res}}) = -1.2979\,\text{GeV} + 0.0309 \times m_{\text{res}}, \tag{4.12}$$

where m_{res} is in units of GeV.

The decay width of the Z'_{St}(Figure 2.2) is several orders of magnitude less than the dimuon invariant mass resolution (Figure 4.5). The decay width can then be treated as zero and pdf_{sig} reduces back to the Gaussian distribution. Both the expected and observed invariant mass exclusion limits increase by about $20 \sim 40\,\text{GeV}$. This will be further discussed in Section 4.7.3.

Number of Expected Background Events

Because we did not see any significant resonance peak above 200 GeV in the dimuon spectrum, the observed dimuon events above 200 GeV are considered as the background and a limit is set. The number of the expected background dimuon events, $N_{\text{bkg}}^{\text{expected}}$, is the product of the number of observed dimuon events above 200 GeV and a nuisance parameter,

$$N_{\text{bkg}}^{\text{expected}} = N_{M_{\mu\mu}>200\,\text{GeV}}^{\text{observed}} \times \theta_{\text{bkg}}.$$

In 2011 data, $N_{M_{\mu\mu}>200\,\text{GeV}}^{\text{observed}} = 4250$. The nuisance parameter θ_{bkg} is modeled as log-normal distribution with $\theta_{\text{bkg}} \in [0, 2.0]$ and $\Delta_{\text{bkg}} = 20\%$ (Equation 4.6).

Expected Background Shape

In the 2011 analysis, since there are only abount ten high mass events and the $\text{t}\bar{\text{t}}$-like background only contributes significantly in the high invariant mass range, the Drell–Yan background shape is used as the expected background probability distribution:

$$pdf_{\text{bkg}} = pdf_{\text{DY}}(M_{\mu\mu}; a_{\text{DY}}, b_{\text{DY}}).$$

In the 2012 analysis, to improve the fit at high invariant dimuon masses, the fit was performed on the total expected background spectrum, including the $\text{t}\bar{\text{t}}$-like events, jets, and others. In addition, a quadratic term in the exponential was added to improve the fit with $M_{\mu\mu} \gtrapprox 2500\text{GeV}$. The fit is

$$pdf_{\text{bkg}}(M_{\mu\mu}; a_{\text{bkg}}, b_{\text{bkg}}, c_{\text{bkg}}) = A e^{a_{\text{bkg}} \cdot M_{\mu\mu} + c_{\text{bkg}} \cdot {M_{\mu\mu}}^2} {M_{\mu\mu}}^{b_{\text{bkg}}}, \tag{4.13}$$

In the following sections, the fit in 2011 analysis will be kept in. The difference and parameters used in 2012 analysis are summarized in Appendix A.

Total Expected Shape

The total expected pdf of the dimuon spectrum is thus the normalized summation of the signal and background pdf (2011 analysis):

$$\begin{aligned} & pdf_{\text{ dimuon}}(M_{\mu\mu}; R_\sigma; m_{\text{res}}; \Gamma, \Delta_{M_{\mu\mu}}, a_{\text{DY}}, b_{\text{DY}}; \theta_{\text{ sig}}, \theta_{\text{bkg}}) \\ = & \frac{N_{\text{sig}}^{\text{expected}}(R_\sigma) \times pdf_{\text{ sig}}(M_{\mu\mu}; m_{\text{res}}, \Gamma, \Delta_{M_{\mu\mu}}) + N_{\text{bkg}}^{\text{expected}} \times pdf_{\text{DY}}(M_{\mu\mu}; a_{\text{DY}}, b_{\text{DY}})}{N_{\text{total}}^{\text{expected}}}, \end{aligned} \tag{4.14}$$

where $N_{\text{total}}^{\text{expected}} = N_{\text{sig}}^{\text{expected}} + N_{\text{bkg}}^{\text{expected}}$; the parameters are categorized as the limit ratio R_σ, the resonance peak mass m_{res}, the model shape parameters, and the nuisance variables.

$pdf_{\text{DY}}(M_{\mu\mu}; a_{\text{DY}}, b_{\text{DY}})$ is the shape of the simulated Drell–Yan dimuon spectrum, which is defined by Equation 4.5.

4.6.2 Profile Likelihood Limit Estimation

The likelihood function is proportional to the probability of the observed spectrum under the hypothesis of the expected distribution. The *profile* stands for the probability of the total observed number of events in the hypothesis of the total expected number of events, which follows the Poisson distribution. So the likelihood function

$$L({M_{\mu\mu}}^1, {M_{\mu\mu}}^2, \ldots, {M_{\mu\mu}}^{N^{\text{ observed}}}; R_\sigma; m_{\text{res}}; \Gamma, \Delta_{M_{\mu\mu}}, a_{\text{DY}}, b_{\text{DY}}; \theta_{\text{ sig}}, \theta_{\text{bkg}}) =$$

$\frac{{N_{\text{total}}^{\text{expected}}}^{N^{\text{observed}}}}{N^{\text{ observed}}!} e^{-N_{\text{total}}^{\text{expected}}}$	the profile probability
$\times \prod_{i=1}^{N^{\text{observed}}} pdf_{\text{dimuon}}({M_{\mu\mu}}^i)$	the dimuon spectrum probability (Equation 4.14) of all observed events
$\times Lognormal(\theta_{\text{sig}})$	the signal nuisance parameter probability
$\times Lognormal(\theta_{\text{bkg}})$,	the background nuisance parameter probability

(4.15)

where i is the index of the observed dimuon event.

Starting from $m_{\text{res}} = 300\text{GeV}$, the limit setting is done for each m_{res}.

In the limit setting calculation using the Bayesian approach, the nuisance parameters are marginalized by integrating over their possible values [82], leaving the only interesting parameter R_σ:

$$L(R_\sigma) = \int_{0.3}^{1.7} \mathrm{d}\theta_{\text{sig}} \int_0^2 \mathrm{d}\theta_{\text{ bkg}} L(R_\sigma, \theta_{\text{sig}}, \theta_{\text{bkg}}).$$

Bayes' theorem states that the product of the probability of a hypothesis (model) given data and the prior probability of data equals the product of the probability of obtaining the data given a hypothesis and the prior probability of the hypothesis:

$$L(\text{model}|\text{data})P(\text{data}) = L(\text{data}|\text{model})P(\text{model}).$$

In this case, $L(\text{data}|\text{model})$ is just $L(R_\sigma)$. To get the probability of our model given the observed data, we assume both prior probabilities $P(\text{model})$ and $P(\text{data})$ are constant. So the probability of the model given data is normalized $L(R_\sigma)$.

There is a 95% chance that R_σ falls into $[0, R_\sigma^{(0.95)}]$, where $R_\sigma^{(0.95)}$ is defined by

$$0.95 = \frac{\int_0^{R_\sigma^{(0.95)}} L(R_\sigma)\mathrm{d}R_\sigma}{\int_0^{\infty} L(R_\sigma)\mathrm{d}R_\sigma},$$

So the ratio of cross sections for Z′ bosons relative to standard model Z bosons above $R_\sigma^{(0.95)}$ can be excluded with 95% Confidence Level (C.L.). The calculation is done by the RooStat MCMCCalculator [82], in which the integration is done by the Metropolis-Hastings algorithm that is a Markov-Chain Monte Carlo (MCMC) method.

The observed limit calculation is done by inputting the observed ${M_{\mu\mu}}^i$ values. The expected limit calculation is done by inputting ${M_{\mu\mu}}^i$ values from pseudoexperiments. Each pseudoexperiment is done with the following procedure.

1. Generate the background nuisance parameter θ_{bkg} according to its distribution;
2. Calculate $N_{\text{bkg}}^{\text{expected}}$: $N_{\text{bkg}}^{\text{expected}} = N_{M_{\mu\mu}>200\,\text{GeV}}^{\text{observed}} \times \theta_{\text{bkg}}$;
3. Generate the number of events in the pseudoexperiment (N^{pseudo}) distributed according to the Poisson law with a mean being $N_{\text{bkg}}^{\text{expected}}$;
4. Generate N^{pseudo} dimuon invariant masses (${M_{\mu\mu}}^i$, $i = 1, 2, \ldots, N^{\text{pesudo}}$) distributed according to $pdf_{\text{DY}}(M_{\mu\mu}; a_{\text{DY}}, b_{\text{DY}})$;

One $R_\sigma^{(0.95)}$ is calculated for each pseudoexperiment. The best estimate for the expected limit is taken to be the median of the set of $R_\sigma^{(0.95)}$s. The 68% (one times uncertainty) and 95% (two times uncertainty) quantile bands within the set of $R_\sigma^{(0.95)}$s are also evaluated.

4.7 Results at $\sqrt{s} = 7\,\text{TeV}$ with CMS 2011 data

The result shown in this chapter is based on the CMS data in 2011. The result with CMS 2012 data is shown in Appendix B. The summary of parameter values of 2011 and 2012 is shown in Appendix A.

4.7.1 The Systematic Uncertainties

The signal systematic uncertainties in the 2011 analysis can be summarized in the following table:

counts of Z	normalization to counts of Z	muon showering	total
2%	1.5%	2%	3.2%

Table 4.3: Signal uncertainty sources in the 2011 analysis according to Section 4.3. The components of the uncertainties are combined in quadrature.

The background systematic uncertainties at $M_{\mu\mu} = 400\,\text{GeV}$ and $1.5\,\text{TeV}$ in the 2011 analysis can be summarized as:

	at $M_{\mu\mu} = 400$ GeV	at $M_{\mu\mu} = 1.5$ TeV
PDF	4%	16%
NNLO QCD correction	0.7%	1.7%
$t\bar{t}$	13.6%	
Total	14.2%	21.1%

Table 4.4: Background uncertainty sources in the 2011 analysis according to Section 4.5 and Figure 2.4. The components of the uncertainties are combined in quadrature.

As a result, in the 2011 analysis, the total signal uncertainty is 3.2% and the background uncertainty is assigned as 20%. Those uncertainties are marginalized in the limit setting integration according to lognormal distributions.

4.7.2 Exclusion Limits

The top panel of Figure 4.12 shows the dimuon limit calculated by the method mentioned in the last section.

The limits based on the dielectron data set were done by the dielectron analysis group (see CMS internal note AN-2011-444 and [72]). They used a similar method with different probability distribution functions, as shown in the middle panel of Figure 4.12. Because the dielectron search requires the ECAL detector while the dimuon search can be performed without the calorimeters with little losses of accuracy, the amount of dielectron data, $4.98\,\text{fb}^{-1}$, is less than the dimuon data.

The combined dilepton result is created by combining the dimuon and dielectron data and combing the dimuon and dielectron models, as shown in the bottom panel of Figure 4.12. The predicted cross section ratio limits for Z'_{St} produced in the minimum

Stueckelberg extension to the standard model with $\epsilon = 0.02, 0.03, 0.04, 0.05$, and 0.06, as well as the predicted cross section ratios of sequential standard model Z′ with standard model couplings [83], the Z′$_\psi$ expected in grand unified theories [84], and the Kaluza-Klein graviton G_{kk} excitations arising in the Randall-Sundrum (RS) model of extra dimensions [85, 86] are shown[4].

From Figure 4.12, we get the Z'_{St} invariant mass limit in Table 4.5.

	expected (GeV)			observed (GeV)		
	$M_{\mu\mu}$	M_{ee}	$M_{\ell\ell}$, combined	$M_{\mu\mu}$	M_{ee}	$M_{\ell\ell}$, combined
Z'_{St}, $\epsilon = 0.04$	410	460	510	520	530	540
Z'_{St}, $\epsilon = 0.05$	560	620	700	540	560	740
Z'_{St}, $\epsilon = 0.06$	690	740	820	860	720	890

Table 4.5: 95% C.L lower mass limits for the Z'_{St}s with different ϵ_s [72]. Because the detector dimuon invariant mass resolution in this range is from 10 to 40 GeV and the dielectron invariant mass resolution is about 10 GeV, the numbers are rounded to 10 GeV.

The invariant mass limit is obtained by examining the cross point between the mid-line of the predicted cross section ratio bands and the expected/observed ratio limit. Conservatively, the lowest m_{res} cross point is chosen as the limit. The Z'_{St}, $\epsilon = 0.02$ and $\epsilon = 0.03$ limits are below 300 GeV with 2011 CMS data, which is out of this analysis scale.

[4]The predicted cross section is calculated from the product of the PYTHIA6.4 [77] leading order cross section and up to the next next leader order k-factor calculated from ZWPROD [32]. In the PYTHIA calculation, a mass window cut has been applied to the generator: $|M_{\ell\ell} - m_{res}|/m_{res} < 40\%$. This is to obtain the cross section when the decay width approaches zero (the cross section under the narrow width approximation) [87]. In the narrow width approximation, the vector boson propagator, $\lim_{\Gamma\to 0} \frac{1}{(p^2 - m_{res}^2)^2 + (m_{res}\Gamma)^2}$, reduces to $\frac{\pi}{m_{res}\Gamma}\delta(p^2 - m_{res}^2)$. It removes all off-shell events and assumes that all resonance events happen on-shell. This approximation makes it possible to set the dilepton cross section limit in a model independent fashion. In [72], we set the limit based on the decay width of the sequential standard model Z′ with standard model couplings, as shown in Equation 4.12. It does not match the narrow width approach. In the 2012 data analysis, the group used the decay width of the Z′$_\psi$, which is insensitive to the mass cut [87] and obeys the narrow width approach. In Appendix B, I use the decay width of the Z'_{St}. The decay width of the Z'_{St} is tiny enough compared to the dimuon mass resolution. For the 2011 analysis, I will further discuss this issue in Section 4.7.3.

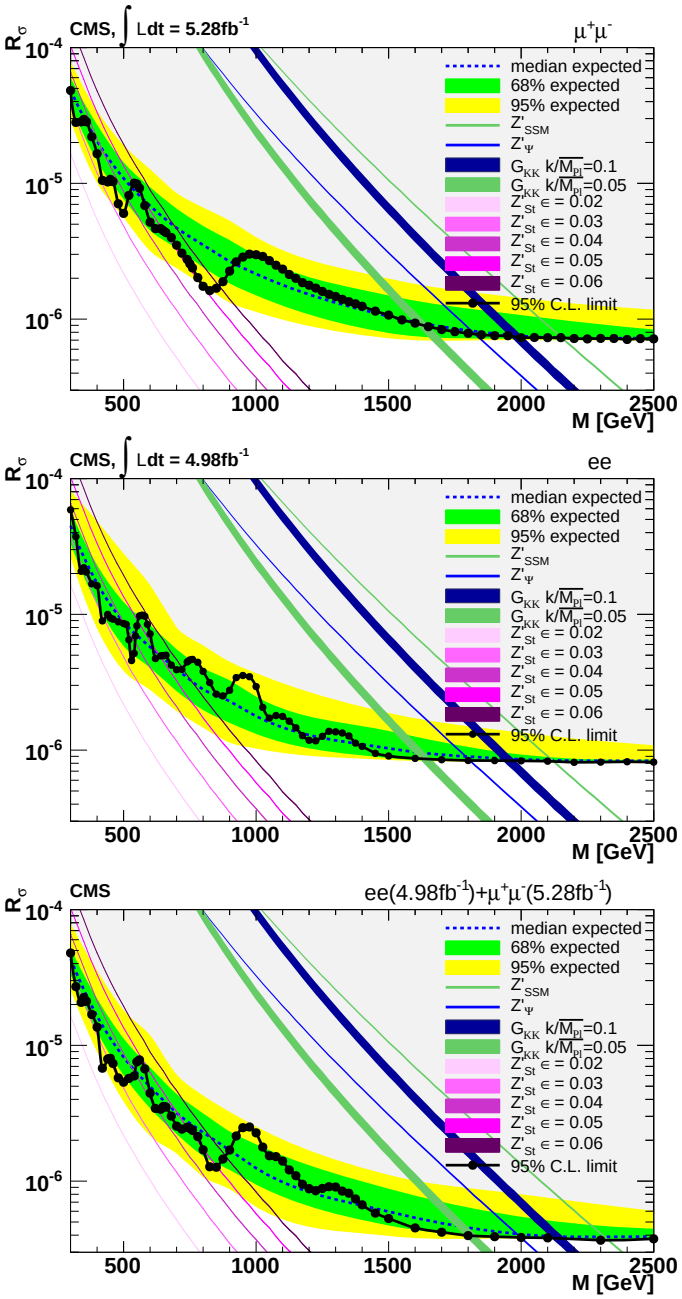

Figure 4.12: Ratio R_σ upper limits ($R_\sigma^{(0.95)}$) as a function of the dilepton resonance mass $m_{\rm res}$ [72]. The limits are shown from (top) the $\mu^+\mu-$ final state, (middle) the e^+e^- final state and (bottom) the combined $\ell^+\ell^-$ result. Shaded green and yellow bands correspond to the 68% and 95% quantiles for the expected limits. The predicted QCD NNLO cross section ratios of sequential standard model Z′, Z'_ψ, $\mathrm{Z}'_{\rm St}$, and G_{kk} are shown as bands, with widths indicating the QCD NNLO k-factor uncertainties.

4.7.3 The Effect of Narrow Width Approximation and Dimuon Mass Resolution

As mentioned after Equation 4.12 and in the footnote 4, the narrow width approximation only needs to take the dimuon mass resolution but not the decay width into account. Table 4.6 shows the observed 95% C.L. lower mass limit using the decay width of Z'_{St} and dimuon data. The decay width of the Z'_{St} is tiny enough comparing with the dimuon mass resolution. In this case, the uncertainty of the dimuon mass resolution will propagate to the lower mass limits. The propagation of the uncertainty of the dimuon mass resolution is studied by taking the upper and lower edges of the parameters in Equation 4.4. According to the uncertainties given in Figure 4.5, the upper and lower edges of those parameters are

$$\begin{aligned} p_0 &= 0.003302 \text{ and } 0.015362, \\ p_1 &= 4.60 \times 10^{-5} \text{ and } 6.821 \times 10^{-5}\,\text{GeV}^{-1} \\ p_2 &= -5.911 \times 10^{-9} \text{ and } 3.569 \times 10^{-9}\,\text{GeV}^{-2}. \end{aligned}$$

The results are shown in Table 4.6.

	with $\Gamma_{\text{sequential SM Z}'}$	with $\Gamma_{Z'_{St}}$	lower edge	upper edge
Z'_{St}, $\epsilon = 0.03$	N/A	450	520	N/A
Z'_{St}, $\epsilon = 0.04$	540	530	540	520
Z'_{St}, $\epsilon = 0.05$	560	860	880	840
Z'_{St}, $\epsilon = 0.06$	860	890	900	870

Table 4.6: The observed 95% C.L lower dimuon invariant mass limits for the Z'_{St} with different expected peak widths. From the second to the last column: using the decay width of the sequential standard model Z' (same with the fifth column in Table 4.5 as comparison), using the decay width of the Z'_{St}, using the decay width of the Z'_{St} and the lower edge (best expectation) of the dimuon mass resolution, and using the decay width of the Z'_{St} and the upper edge (worst expectation) of the dimuon mass resolution. The limit of Z'_{St} with $\epsilon = 0.05$ jumps a lot because there is a peak around 550 GeV at the observed limit line, as shown in the top panel of Figure 4.12. The existence of a signal at that invariant mass can not be excluded due to the large total expected peak width. As the entire observed limit line getting lower due to the shrink of the total peak width, this peak no longer affects the Z'_{St} with $\epsilon = 0.05$.

As a result, due to the uncertainty of the dimuon mass resolution, the uncertainty of the observed 95% C.L. lower mass limit is in general 20 GeV.

4.7.4 The (C_d, C_u) and $(M_{\mathrm{Z'_{St}}}, \epsilon)$ Limit of the Stueckelberg Z′

In this section, the 95% C.L. excluded region in $(M_{\mathrm{Z'_{St}}}, \epsilon)$ parameter space is determined based on the combined CMS 2011 dilepton data. The 95% C.L. excluded region of the coupling constants of the $\mathrm{Z'_{St}}$ with up and down type quarks, introduced in section 2.9.3, correlating with $(M_{\mathrm{Z'_{St}}}, \epsilon)$, has also been determined.

As indicated by Equation 2.16, upon setting a cross section limit for a certain m_{res}, the allowed (C_d, C_u) values should satisfy:

$$C_u W_u(s, M^2_{\mathrm{Z'_{St}}}) + C_d W_d(s, M^2_{\mathrm{Z'_{St}}}) < \frac{48s}{\pi}\sigma(pp \to \mathrm{Z'} + X \to \ell^+\ell^- + X)^{(0.95)}, \quad (4.16)$$

where the (0.95) indicates the 95% C.L. upper limit. For each resonance mass $M_{\mathrm{Z'_{St}}}$, the excluded (C_d, C_u) regions are thus described in Figure 4.13.

To get a clear view, as done in Figure 2.5, the coordinate of (C_d, C_u) is rotated by 0.295 rad counterclockwise. For each $M_{\mathrm{Z'_{St}}}$, the excluded part of ϵ has been examined individually, as shown in Figure 4.14.

Combining the plots in Figure 4.14, Figure 4.15 summarizes the allowed and 95% C.L. excluded region in the (C_d, C_u) and $(M_{\mathrm{Z'_{St}}}, \epsilon)$ parameter spaces.

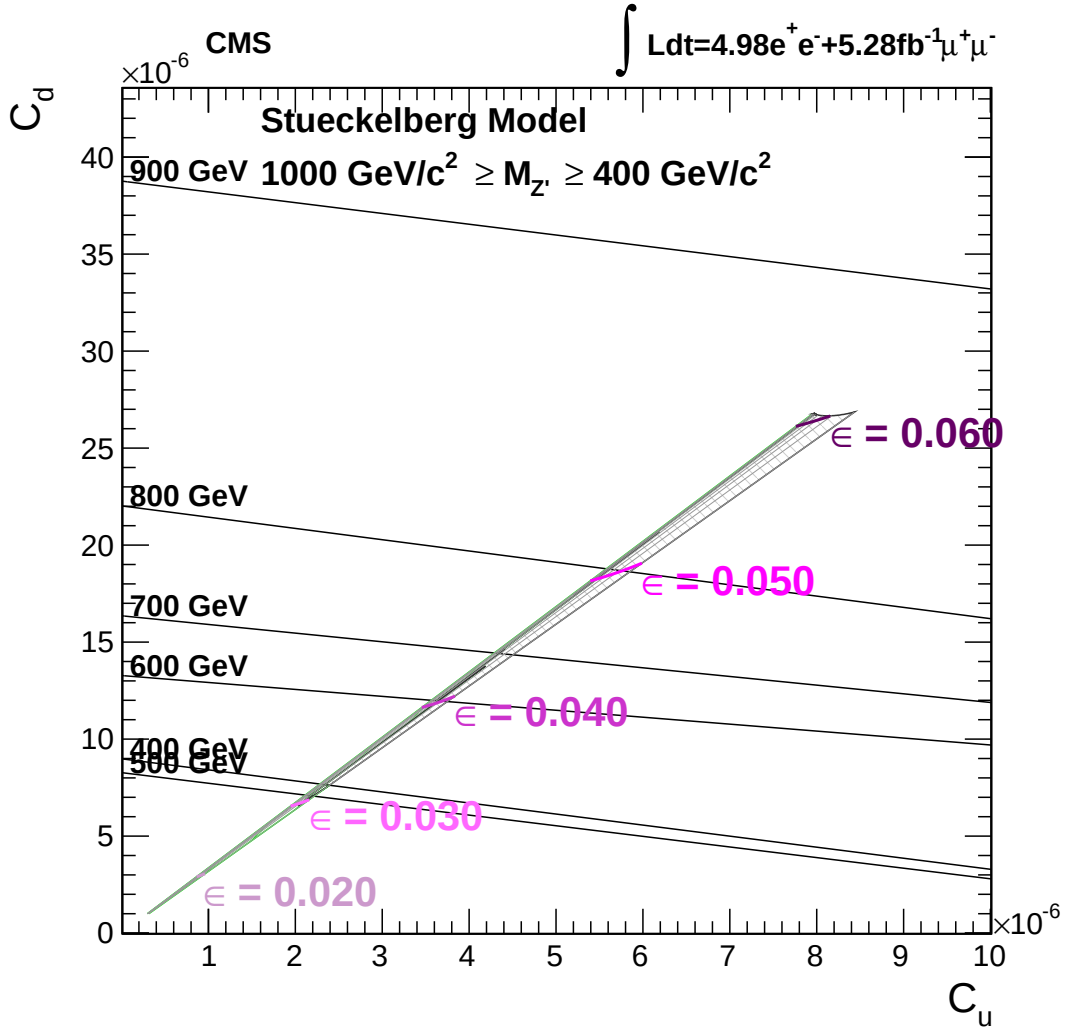

Figure 4.13: The 95% C.L. upper limits on the Z′ cross sections for given masses are equivalent to excluded regions in the (C_d, C_u) plane that are bounded by the thin black lines in the figure. For each $M_{Z'_{St}}$, the region above the corresponding black line is excluded at 95% C.L..

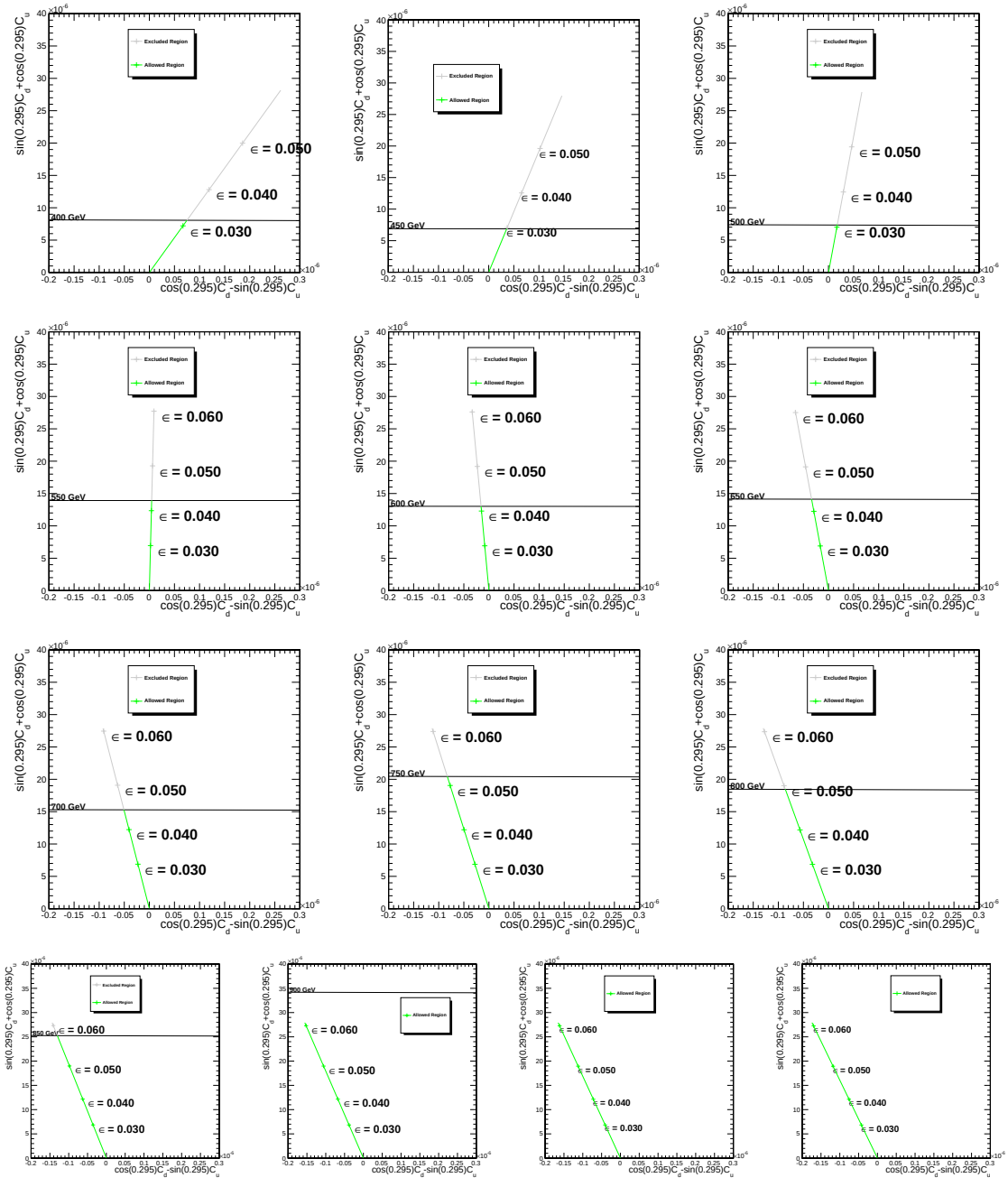

Figure 4.14: The 95% C.L. upper limit of ϵ for each given $M_{Z'_{St}}$, where $M_{Z'_{St}} = 400, 450, 500, 550, 600, 650, 700, 750, 800, 850, 900, 950, 1000\,\text{GeV}$ horizontally from top-left to bottom-right.

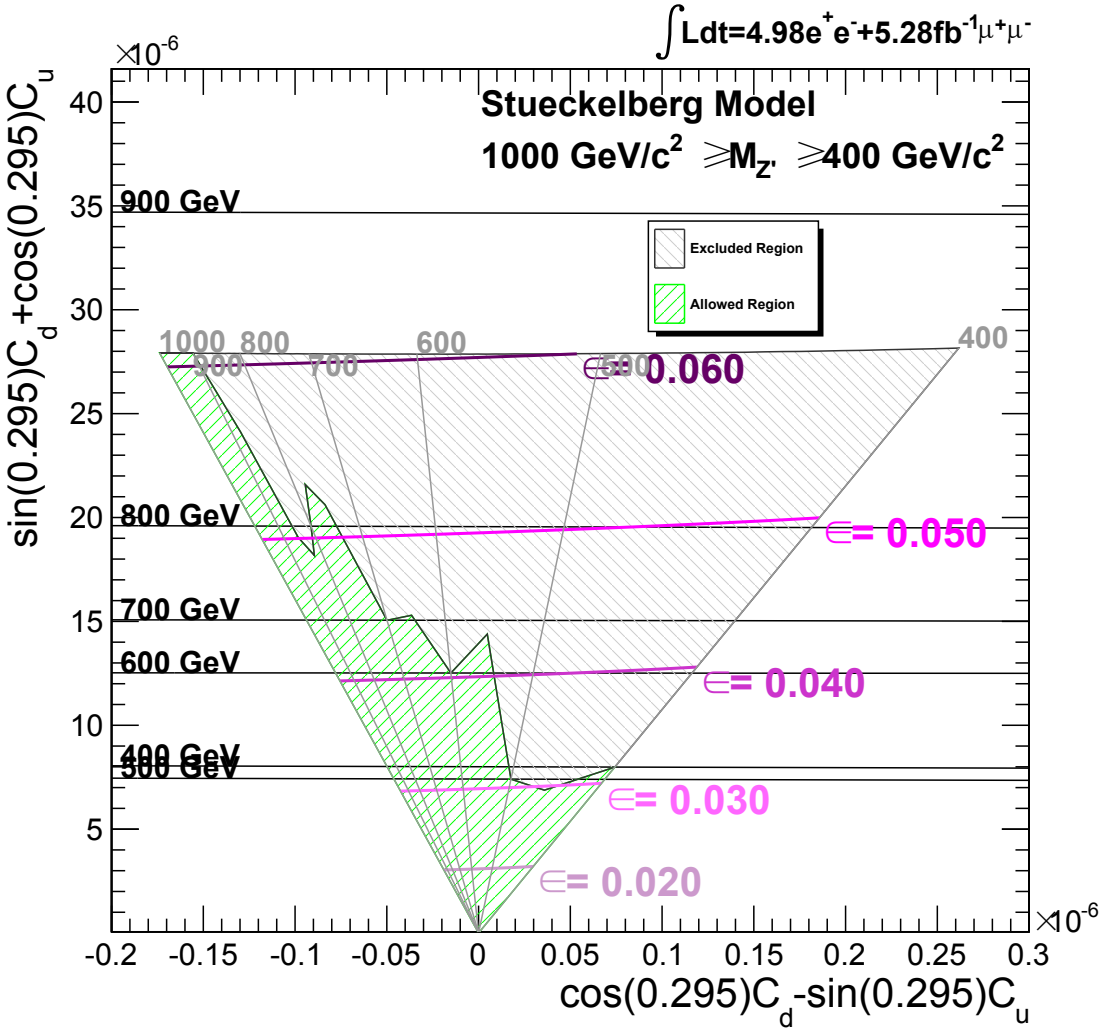

Figure 4.15: The 95% C.L. excluded regions on the rotated (C_d, C_u) plane. The black lines are the border lines of the 95% C.L. excluded regions. The gray lines are the iso-$M_{Z'_{St}}$-lines. The magenta lines are the iso-ϵ-lines.

Chapter 5

Conclusion

The theory of the Standard Model, the extension to the SM via the Stueckelberg model, and the CMS detector have been introduced. The search for Z′ decaying into dimuon pairs using $\sqrt{s} = 7\,\text{TeV}$ pp collision data collected by CMS in 2011 has been presented. The integrated luminosity corresponds to $5.3\,\text{fb}^{-1}$. Combining with the dieletron search with $5.0\,\text{fb}^{-1}$ of integrated luminosity, the observed result shows that for the model parameter values $\epsilon = 0.06\,(0.05, 0.04)$, Stueckelberg Z′s with masses smaller than $890\,(790, 540)\,\text{GeV}$ are excluded at 95% confidence level. In addition, the upper limit is presented in terms of the Z'_{St} couplings to up and down quark (C_u and C_d), in which the 95% C.L. excluded parameter region is shown.

References

[1] **CMS** Collaboration, *The CMS Physics Technical Design Report, volume 1*, tech. rep., Feb, 2006. CMS TDR 8.1.

[2] M. Lapka, *Interactive Slice of the CMS detector*, 2012. Available at `https://cms-docdb.cern.ch/cgi-bin/PublicDocDB/RetrieveFile?docid=4172&version=2&filename=CMS_Slice.gif`.

[3] S. Weinberg, *Recent progress in gauge theories of the weak, electromagnetic and strong interactions*, *Rev. Mod. Phys.* **46** (Apr, 1974) 255–277.

[4] F. Hasert *et al.*, *Search for elastic muon-neutrino electron scattering*, *Physics Letters B* **46** (1973), no. 1 121 – 124.

[5] F. Hasert *et al.*, *Observation of neutrino-like interactions without muon or electron in the gargamelle neutrino experiment*, *Physics Letters B* **46** (1973), no. 1 138 – 140.

[6] F. Hasert *et al.*, *Observation of neutrino-like interactions without muon or electron in the gargamelle neutrino experiment*, *Nuclear Physics B* **73** (1974), no. 1 1 – 22.

[7] B. Wiik, *First Results from PETRA*, *Conf.Proc.* **C7906181** (1979) 113–154.

[8] G. Arnison *et al.*, *Experimental observation of isolated large transverse energy electrons with associated missing energy at* $\sqrt{s} = 540$ *gev*, *Physics Letters B* **122** (1983), no. 1 103 – 116.

[9] P. Bagnaia *et al.*, *Evidence for* $z^0 \to e^+e^-$ *at the CERN pp collider*, *Physics Letters B* **129** (1983), no. 12 130 – 140.

[10] **CMS** Collaboration, *Observation of a new boson with mass near 125 GeV in pp collisions at* $\sqrt{s} = 7$ *and 8 TeV*, *Journal of High Energy Physics* **2013** (2013), no. 6 1–127.

[11] **ATLAS** Collaboration, *Evidence for the spin-0 nature of the higgs boson using ATLAS data*, *Physics Letters B* **726** (2013), no. 13 120 – 144.

[12] **CMS** Collaboration, *CMS Luminosity Based on Pixel Cluster Counting - Summer 2013 Update*, Tech. Rep. CMS-PAS-LUM-13-001, CERN, Geneva, 2013.

[13] S. Weinberg, *The Quantum theory of fields. Vol. 1: Foundations*. 1995.

[14] M. E. Peskin and D. V. Schroeder, *An Introduction to Quantum Field Theory*. Addison-Wesley Publishing Company, 1995.

[15] E. Noether, *Invariant Variation Problems*, *Gott.Nachr.* **1918** (1918) 235–257 [physics/0503066].

[16] M. Srednicki, *Quantum field theory*. 2007.

[17] D. J. Gross and F. Wilczek, *Ultraviolet behavior of non-abelian gauge theories*, *Phys. Rev. Lett.* **30** (Jun, 1973) 1343–1346.

[18] E. Fermi, *Versuch einer theorie der β-strahlen. i*, *Zeitschrift für Physik* **88** (1934), no. 3-4 161–177.

[19] T. D. Lee and C. N. Yang, *Question of parity conservation in weak interactions*, *Phys. Rev.* **104** (Oct, 1956) 254–258.

[20] C. S. Wu, E. Ambler, R. W. Hayward, D. D. Hoppes and R. P. Hudson, *Experimental test of parity conservation in beta decay*, *Phys. Rev.* **105** (Feb, 1957) 1413–1415.

[21] **Particle Data Group** Collaboration, J. Beringer *et al.*, *Review of Particle Physics (RPP)*, *Phys.Rev.* **D86** (2012) 010001.

[22] S. Weinberg, *The Quantum theory of fields. Vol. 2: Modern Applications*. 1995.

[23] L.-L. Chau and W.-Y. Keung, *Comments on the parametrization of the kobayashi-maskawa matrix*, *Phys. Rev. Lett.* **53** (Nov, 1984) 1802–1805.

[24] http://en.wikipedia.org/wiki/Cabibbo-Kobayashi-Maskawa_matrix.

[25] B. Körs and P. Nath, *A Stueckelberg extension of the standard model*, *Phys. Lett.* **B586** (2004) 366–372 [hep-ph/0402047].

[26] B. Körs and P. Nath, *Aspects of the Stueckelberg extension*, *JHEP* **07** (2005) 069 [hep-ph/0503208].

[27] F. A. Dilkes and D. G. C. McKeon, *Massive renormalizable abelian gauge theory in 2+1 dimensions*, *Phys. Rev. D* **52** (Oct, 1995) 4668–4674.

[28] D. Feldman, Z. Liu and P. Nath, *The Stueckelberg Z Prime at the LHC: Discovery Potential, Signature Spaces and Model Discrimination*, *JHEP* **11** (2006) 007 [hep-ph/0606294].

[29] H. Lehmann, K. Symanzik and W. Zimmermann, *Zur formulierung quantisierter feldtheorien*, *Il Nuovo Cimento* **1** (1955), no. 1 205–225.

[30] F. Halzen and A. D. Martin, *Quarks and Leptons*. John Wiley & Sons, 1984.

[31] J. Pumplin *et al.*, *New generation of parton distributions with uncertainties from global QCD analysis*, *JHEP* **0207** (2002) 012 [hep-ph/0201195].

[32] R. Hamberg, T. Matsuura and W. van Neerven, *ZWPROD program*, 1989-2002. Available at http://www.lorentz.leidenuniv.nl/research/neerven/DECEASED/Welcome.html.

[33] R. Hamberg, W. L. van Neerven and T. Matsuura, *A complete calculation of the order α_s^2 correction to the Drell-Yan K-factor* , *Nuclear Physics B* **359** (1991) 343–405.

[34] W. van Neerven and E. Zijlstra, *The $O(\alpha_s^2)$ corrected Drell-Yan K-factor in the DIS and $\overline{MS}$ schemes* , *Nuclear Physics B* **382** (1992), no. 1 11 – 62.

[35] M. Carena, A. Daleo, B. A. Dobrescu and T. M. P. Tait, *z' gauge bosons at the fermilab tevatron*, *Phys. Rev. D* **70** (Nov, 2004) 093009.

[36] **CMS** Collaboration, *The CMS experiment at the CERN LHC*, *Journal of Instrumentation* **3** (2008), no. 08 S08004.

[37] **ATLAS** Collaboration, *The ATLAS Experiment at the CERN Large Hadron Collider*, *Journal of Instrumentation* **3** (2008), no. 08 S08003.

[38] **ALICE** Collaboration, *The ALICE experiment at the CERN LHC*, *Journal of Instrumentation* **3** (2008), no. 08 S08002.

[39] J. L. Pinfold, *Searching for the magnetic monopole and other highly ionizing particles at accelerators using nuclear track detectors*, *Radiation Measurements* **44** (2009), no. 90 834 – 839. Proceedings of the 24th International Conferenceon Nuclear Tracks in Solids.

[40] **TOTEM** Collaboration, G. Anelli *et al.*, *The TOTEM Experiment at the CERN Large Hadron Collider*, *Journal of Instrumentation* **3** (2008), no. 08 S08007.

[41] **LHCb** Collaboration, *The LHCb Detector at the LHC*, *Journal of Instrumentation* **3** (2008), no. 08 S08005.

[42] **LHCf** Collaboration, O. Adriani *et al.*, *The LHCf detector at the CERN Large Hadron Collider*, *Journal of Instrumentation* **3** (2008), no. 08 S08006.

[43] **CMS** Collaboration, G. Acquistapace *et al.*, *CMS, the magnet project: Technical design report*, . CERN-LHCC-97-10 [`http://cmsdoc.cern.ch/ftp/TDR/MAGNET/magnet.html`].

[44] **CMS** Collaboration, *Precise mapping of the magnetic field in the cms barrel yoke using cosmic rays*, *Journal of Instrumentation* **5** (2010), no. 03 T03021.

[45] **CMS** Collaboration, S. Chatrchyan *et al.*, *The CMS experiment at the CERN LHC*, *JINST* **3** (2008) S08004.

[46] **CMS** Collaboration, *The CMS tracker system project : Technical Design Report*, tech. rep., Geneva, 1997. CERN-LHCC-98-006.

[47] L. Borrello, A. Messineo, E. Focardi and A. Macchiolo, *Sensor Design for the CMS Silicon Strip Tracker*, Tech. Rep. CMS-NOTE-2003-020, CERN, Geneva, Aug, 2003.

[48] P. Schleper, G. Steinbrüeck and M. Stoye, *Software Alignment of the CMS Tracker using MILLEPEDE II*, Tech. Rep. CMS-NOTE-2006-011, CERN, Geneva, Jan, 2006.

[49] E. Widl, R. Frühwirth and W. Adam, *A Kalman Filter for Track-based Alignment*, Tech. Rep. CMS-NOTE-2006-022, CERN, Geneva, Jan, 2006.

[50] V. Karimäki, A. M. Heikkinen, T. Lampén and T. Lindén, *Sensor Alignment by Tracks*, Tech. Rep. CMS-CR-2003-022. physics/0306034, CERN, Geneva, Jun, 2003.

[51] W. Leo, *Techniques for Nuclear and Particle Physics Experiments: A How to Approach*. Springer-Verlag, 2nd ed., 1994.

[52] A. Annenkov, M. Korzhik and P. Lecoq, *Lead tungstate scintillation material*, *Nuclear Instruments and Methods in Physics Research Section A: Accelerators, Spectrometers, Detectors and Associated Equipment* **490** (2002), no. 1C2 30 – 50.

[53] I. Dafinei, E. Auffray, P. Lecoq and M. Schneegans, *Lead tungstate for high energy calorimetry*, in *Symposium P C Scintillator and Phosphor Materials*, vol. 348 of *MRS Proceedings*, 1, 1994.

[54] P. Adzic, *Energy resolution of the barrel of the cms electromagnetic calorimeter*, *Journal of Instrumentation* **2** (2007), no. 04 P04004.

[55] **CMS** Collaboration, *The Electromagnetic Calorimeter: Technical Design Report*, tech. rep., Geneva, 1997. CERN-LHCC-97-033.

[56] P. Aspell *et al.*, *Results from the 1999 Beam Test of a Preshower Prototype*, Tech. Rep. CMS-NOTE-2000-001, CERN, Geneva, Jan, 2000.

[57] D. Green, *Calibration of the CMS Calorimeters*, tech. rep., May, 2001.

[58] **CMS Collaboration** Collaboration, S. Chatrchyan *et al.*, *The performance of the CMS muon detector in proton-proton collisions at sqrt(s) = 7 TeV at the LHC*, *JINST* **8** (2013) P11002 [1306.6905].

[59] **CMS** Collaboration, S. Chatrchyan *et al.*, *Performance of the CMS Drift Tube Chambers with Cosmic Rays*, *JINST* **5** (2010) T03015 [0911.4855].

[60] **CMS** Collaboration, *The CMS muon project: Technical Design Report*, tech. rep., Geneva, 1997. CERN-LHCC-97-032.

[61] R. Fruhwirth, *Application of Kalman filtering to track and vertex fitting*, *Nucl.Instrum.Meth.* **A262** (1987) 444–450.

[62] R. Fruhwirth and T. Speer, *A Gaussian-sum filter for vertex reconstruction*, *Nucl.Instrum.Meth.* **A534** (2004) 217–221.

[63] M. Cacciari, G. P. Salam and G. Soyez, *The Anti-k_t jet clustering algorithm*, *JHEP* **0804** (2008) 063 [0802.1189].

[64] J. D'Hondt, P. Vanlaer, R. Fruhwirth and W. Waltenberger, *Sensitivity of robust vertex fitting algorithms*, *IEEE Trans.Nucl.Sci.* **51** (2004) 2037–2044.

[65] R. Fruhwirth, W. Waltenberger, K. Prokofiev, T. Speer and P. Vanlaer, *New developments in vertex reconstruction for CMS*, *Nucl.Instrum.Meth.* **A502** (2003) 699–701.

[66] T. Speer, K. Prokofiev, R. Fruhwirth, W. Waltenberger and P. Vanlaer, *Vertex fitting in the CMS tracker*, .

[67] **CMS** Collaboration, *Particle-Flow Event Reconstruction in CMS and Performance for Jets, Taus, and MET*, Tech. Rep. CMS-PAS-PFT-09-001, CERN, 2009. Geneva, Apr, 2009.

[68] A. Strandlie and W. Wittek, *Propagation of Covariance Matrices of Track Parameters in Homogeneous Magnetic Fields in CMS*, Tech. Rep. CMS-NOTE-2006-001, CERN, Geneva, Jan, 2006.

[69] S. Agostinelli *et al.*, *Geant4a simulation toolkit*, *Nuclear Instruments and Methods in Physics Research Section A: Accelerators, Spectrometers, Detectors and Associated Equipment* **506** (2003), no. 3 250 – 303.

[70] J. Allison *et al.*, *Geant4 developments and applications*, *Nuclear Science, IEEE Transactions on* **53** (Feb, 2006) 270–278.

[71] **CMS Collaboration** Collaboration, S. Chatrchyan *et al.*, *Identification of b-quark jets with the CMS experiment*, *JINST* **8** (2013) P04013 [1211.4462].

[72] **CMS** Collaboration, *Search for narrow resonances in dilepton mass spectra in pp collisions at $\sqrt{s} = 7$ TeV*, *Physics Letters B* **714** (2012), no. 2 158 – 179.

[73] **CMS** Collaboration, *CMS tracking performance results from early LHC operation*, *The European Physical Journal C* **70** (2010), no. 4 1165–1192.

[74] **CMS** Collaboration, *Performance of CMS muon reconstruction in pp collision events at $\sqrt{s} = 7$ TeV*, *Journal of Instrumentation* **7** (2012), no. 10 P10002.

[75] **CMS** Collaboration, S. Chatrchyan *et al.*, *Measurement of the Inclusive W and Z Production Cross Sections in pp Collisions at $\sqrt{s} = 7$ TeV*, *JHEP* **1110** (2011) 132 [1107.4789].

[76] D. E. Groom, N. V. Mokhov and S. I. Striganov, *Muon stopping power and range tables 10-MeV to 100-TeV*, *Atom.Data Nucl.Data Tabl.* **78** (2001) 183–356.

[77] T. Sjostrand, S. Mrenna and P. Z. Skands, *PYTHIA 6.4 Physics and Manual*, *JHEP* **05** (2006) 026 [hep-ph/0603175].

[78] M. Whalley, D. Bourilkov and R. Group, *The Les Houches accord PDFs (LHAPDF) and LHAGLUE*, hep-ph/0508110.

[79] D. Bourilkov, *Study of parton density function uncertainties with LHAPDF and PYTHIA at LHC*, hep-ph/0305126.

[80] S. Frixione and B. R. Webber, *Matching NLO QCD computations and parton shower simulations*, *Journal of High Energy Physics* **2002** (2002), no. 06 029.

[81] **CMS** Collaboration, S. Chatrchyan *et al.*, *Search for Resonances in the Dilepton Mass Distribution in pp Collisions at* $\sqrt{s} = 7$ *TeV*, *JHEP* **1105** (2011) 093 [1103.0981].

[82] **RooStats Team** Collaboration, G. Schott, *RooStats for Searches*, 1203.1547.

[83] G. Altarelli, B. Mele and M. Ruiz-Altaba, *Searching for New Heavy Vector Bosons in* $p\bar{p}$ *Colliders*, *Z.Phys.* **C45** (1989) 109.

[84] A. Leike, *The Phenomenology of extra neutral gauge bosons*, *Phys.Rept.* **317** (1999) 143–250 [hep-ph/9805494].

[85] L. Randall and R. Sundrum, *An alternative to compactification*, *Phys. Rev. Lett.* **83** (Dec, 1999) 4690–4693.

[86] L. Randall and R. Sundrum, *Large mass hierarchy from a small extra dimension*, *Phys. Rev. Lett.* **83** (Oct, 1999) 3370–3373.

[87] E. Accomando, A. Belyaev, L. Fedeli, S. F. King and C. Shepherd-Themistocleous, *Z' physics with early LHC data*, *Phys.Rev.* **D83** (2011) 075012 [1010.6058].

Appendix A

Parameters at $\sqrt{s} = 7$ TeV 2011 CMS Data and at $\sqrt{s} = 8$ TeV 2012 CMS Data

Parameters Used in the Unbinned Likelihood

The parameters used in the analytic model and unbinned likelihood limit setting for the 2011 and 2012 data are listed in Table A.2. The changes in the 2012 analysis are

a Expected decay width: As mentioned in the footnote in section 4.7.2, for the 2011 analysis, the decay width of the sequential standard model Z′ with standard model couplings was used; in 2012, the decay width of Z'_{St} was used.

b The prescale trigger used to count the standard model Z: In the 2011 analysis, the number of standard model Z is counted using a prescaled single muon trigger with online calculated p_T threshold at 15 GeV and $|\eta| < 2.1$, corresponding to offline reconstructed $p_T = 20$ GeV and $|\eta| < 2.1$. The normalized overall prescale factor is 2000. In the 2012 analysis, similar adjustment is done. The online reconstructed p_T threshold of the trigger is 24 GeV, corresponding to offline reconstructed p_T= 27 GeV. The pseudorapidity range is still $|\eta| < 2.1$. The overall prescale factor is 300.

c Fit to the background: As mentioned in Section 4.6.1, in the 2011 analysis, the Drell–Yan shape with the pdf fit, Equation 4.5, has been used. In the 2012 analysis, the fit with the total background (Equation 4.13) has been applied.

d Systematic uncertainty:

For the signal uncertainty, in the 2011 analysis, Equation 4.3 is used. In the 2012 analysis, the same signal systematic uncertainty is taken into account, about 1% at $M_{\mu\mu} = 1$ TeV and about 3.5% at $M_{\mu\mu} = 3$ TeV. A 3% signal systematic uncertainty is used in both the 2011 and 2012 analyses.

For the background uncertainty in the 2011 analysis, Equation 4.6 is used. In 2012 analysis, since the fitting scheme is changed, as mentioned above in c, the background uncertainty comes from

- the uncertainty in the mass resolution,
- the mass scale factor between the dimuon invariant mass peak from the data reconstruction and that from the Monte-Carlo,
- the parton distribution function (PDF) uncertainty,
- the uncertainty in the higher order electroweak (EWK) correction,
- and the uncertainty in the higher order quantum chromodynamics (QCD) correction.

The following table lists them at $M_{\mu\mu} = 1$ TeV and $M_{\mu\mu} = 3$ TeV.

	at $M_{\mu\mu} = 1$ TeV	at $M_{\mu\mu} = 3$ TeV
mass resolution	0.6%	10%
mass scale	5%	15%
PDF	7%	30%
EWK correction	3.2%	12%
QCD correction	$2 \sim 3\%$ (neglected)	
Total	9%	37%

Table A.1: Background uncertainty sources in the 2012 analysis. The components of the uncertainties are combined in quadrature.

As a result, a 20% background uncertainty is still good for 2012 analysis and has been used.

The limit setting of the dependence of the background uncertainty has also been studied. Because of the marginalized nuisance parameters, changing the background uncertainty to up to 200% does not even affect the limits.

Monitoring Parameters

This section lists the experimental parameters that were not used in the likelihood method but were used for monitoring.

	Symbol	2011 7 TeV	2012 8 TeV
Dimuon invariant mass resolution (Equation 4.4)	p_0	0.009332	0.01675
	p_1	5.71×10^{-5}	2.575×10^{-5}
	p_2	-1.171×10^{-9}	-2.862×10^{-10}
Total dimuon acceptance×efficiency (Equation 4.2)	a_ϵ	0.849	0.81
	b_ϵ	-1.22×10^8	-1.54×10^8
	c_ϵ	510	585
Expected decay width [a]	$\Gamma(m_{\text{res}})$	$-1.30 + 0.031 m_{\text{res}}$	$0.00006 m_{\text{res}}$
Number of Zin the investigating luminosity (see Equation 4.7)	N_{Z}	680	24306
	ω_{pre} [b]	2000	300
	ϵ_{Z}	0.27	0.326
Number of observed $M_{\mu\mu} > 200$ GeV events	$N^{\text{observed}}_{M_{\mu\mu}>200\text{GeV}}$	4250	19950
Background shape [c] (Equation 4.5, 4.13)	$a_{\text{DY/bkg}}$	-0.002423	-0.002293
	$b_{\text{DY/bkg}}$	-3.625	-3.646
	c_{bkg}	0	3.315×10^{-8}
Systematic uncertainty [d]	Δ_{sig}	3%	3%
	Δ_{bkg}	20%	20%

Table A.2: Parameters used in the analytic model and unbinned likelihood limit setting. Unless specified, the definitions of the parameters are the same in the 2011 and 2012 analysis. Notes of changes in the 2012 analysis, **a** to **c**, are given in the text.

Table A.3 shows the number of simulated background events with $M_{\mu\mu} > 200$ GeV.

	2011 7 TeV	2012 8 TeV
DY	3591 ± 170	16274 ± 750
$t\bar{t}$	477 ± 72	2780 ± 160
Other prompt leptons ($t\bar{t}$-like events*)	190 ± 8	1034 ± 50
Multi-jets and W+jets	8 ± 4	$50 \pm 8^{**}$
Total background	4266 ± 185	20138 ± 920

Table A.3: Number of simulated background events in $M_{\mu\mu} > 200$ GeV (from the CMS internal notes AN-2011-472 and AN-2012-422). Uncertainties include both statistical and systematic components added in quadrature.
$*$ These include $Z \to \tau\tau$, WW, WZ, ZZ, and the single-top tW and $\bar{t}W$ events.
$**$ Only this number is evaluated from data as described in Section 4.5.3.

Table A.4 shows the number of background events evaluated from a data-driven analysis, compared with the simulation, as described in Sections 4.5.2, 4.5.3, and 4.5.4, with $M_{\mu\mu} > 200$ GeV.

	7 TeV Predicted	7 TeV Sim	8 TeV Predicted	8 TeV Sim
$t\bar{t}$ and other prompt leptons*	580 ± 25	667 ± 72	3330 ± 59	3814 ± 168
Multi-jets and W+jets	3 ± 0.2	8 ± 4	50 ± 8	N/A
Cosmic events	< 0.19	N/A	$< 0.09^{**}$	N/A

Table A.4: Number of background events evaluated from data compared with the simulation for $M_{\mu\mu} > 200$ GeV (from the CMS internal notes AN-2011-472 and AN-2012-422). Uncertainties include both statistical and systematic components added in quadrature.
$*$ These include $Z \to \tau\tau$, WW, WZ, ZZ, and the single-top tW and $\bar{t}W$ events.
$**$ The reduction in the number of recorded cosmic events in the 2012 analysis is due to better timing in the 2012 data taking period.

Appendix B

Results at $\sqrt{s} = 8$ TeV with CMS 2011 data

B.1 Dimuon Spectrum

The observed invariant mass spectrum of dimuons under $20.6\,\mathrm{fb}^{-1}$ is compared with the background predictions in Figure B.1. Different with the jets simulation in Figure 4.6 for the 2011 analysis, the jets background is estimated from data using the method mentioned in section 4.5.3.

B.2 $\mathrm{Z}'_{\mathrm{St}}$ Ratio Limit Based on CMS 2012 Dimuon Data

The 95% C.L. R_σ upper limits ($R_\sigma^{(0.95)}$) as a function of the dimuon resonance mass m_{res} is shown in the following plot. The result is based on the CMS 2012 dimuon data and the parameters mention in Appendix A.

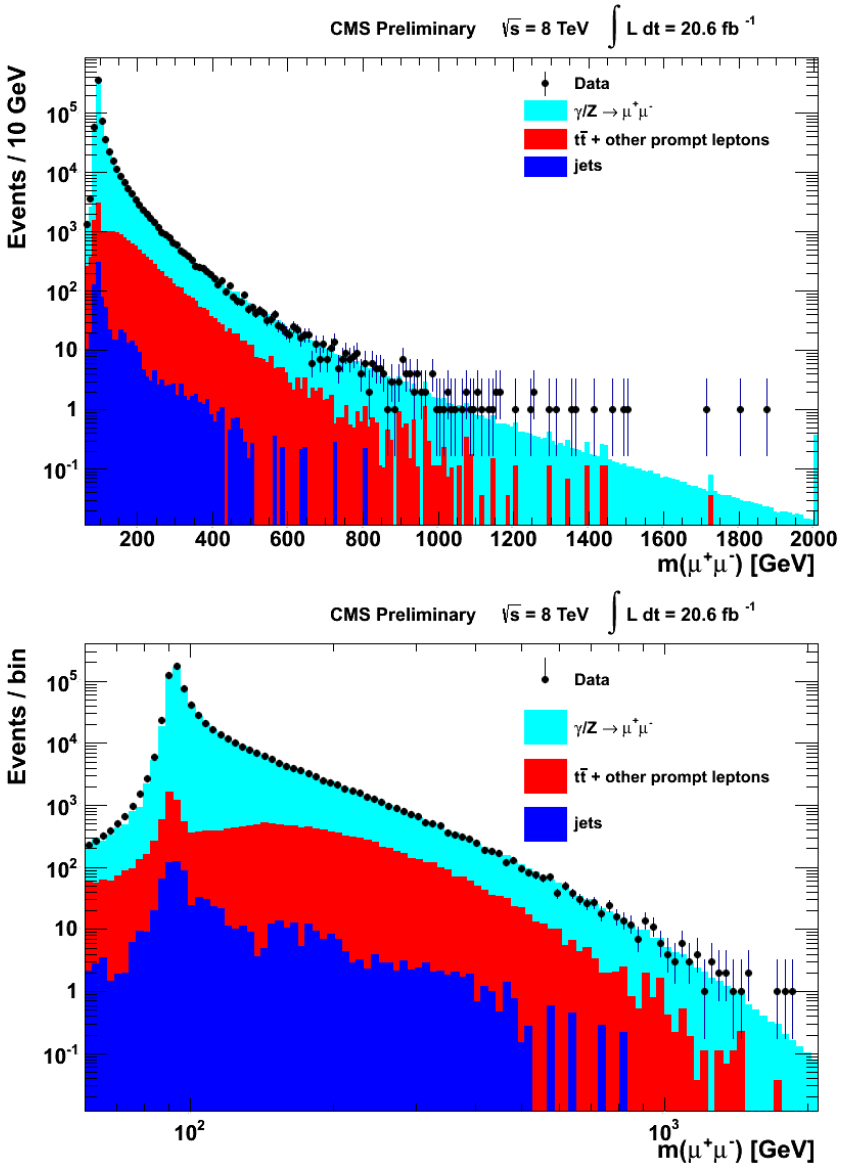

Figure B.1: The observed invariant mass spectrum of dimuons under 20.6 fb^{-1}, overlaid on the background prediction (with not log-scaled horizontal axis and log-scaled log-scaled horizontal axis, from CMS internal note AN-2012-422). Background simulations, $\mathrm{t\bar{t}}$, W^+W^-, WZ, ZZ, tW, $\bar{\mathrm{t}}$W, and $\mathrm{Z}/\gamma \to \tau^+\tau^-$ are shown in red. The jets background is estimated from data following the method mentioned in section 4.5.3. The cosmic background is supposed to be reduced to a negligible rate by the anti-cosmic dimuon cut so that they are not shown.

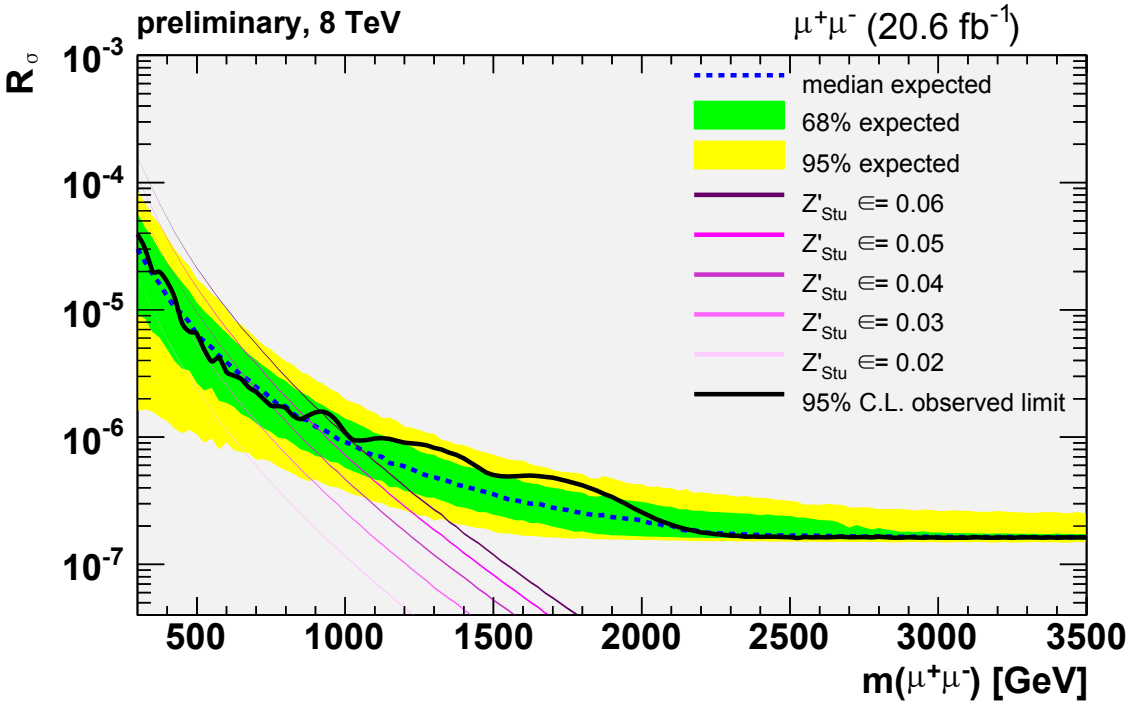

Figure B.2: The 95% C.L. R_σ upper limits ($R_\sigma^{(0.95)}$) as a function of the dimuon resonance mass m_{res} with CMS 2012 data at $\sqrt{s} = 8\,\text{TeV}$.

From Figure B.2, the observed 95% C.L. mass lower limits of the Z'_{St}s are obtained and are shown in Table B.1. The table also compares the dimuon analysis results of the 2012 analysis with those of the 2011 analysis. The results of the dielectron analysis are not included in this table.

	expected (GeV)		observed (GeV)	
	in 2011	in 2012	in 2011	in 2012
Z'_{St}, $\epsilon = 0.03$	N/A	410	N/A	360
Z'_{St}, $\epsilon = 0.04$	410	670	520	750
Z'_{St}, $\epsilon = 0.05$	560	900	540	870
Z'_{St}, $\epsilon = 0.06$	690	1050	860	920

Table B.1: 95% C.L lower mass limits for the Z'_{St}s with different ϵ_{s}. Because the detector dimuon invariant mass resolution in this range is from 10 to 40 GeV and the dielectron invariant mass resolution is about 10 GeV, the numbers are rounded to 10 GeV.

B.3 The (C_d, C_u) and $(M_{Z'_{St}}, \epsilon)$ limit of the Stueckelberg Z′

The observed limits obtained in B.2 are translated to the excluded and allowed region of up and down type quark coupling constants. It is done by the same method with the 2011 analysis using Equation 4.16. Thus an update of Figure 4.13 based on CMS 2012 dimuon data is shown in Figure B.3.

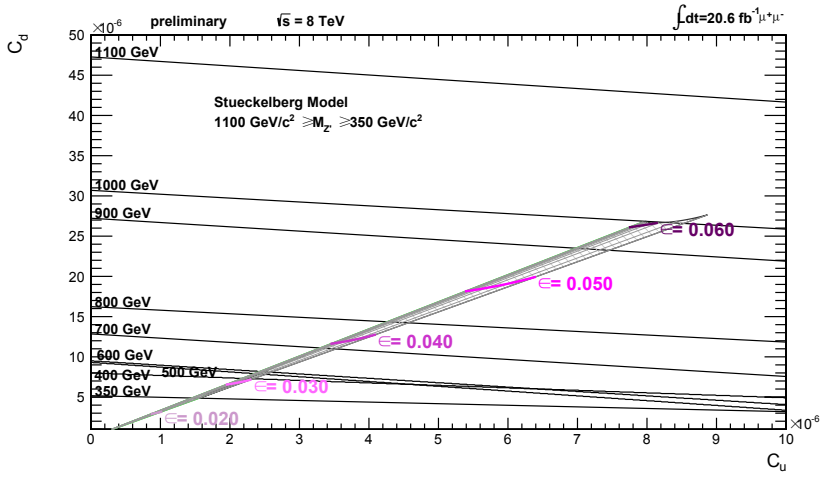

Figure B.3: The 95% C.L. upper limits on the Z′cross sections for given masses are equivalent to excluded regions in the (C_d, C_u) plane which are bounded by the thin black lines in the figure. For each $M_{Z'_{St}}$, the region above the corresponding black line is excluded at 95% C.L..

As what is done in the 2011 analysis, the coordinate of (C_d, C_u) is rotated by 0.295 rad counterclockwise. For each $M_{Z'_{St}}$, the excluded part of ϵ has been examined individually. Thus an update of Figure 4.14 based on CMS 2012 dimuon data is obtained in Figure B.4.

Combining the plots in Figure 4.14, Figure B.5 summarizes the allowed and 95% C.L. excluded region in the (C_d, C_u) and $(M_{Z'_{St}}, \epsilon)$ parameter spaces, as an update of Figure 4.15.

As a result, in 2012, the CMS see about four times amount of data than in 2011. The expected and observed 95% C.L. lower dimuon invariant mass limits are both increased by hundreds of GeV. For the model parameter values $\epsilon = 0.06(0.05, 0.04, 0.03)$, Stueckelberg Z′s with masses smaller than $920(870, 750, 360)$ GeV are excluded at 95% confidence level. The up and down quark couplings (C_u and C_d) are further excluded at 95% C.L. as well.

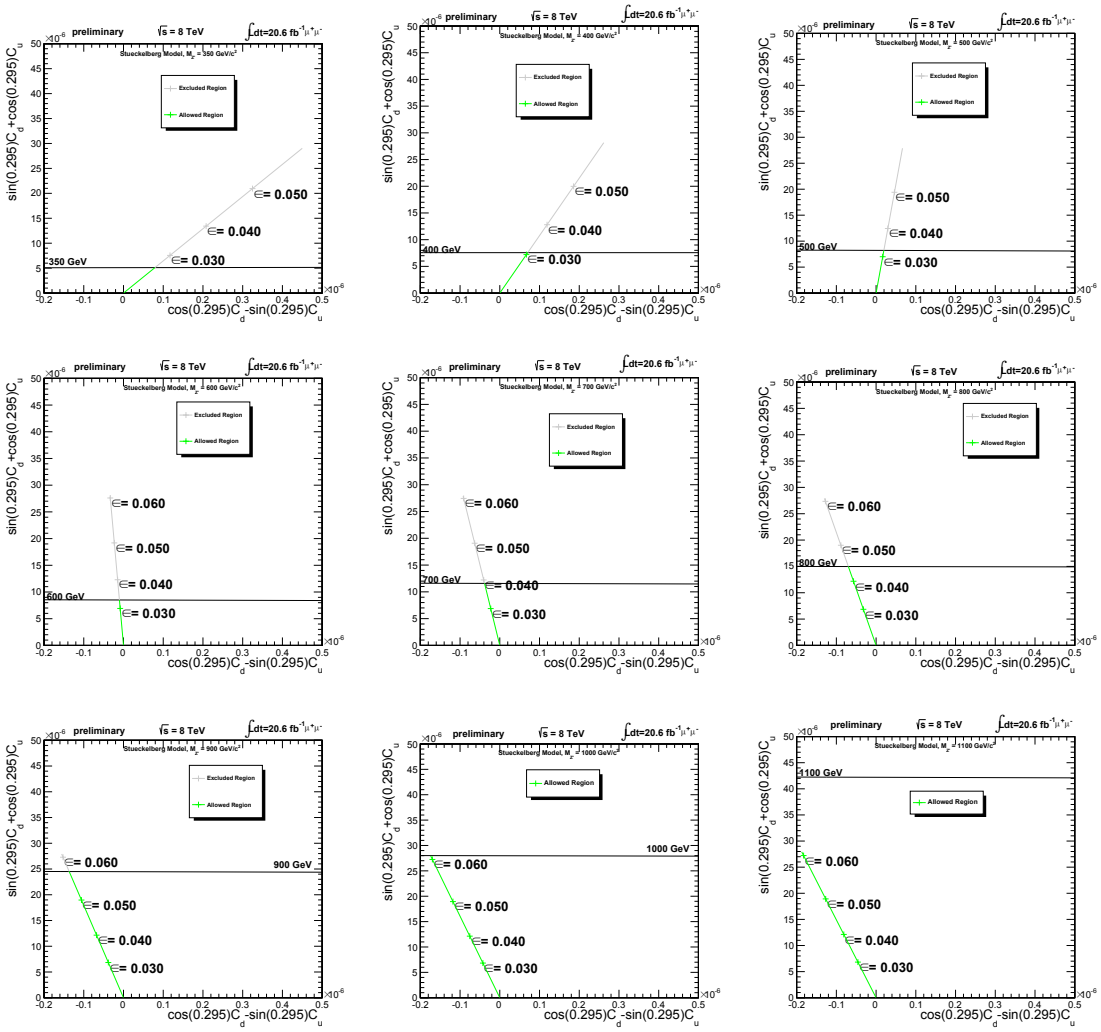

Figure B.4: The 95% C.L. upper limit of ϵ for each given $M_{Z'_{St}}$, where $M_{Z'_{St}} = 350, 400, 500, 600, 700, 800, 900, 1000, 1100\,\text{GeV}$ horiontally from top-left to bottom-right.

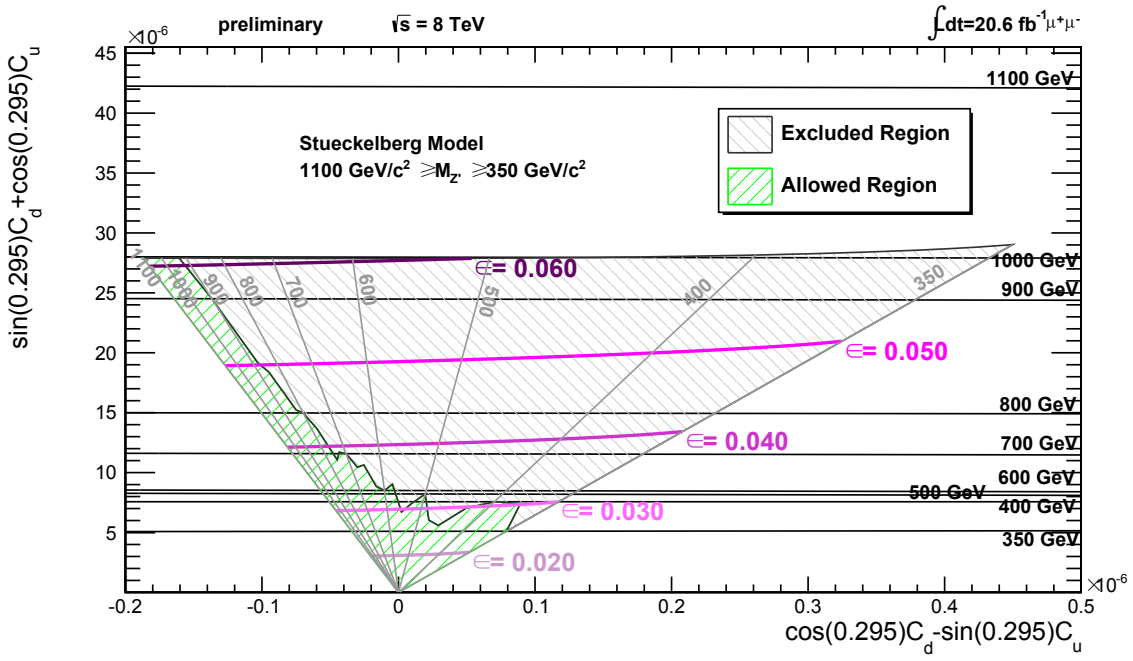

Figure B.5: The 95% C.L. excluded regions on the rotated (C_d, C_u) plane. The black lines are the border lines of the 95% C.L. excluded regions. The gray lines are the iso-$M_{Z'_{St}}$-lines. The magenta lines are the iso-ϵ-lines.